NASA Contractor Report 3302

Analytical Investigation of Fan Tone Noise Due to Ingested Atmospheric Turbulence

Ulrich W. Ganz

CONTRACT NAS1-15085
AUGUST 1980

NASA

NASA Contractor Report 3302

Analytical Investigation of Fan Tone Noise Due to Ingested Atmospheric Turbulence

Ulrich W. Ganz
Boeing Commercial Airplane Company
Seattle, Washington

Prepared for
Langley Research Center
under Contract NAS1-15085

National Aeronautics
and Space Administration

**Scientific and Technical
Information Branch**

1980

CONTENTS

FIGURES

1.0 SUMMARY

It is well known that there exists systematic differences in the fan stage noise between static (ground test) and flight conditions. These differences are significant in the current high bypass ratio engines with single stage, non-IGV fans. They have been designed to provide complete cutoff at the blade passing frequency (BPF) throughout the approach power range. However, results from static tests with these engines reveal a strong presence of the BPF tone. This tone has been associated with the steady and unsteady distortions in the static fan inflow field in particular the atmospheric turbulence, the ground vortex, test stand induced distortions and the interference of all these disturbances with the inlet boundary layer. Fan noise data from flight tests with these engines show significantly lower BPF levels, but usually indicate that complete elimination has not been achieved. The remaining fan tone has been associated with the atmospheric turbulence, inlet angle of attack related distortions as well as incomplete cutoff of rotor stator interaction noise. The primary purpose of the present investigation is

- to define an atmospheric turbulence model
- to identify the turbulence length scales that dominate in the generation of fan tone noise due to convected turbulence, and
- to evaluate the difference in fan tone noise due to atmospheric turbulence between static and flight conditions.

The investigation is based on analytical and empirical models and is divided into two segments. The first segment is concerned with the definition of the turbulence at the fan face, which is related to the atmospheric turbulence in the ambient flow field and is affected by the flow contraction between the ambient and the fan face conditions. The second segment is concerned with the fan noise generation due to convected turbulence.

Based on a literature search an atmospheric turbulence model has been selected that predicts turbulence intensities, integral scales and spectra as a function of the altitude above the ground, the mean wind velocity, the surface roughness and atmospheric stability. An existing flow contraction model has been extended to provide all the one-dimensional spectra of the post-contraction turbulence for simple, isotropic pre-contraction turbulence. Narrow-band fan noise resulting from ingested anisotropic but homogeneous turbulence has been studied with existing fan noise models with particular emphasis on fan noise resulting from atmospheric turbulence in static and flight conditions. The primary results of the study are:

- The difference in fan tone power at BPF due to ingested atmospheric turbulence between typical static test conditions and typical landing approach flight conditions is in the order of 30 dB. Based on this difference it is concluded that fan noise due to ingested atmospheric turbulence is negligible in landing approach conditions for the currently used high bypass ratio engines.

- Based on the analytical results it is concluded that fan noise due to atmospheric turbulence is below actual fan noise in flight conditions. It is therefore assumed that it is not necessary to simulate in-flight turbulence in static tests. However, fan noise due to atmospheric turbulence in static tests should be reduced to levels below broadband fan noise in flight conditions. An effective way to achieve this, is the reduction of the turbulence intensities in the static inflow field. The following guidelines are recommended for static test conditions:

  - usage of an inflow control device
  - low limits on wind velocities
  - small surface roughness scale in the test stand environment
  - large height of engine axis above ground
  - mean wind direction from the forward arc to eliminate reingestion

  Proper test stand and bellmouth inlet design and possibly inlet boundary layer suction are necessary to achieve this reduction.

- Rotor tone noise due to convected turbulence is dominated by a small range of transverse scales. For typical turbulence energy distributions this range covers about one decade and is centered around a transverse scale in the order of 30% of the rotor blade spacing at the blade tip. For a given turbulence variance, maximum sound power is achieved at transverse integral scales in the order of 25% of the rotor blade spacing at the blade tip. For a JT9D fan this is about 4.1 cm and for the JT15D fan it is about 1.3 cm.

- The difference in fan tone noise due to atmospheric turbulence between static and flight conditions is primarily due to the difference in the intensities of the turbulence involved in the fan tone noise generation. In static conditions the atmospheric turbulence is affected by a large inflow contraction, which results in:

  - large initial scale and therefore high initial turbulence energy level
  - large increase in the standard deviation of the transverse turbulence component
  - large streamwise integral scale at the fan face

  In the flight conditions the turbulent energy at large wavenumbers decreases with altitude, due to the nearly constant turbulence variance and the increase of the integral scales with altitude.

  The effect of inlet angle of attack on fan noise has been evaluated with data acquired during a flight test with a 747 aircraft powered with JT9D engines. Sound pressure measurements were made on the inlet wall, the fan duct wall and the fuselage surface over the full operational range of aircraft angle of attack. The measurements indicate that there is no obvious correlation between inlet angle of attack changes and changes in broadband noise as well as narrowband noise at BPF and its second and third harmonic. A circumferential variation of the buzzsaw sound pressure field in the inlet that increases with angle of attack, has been observed.

2.0 INTRODUCTION

By now it is well known that systematic differences exist between the fan stage noise in static and flight conditions (Ref 1 to 6). These differences became apparent with the introduction of the current high bypass, single stage, non-IGV fans. These engines are designed to provide complete cutoff at the fan blade passing frequency throughout the approach power range. However, results from static tests with these engines revealed a strong presence of the blade passing frequency (BPF) tone. Most of the corresponding flight test data show significantly lower BPF levels, but indicate that complete cutoff has not been achieved. The appearance of the BPF tone in static tests has been related to rotor noise due to steady and unsteady distortions in the fan inflow field, such as atmospheric turbulence, the ground vortex, test stand induced distortions and the interference of all these distortions with the inlet boundary layer (Ref 5 to 8). Much progress has been made in the simulation of flight inflow conditions with inflow control devices (Ref 4, 9 and 10). Further improvements have been achieved with the combined application of inflow control and inlet boundary layer suction (Ref 11). Another approach that has been used successfully to simulate in-flight conditions is the evaluation of scaled fan models in wind tunnels (Refs 10, 12 and 13).

The cause of the remaining fan tone in flight is not known. It has been associated with atmospheric turbulence, inlet angle of attack induced distortions as well as incomplete cutoff of rotor-stator (primary or secondary) interaction noise. Little work has been done in the evaluation of fan noise due to atmospheric turbulence in flight conditions. A Boeing in-house report used simple turbulence and fan noise models and showed significant differences between the two conditions. Substantial differences in the unsteady pressure distributions on propellor blades between static and flight conditions, which have been related to convected atmospheric turbulence, are reported in Reference 15.

It is the primary purpose of the present study to evaluate the difference in fan noise due to atmospheric turbulence between static and flight approach conditions. The investigation is divided into two segments. The first segment is concerned with the definition of the turbulence at the fan face, which is related to the atmospheric turbulence in the ambient flow field and is affected by the flow contraction between the ambient and the fan face condition. An existing model that describes the properties of the atmospheric turbulence (Ref 16) is used to define the turbulence in the inflow streamtube ingested by the fan. The effects of the inflow contraction between the ambient and the fan face conditions on the atmospheric turbulence are estimated based on an existing model (Ref 17), which has been extended to provide more detailed information. In order to compute fan noise resulting from convected turbulence with the selected fan noise models, it was necessary to represent the turbulence at the fan face by a distribution of discrete distortion elements. A model that computes the statistical averages (spectra, correlations, length scales and variances) of such distributions of distortion elements has been developed and is described.

The second segment of the study is concerned with the fan noise generation due to convected turbulence. The range of transverse scales involved in fan noise generation is determined and a limited parametric study of fan noise due to convected turbulence is conducted. All the models mentioned previously are then combined to estimate the difference in fan narrowband noise due to atmospheric turbulence between static and flight conditions. Results based on measured and predicted turbulence at the fan face are compared.

An additional segment of the study is concerned with the inlet angle of attack effects on fan noise. Results from a flight test conducted jointly by P&WA and Boeing with a 747 aircraft powered by JT9D engines are presented.

Use of trade names or names of manufacturers in this report does not constitute an official endorsement of such products or manufacturers, either expressed or implied, by the National Aeronautics and Space Administration.

The author would like to acknowledge the technical support received throughout this project from T. L. Clark.

3.0 SYMBOLS AND ABBREVIATIONS

a	Transverse scale of distortion elements
A_{mnk}	Mode amplitude of spinning order m, radial order n and harmonic order k
B	Half bandwidth used in the evaluation of narrowband tones
c	Velocity scale of largest distortion elements
c_o	Speed of sound
c_l	Velocity scale of distortion elements
c_h	Rotor blade chord
c_L	Rotor blade section lift coefficient
c_p	Specific heat of air at constant pressure
C_i	Correlation coefficient of the i^{th} turbulence velocity component
d	Boundary layer thickness Coefficient, 1. for Gaussian eddy field, e/2 for vortex field
E	Eddy or vortex volume
F_i	One dimensional spectrum of the i^{th} turbulence velocity component
g	Gravitational acceleration
G(k)	Spectrum function
$G_{mn\ell^*}$	Airfoil acoustic response function
I_{ℓ^*}	Modified Bessel function of the first kind and order ℓ^*
I_z	Axial acoustic energy flux
k	Von Karman constant (.4)
	Wavenumber vector in turbulence velocity field
	Harmonic order in fan narrowband sound pressure field
K_{mn}	Axial wavenumber component of fan narrowband sound pressure field
ℓ	Mixing length
	Streamwise scale of distortion elements
	Contraction ratio

ℓ'	Monin-Obukov length scale
ℓ^*	Circumferential distortion order
L_{ij}	Integral length scale of i^{th} turbulence component along j^{th} coordinate axis
m	Exponent in β probability density distribution
	Spinning order
M	Axial mean flow Mach number
M_m	Mean flow Mach number relative to fan rotor blade
M_t	Mechanical fan tip Mach number
n	Exponent in β probability density distribution
	Radial order
N	Constant in spectrum function
	Density of distortion elements
	Number of rotor blades
p	Static pressure
	Acoustic pressure
P	Probability density distribution
Q	Velocity amplitude of turbulence wave
	Occurrence rate
	BL/M
r	Radial coordinate within distortion elements
R	Radial location of distortion element center
R_o	Radius of outer annulus wall
R_A	Radius of inflow streamtube
R_i	Correlation function of i^{th} turbulence component
$\mathcal{R}$	Normalized duct eigen-function
s	Normalized random variable
t	Normalized random variable
	Time

T	Static temperature
u	Turbulence velocity component
	Streamwise turbulence velocity component
$u_\star$	Friction velocity
U	Mean flow velocity
v	Transverse turbulence velocity component
w	Vertical turbulence velocity component
W	Acoustic sound power
x	Cartesian coordinate
z	Vertical coordinate
	Axial duct coordinate
z_o	Surface roughness scale
z_I	Height where turbulence variances become equal
α	Rotor blade angle of attack
α, β	Exponents in length-velocity scale relationship
γ	Constant in spectrum function
γ	Stagger angle
Γ	Gamma function
Γ_{ij}	Three dimensional turbulence spectrum
δ	Delta function
ϵ	Contraction parameter $\left(\ell_2 / \ell_1\right)^2$
η	Hub to tip ratio
$\mathcal{H}$	Post-contraction wavenumber vector
λ	Turbulence wavelength
μ_{mn}	Annular duct eigenvalue
ξ	Separation vector
ρ	Radial duct coordinate

ρ_o	Standard density of air
σ	Turbulence velocity standard deviation
σ	Density ratio
τ	Time delay
ϕ	Angular duct coordinate
Φ	Angular eddy center coordinate
ϕ_i	Universal functions in atmospheric turbulence model
ω	Angular frequency
ω_o	Blade passing frequency
Ω	Vorticity vector

subscripts

o	Ground surface condition
	Standard condition
1,2,3	Indices for vector or matrix components
a	Associated with transverse distortion scale
i,j,k	Indices for vector or matrix components
ℓ	Associated with streamwise distortion scale
u,v,w	Associated with turbulence velocity components
A	Pre-contraction condition
AP	Airplane
B	Post-contraction condition
E	Gaussian eddy
F	Approach flight condition
P	Pulse related parameter
REF	Reference condition
S	Static test condition
SL	Single streamline

SS	Single scale
V	Vortex

superscripts

A	Pre-contraction condition
B	Post-contraction condition
$\rightarrow$	Vector

abbreviations

erf	Error function
BMT	Blade mounted transducers
BPF	Blade passing frequency
PDD	Probability density distribution
Ri	Richardson number
$\sim$	Proportionality
$\cong$	Approximate equality

4.0 TURBULENCE MODELS

A major goal of this study is to provide a comparison of fan tone noise resulting from ingested atmospheric turbulence between typical static and flight test conditions (Sec. 5.3). This requires the definition of turbulence models that allow the description of the atmospheric turbulence at the fan face. A model that defines the statistical averages for atmospheric turbulence in typical test conditions is described in Section 4.1. The description of a model that estimates the effects of the flow contraction between the ambient and fan face conditions on the atmospheric turbulence is included in Section 4.2. In the evaluation of fan tone noise due to turbulence, the latter is represented by a homogeneous distribution of distortion elements. A model that allows such a representation of the atmospheric turbulence at the fan face is described in Section 4.3.

4.1 ATMOSPHERIC TURBULENCE MODEL

4.1.1 BACKGROUND

The planetary or atmospheric boundary layer extends between the Earth's surface and the outer atmosphere. It absorbs the shear between the surface, with its no-slip condition and the geostrophic wind at the upper edge. It is characterized by large scales; its thickness is in the order of 600 meters. It normally is divided into 2 layers, the outer layer and the surface layer. In the latter, the flow is assumed 2 dimensional, unaffected by the coriolis force. The random motion within this boundary layer, atmospheric turbulence, is also characterized by its large scale. The separation between variations in the mean wind velocity and turbulence fluctuations is best described by the Van der Hoven spectrum, Figure 1.

Atmospheric turbulence for two conditions, static and flight approach power noise tests, is considered in the present study. In static tests, the atmospheric turbulence in the test stand environment, 0 to 20 meters above the ground is of concern. In flight tests, the turbulence at the approach path altitude (120 meters) above the noise certification location must be considered. Both of these conditions occur within the atmospheric boundary layer.

Only a limited amount of data describing atmospheric turbulence at the fan face of statically operated engines is available, References 19 and 20. No measurements have been made in the corresponding turbulence field in flight conditions. Such measurements would be very difficult to make, due to the extreme noise environment in the engine inlet and the low turbulence intensities associated with the small scales that are of interest. This lack of experimental data makes it necessary to base this study on empirical and analytical models. Several models are available that provide the statistical averages describing atmospheric turbulence, References 21 through 23, and extensive bibliographies are presented in References 23 and 24. The model selected for the present study is summarized in the following paragraph. To a large extent, it is based on information developed in Reference 25, and it is described in great detail in Reference 16.

4.1.2 MODEL DESCRIPTION

Both test conditions in this study are limited to low wind velocities. The limits are imposed to assure high quality for the acoustic data and satisfactory engine operation in static tests. For the flight condition FAR Part 36 prescribes a 5.14 m/s (10 kn) upper limit on the mean wind velocity at 10 m above the ground. The limits for static test conditions are not regulated, but similar wind limits are used throughout the industry. They are normally specified at the altitude of the engine axis above the ground as a function of the angle between the wind direction and the engine axis. The limits are typically 2.68 m/s (6 MPH) in the forward arc and fall off to zero for crosswinds and winds from the aft arc.

Turbulence in the atmospheric boundary layer is generated by two mechanisms, buoyant convection and shear stresses. The shear stress related turbulence production is proportional to the mean velocity gradient and therefore decreases with altitude, whereas the buoyant production is assumed invariant with altitude. For this reason the turbulence production due to shear stresses dominates in high winds and at low altitude. But in low wind velocities and at high altitude, the buoyant production can become significant. For this reason one of the requirements for the atmospheric turbulence model was the inclusion of the buoyant production terms, to properly simulate low wind velocity conditions. Another requirement was the proper description of turbulence at large wavenumbers, where the turbulence becomes isotropic. This is important in the evaluation of in-flight turbulence, where only a limited, high wavenumber segment of the total turbulence spectrum is of interest. Based on these requirements the atmospheric turbulence model described in Reference 16 has been selected for this study.

In the lower layer of the atmospheric boundary layer (the surface layer), the mean flow field is assumed to be two dimensional. This layer covers the lowest 10 to 20% of the atmospheric boundary layer. It includes the static test environment and its upper boundary is close to the flight condition. It is also called the constant stress layer, due to the fact that the shear stress τ remains approximately constant throughout it.

$$\tau = \rho\, u_{\bigstar}^{2} \tag{4.1.01}$$

with

ρ = air density
$u_{\bigstar}$ = friction velocity

Outside of the viscous sublayer the shear stress is dominated by the Reynolds stress

$$\tau \cong \rho\overline{uw} \cong \rho\, \ell^2 \left(\frac{\partial U}{\partial z}\right)^2 \tag{4.1.02}$$

with

u, w = turbulence velocity components
ℓ = mixing length
U = mean flow velocity

The coordinate system is shown in Figure 2.

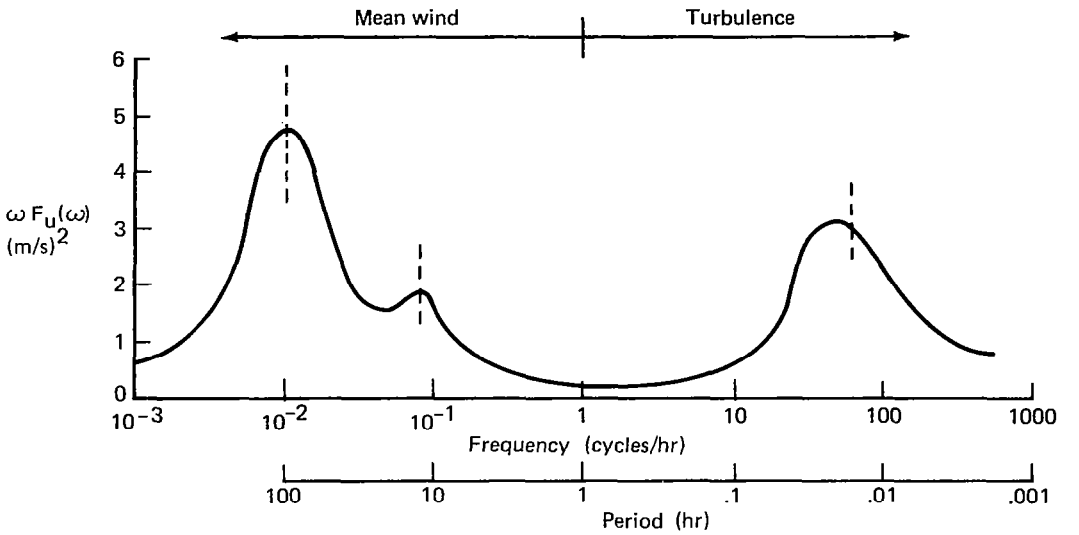

Figure 1.—Schematic Spectrum of Wind Speed Near the Ground From a Study of Van Der Hoven (1957) (From Ref 18)

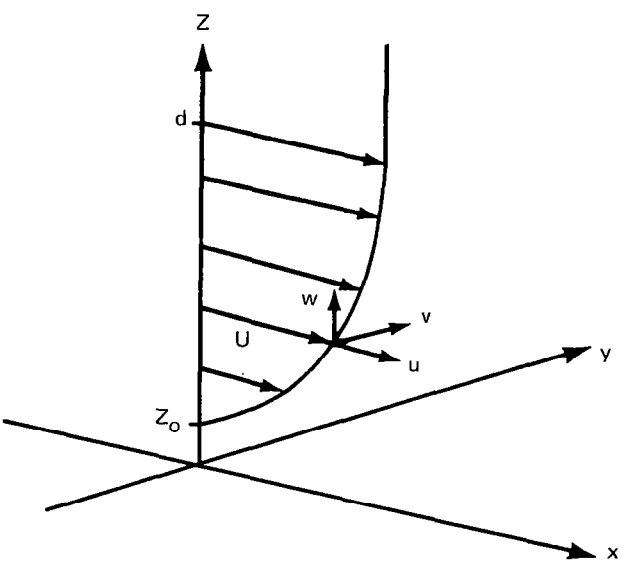

Figure 2.—Coordinate System for Atmospheric Boundary Layer Model

If it is further assumed that the mixing length ℓ is proportional to the coordinate z, then the above equations lead to the well-known logarithmic velocity profile

$$\ell = k \cdot z$$

$$\frac{\partial U}{\partial z} = \frac{u_\star}{kz} \tag{4.1.03}$$

$$U(z) = \frac{u_\star}{k} \int_{z_o}^{z + z_o} \frac{\partial z}{z} = \frac{u_\star}{k} \ell n \left(\frac{z + z_o}{z_o} \right) \tag{4.1.04}$$

with

k = von Karman constant = .4
z_o = roughness scale

The friction velocity $u_\star$ is the velocity scale in the surface layer and the standard deviations of the turbulence components are proportional to it. Equation (4.1.04) is used to determine $u_\star$ based on the wind velocity at a reference altitude z_{REF} and the roughness scale z_o.

$$u_\star = U\left(z_{REF}\right) \cdot k \frac{1}{\ell n \left(\frac{z_{REF} + z_o}{z_o} \right)} \tag{4.1.05}$$

The friction velocity and therefore also the turbulence standard deviations are proportional to the reference wind velocity and increase with increasing surface roughness scale. The latter is a measure of the surface roughness and is in the order of 10% of the size of the roughness elements. Representative roughness scales are shown in Figure 3. In Reference 16, a roughness scale of .05 meters has been suggested for the airport environment.

Equation (4.1.04) is based on the assumption of constant shear stress. It loses its validity when z approaches the size of the roughness elements and is therefore limited to conditions where $z >> z_o$.

Thermal Stability

So far only turbulence produced by shear stress has been considered. In a neutral atmosphere the pressure p and temperature T follow the isentropic relationship and buoyant production is zero.

$$\frac{\partial p}{\partial z} = -\rho g$$

$$\frac{\partial T}{\partial z} = \frac{1}{c_p \cdot \rho} \cdot \frac{\partial p}{\partial z} = \frac{-g}{c_p} \tag{4.1.06}$$

with

g = gravitational acceleration
c_p = specific heat at constant pressure

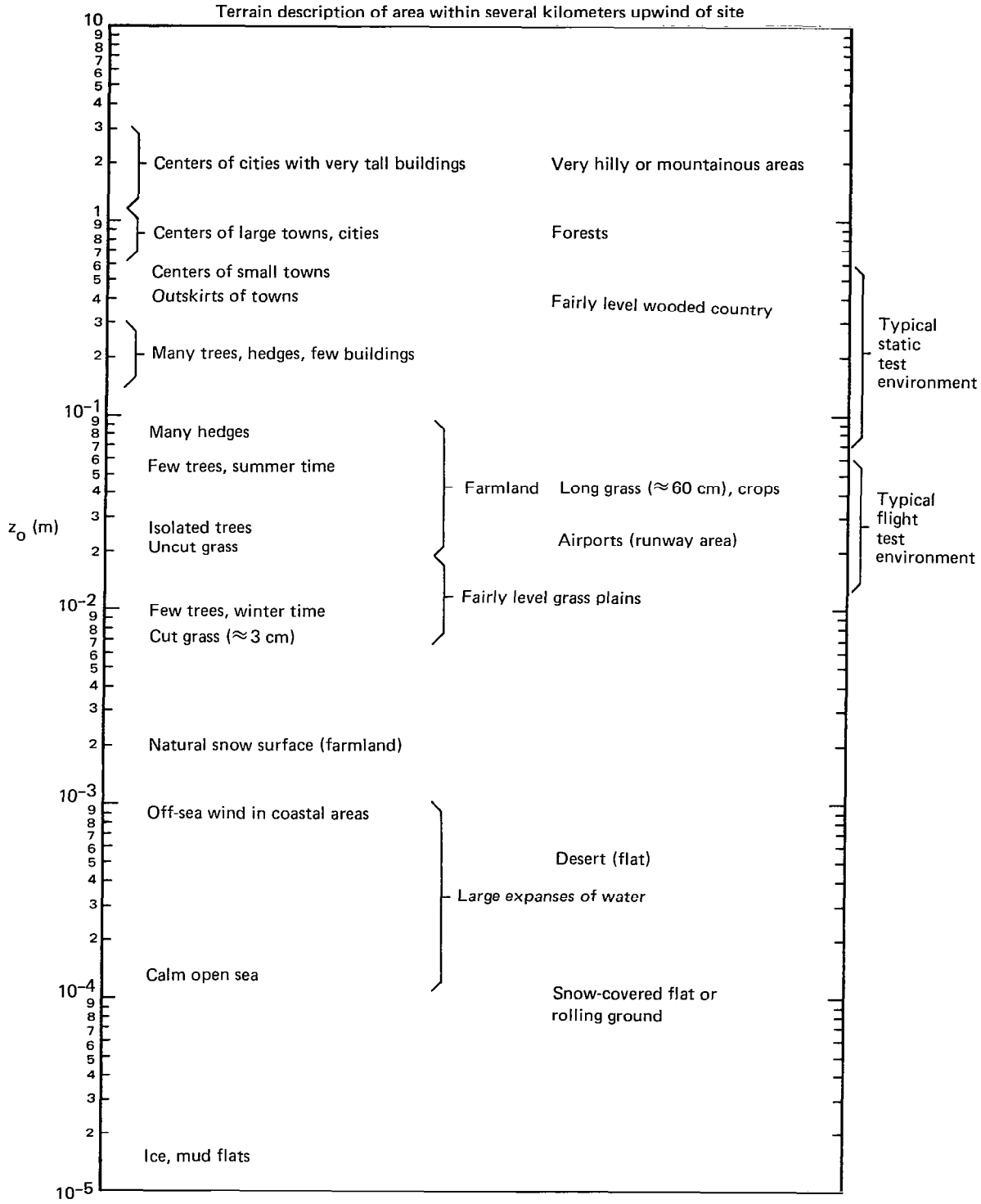

Figure 3.—Values for Surface Roughness Scale Z_0 (From Ref 22)

If however, the temperature gradient deviates from the isentropic relationship, buoyant production can either increase or decrease the stress produced turbulence. The atmospheric stability and its effect on the atmospheric turbulence are described by stability parameters. The best known parameters are the Richardson number (Ri) and the Monin-Obukov length scale (ℓ'). (Ri) and (z/ℓ') represent the production ratio between buoyant and stress generated turbulence. The parameter used in the selected model, the length scale ℓ' is described in Reference 25.

$$\ell' = \frac{u_\star \left(\frac{\partial U}{\partial z}\right) T}{k\, g \left(\frac{\partial T}{\partial z} + \frac{g}{c_p}\right)} \qquad (4.1.07)$$

The sum in the denominator represents the difference between the actual and the isentropic temperature lapse rates. ℓ' can be determined with simple mean velocity and temperature measurements. The following conditions can be defined based on the actual temperature lapse rate.

unstable atmosphere $\quad \frac{\partial T}{\partial z} < -\frac{g}{c_p} \qquad \frac{z}{\ell'} < .0$

neutral atmosphere $\quad \frac{\partial T}{\partial z} = -\frac{g}{c_p} \qquad \frac{z}{\ell'} = .0$

stable atmosphere $\quad \frac{\partial T}{\partial z} > -\frac{g}{c_p} \qquad \left(\frac{z}{\ell'}\right) > .0$

Mean Wind Velocity Profile

Turbulence generated by buoyant convection affects the mean velocity profile. For non-neutral conditions equation (4.1.03) that defines the wind velocity gradient becomes

$$\frac{\partial U}{\partial z} = \frac{u_\star}{kz}\, \phi_1 \left(\frac{z}{\ell'}\right) \qquad (4.1.08)$$

with ϕ_1 (z/ℓ') a universal function.

So far the shear stress has been assumed constant, independent of altitude. But, in reality, it decreases with altitude and disappears at the edge of the boundary layer. In the selected model the shear stress is represented by the following relationship

$$\tau = \rho\, u_\star^2 = \tau_o \left(1 - \frac{z}{d}\right)^2 = \rho \left[u_{\star_o} \left(1 - \frac{z}{d}\right)\right]^2 \tag{4.1.09}$$

with

τ_o = shear stress at surface

$u_{\star_o}$ = friction velocity at surface

d = boundary layer thickness

Equation (4.1.08) then becomes

$$\frac{\partial U}{\partial z} = \frac{u_{\star_o}}{k\, z} \left(1 - \frac{z}{d}\right) \phi_1 \left(\frac{z}{\ell'}\right) \tag{4.1.10}$$

$$U = \frac{u_{\star_o}}{k} \left[\ell n \left(\frac{z + z_o}{z_o}\right) + \phi_2 \left(\frac{z}{\ell'}\right) - \frac{z}{d} \phi_3 \left(\frac{z}{\ell'}\right)\right] \tag{4.1.11}$$

With ϕ_2 and ϕ_3 universal functions of (z/ℓ') which are shown in Figures 4 and 5.

The surface friction velocity is determined from the mean wind velocity at the reference altitude z_{REF}, the length scale ℓ' and the surface roughness scale z_o.

$$u_{\star_o} = \frac{k \cdot U\left(z_{REF}\right)}{\ell n \left(\frac{z_{REF} + z_o}{z_o}\right) + \phi_2 \left(\frac{z_{REF}}{\ell'}\right) - \frac{z_{REF}}{d}\, \phi_3 \left(\frac{z_{REF}}{\ell'}\right)} \tag{4.1.12}$$

Turbulence Standard Deviation

The most consistent information concerning standard deviations of atmospheric turbulence is available for the vertical component. This is partially due to the lack of large scale motion close to the ground for this component. According to similarity analysis, the standard deviations of atmospheric turbulence are proportional to the friction velocity $u_\star$ and a function of the stability parameter (z/ℓ').

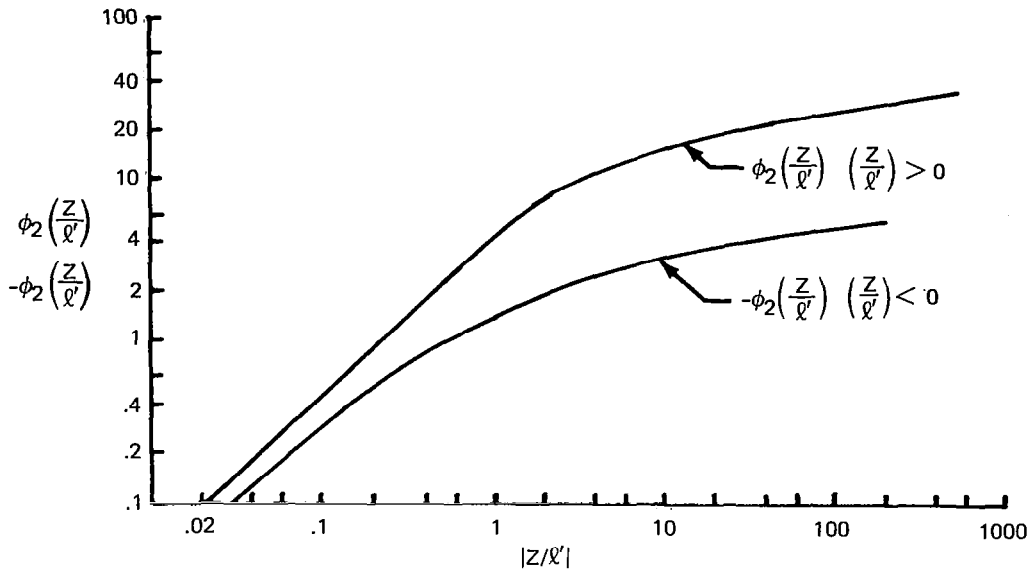

Figure 4.—Non-Neutral Stability Correction to Mean Wind Profile, $\phi_2\,(Z/\ell')$ (From Ref 16)

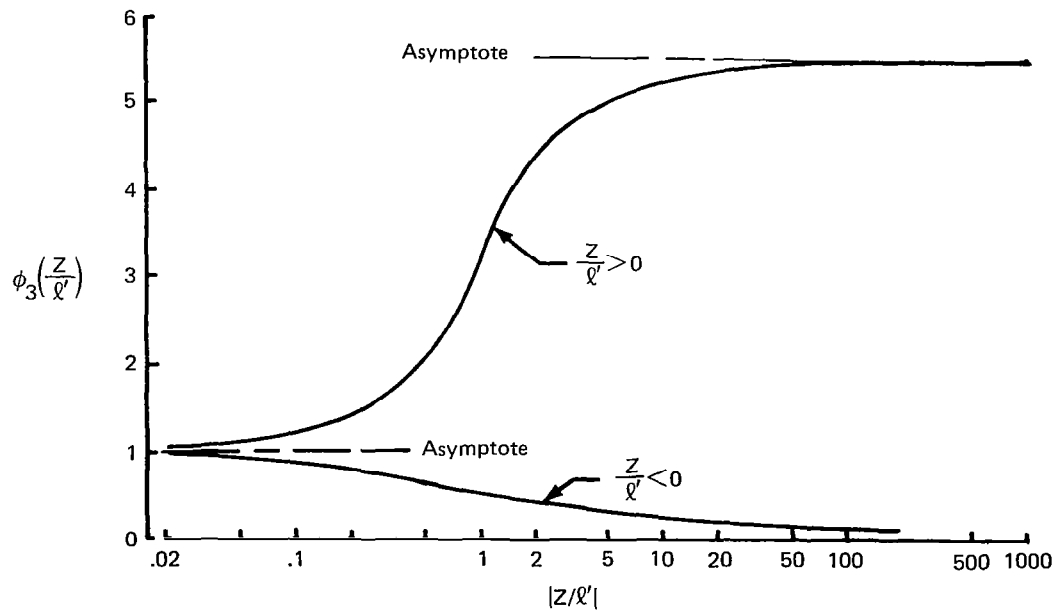

Figure 5.—Variable Shear Stress Correction to Mean Wind Profile, $\phi_3\,(Z/\ell')$ (From Ref 16)

$$\sigma_w = u_{\star_o} \left(1 - \frac{z}{d}\right) \phi_4 \left(\frac{z}{\ell'}\right) \qquad (4.1.13)$$

The universal function ϕ_4 is shown in Figure 6. It assumes a value of 1.3 for neutral conditions and increases with decreasing stability. For highly unstable conditions, it approaches a relationship characteristic for a free convection layer. For stable conditions, it decreases slowly, and above the critical value of 1., it drops to zero indicating that turbulence cannot exist above this stability level.

According to equations (4.1.12) and (4.1.13) the standard deviation of the vertical turbulence component is proportional to the reference velocity and increases with the surface roughness scale and decreasing stability. For neutral stability it is insensitive to altitude.

Close to the ground, the standard deviations of the horizontal turbulence components deviate significantly from the one of the vertical component. This is mainly due to the fact that large scale motion for those components is not suppressed as much close to the ground. In the selected model, it has been assumed that the standard deviations for the two horizontal turbulence components are the same. They are proportional to σ_w and the proportionality factor is a function of the ratio between z and the altitude z_I, where the standard deviations of all 3 components become equivalent.

$$\sigma_u = \sigma_v = \sigma_w \frac{1}{\left(.177 + .823 \frac{z}{z_I}\right)^{.4}} \quad z < z_I \qquad (4.1.14)$$

$$\sigma_u = \sigma_v = \sigma_w \qquad z \geq z_I$$

This empirical relationship is shown in Figure 7. Close to the ground the standard deviations of the horizontal components are twice as large as the one of the vertical component.

Integral Length Scales

Most integral length scales are based on autocorrelations from single point measurements in the atmospheric boundary layer. Taylor's hypothesis is used to compute integral length scales from integral temporal scales and the mean flow velocity. These measurements provide only information about the integral scales in the streamwise direction. As in the case of the standard deviation of the turbulence velocities, the data for the integral scale of the vertical component L_w are the most consistent. Similarity analysis suggests that the integral length scales are proportional to altitude with a proportionality factor that is a function of the stability parameter (ℓ'/z). Measured data do however indicate that the correlation between atmospheric stability and integral scale is insignificant. Most empirical relationships are based on straight proportionality between length scales and height. The proportionality factors are in the order of .35 to .5, a value of .5 is used in the selected model

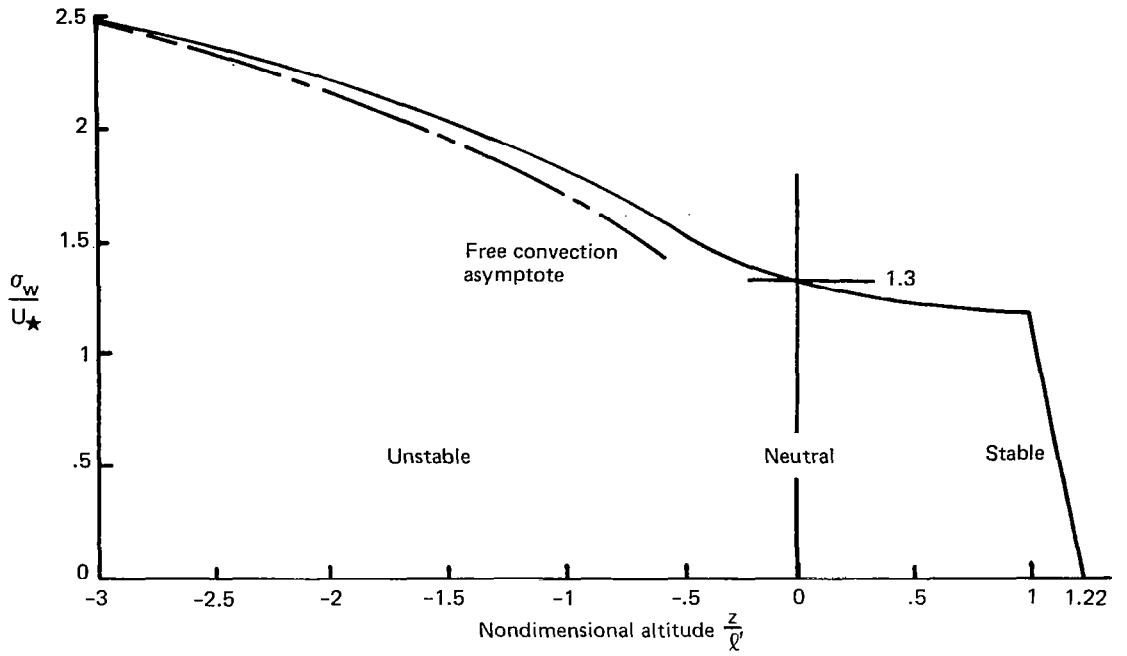

Figure 6.—Normalized Standard Deviation of the Vertical Turbulence Component (From Ref 16)

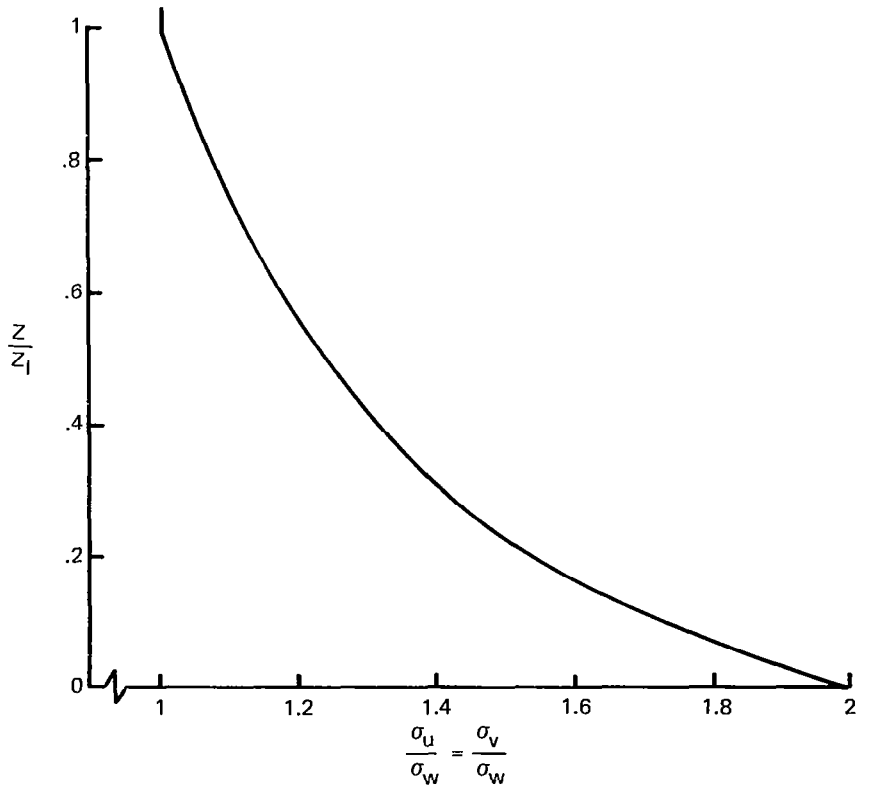

Figure 7.—Standard Deviations of the Horizontal Turbulence Components (From Ref 16)

$$L_w = .5\ z \tag{4.1.15}$$

Measured data for the other two length scales, L_u and L_v show significant scatter and it is difficult to represent them satisfactorily by simple empirical relationships. In the selected model, they are computed based on the standard deviations, the integral scale L_w and the assumption of isotropic turbulence at large wavenumbers. For von Karman spectra the above assumption leads to the following relationship for the streamwise integral length scales, Figure 8.

$$L_u = 2\ L_v = 2\ L_w \left(\frac{\sigma_u}{\sigma_w}\right)^2 \tag{4.1.16}$$

$$L_w = .5\ z \qquad \text{for } z < z_I$$

$$= .5\ z_I \qquad \text{for } z \geqslant z_I$$

Turbulence Spectra

Atmospheric turbulence is neither homogeneous nor isotropic. Its statistical averages are a function of the vertical coordinate and depend on the orientation of the coordinate system. It is however assumed that the turbulence is homogeneous in horizontal planes and stationary at a fixed location. This makes it possible to define local, statistical averages. Even though the atmospheric turbulence cannot be considered isotropic, its one dimensional spectra exhibit characteristics typical for isotropic turbulence. At high frequencies the spectra follow the inertial subrange relationship characterized by its (-5/3) exponent. In this frequency range, the ratio between the spectrum levels of the transverse and the streamwise turbulence components becomes 4/3 (Ref 26), and the cross spectrum between the streamwise and the vertical turbulence components tends to zero (Ref 27). Based on these observations, it has been suggested that atmospheric turbulence is isotropic for wavelengths smaller than z/3 (Ref 21). Even though turbulence is not isotropic for wavelengths above this limit, it still is well represented by spectra developed for isotropic turbulence as long as the integral scales and variances are permitted to be different for the 3 turbulence components. The von Karman spectra satisfy the requirements for isotropic turbulence at large wavenumbers and fit experimental data well, especially in the inertial subrange. They are used to represent the spectral distribution of the turbulent energy in the selected turbulence model.

$$F_u = \frac{2\ \sigma_u^2\ L_u}{\pi} \frac{1}{\left[1 + \left(1.339\ L_u\ k_1\right)^2\right]^{5/6}} \tag{4.1.17}$$

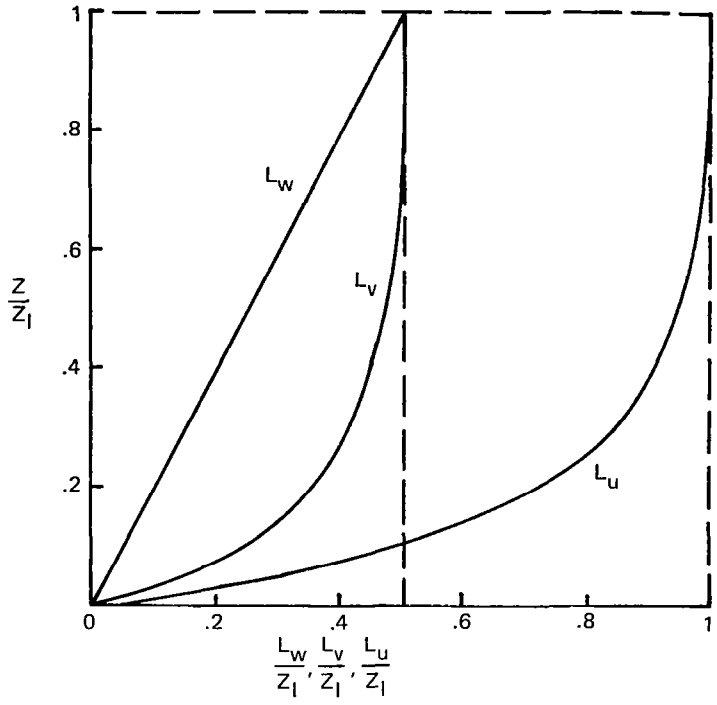

Figure 8.—Streamwise Integral Scales (From Ref 16)

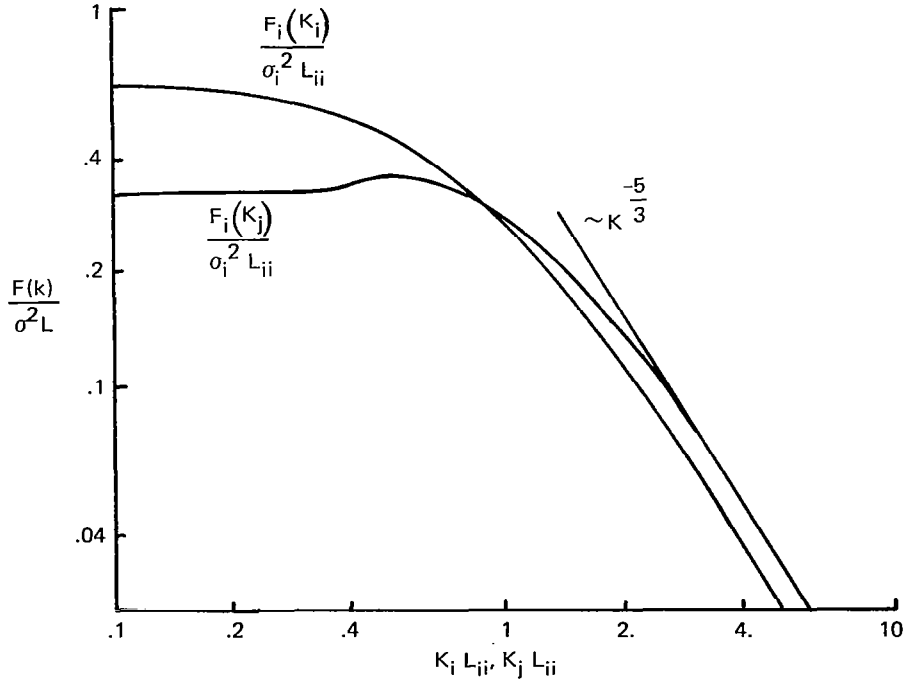

Figure 9.—Von Karman Spectra Normalized With the Integral Scale Parallel to the Turbulence Component

$$F_v = \frac{2\sigma_v^2 L_v}{\pi} \frac{\left[1 + \frac{8}{3}\left(2.678\, L_v k_1\right)^2\right]}{\left[1 + \left(2.678\, L_v k_1\right)^2\right]^{17/6}} \tag{4.1.18}$$

$$F_w = \frac{2\sigma_w^2 L_w}{\pi} \frac{\left[1 + \frac{8}{3}\left(2.678\, L_w k_1\right)^2\right]}{\left[1 + \left(2.678\, L_w k_1\right)^2\right]^{17/6}} \tag{4.1.19}$$

The corresponding normalized spectra are shown in Figure 9.

4.1.3 RESULTS

The atmospheric turbulence model is used in Section 5.3.3 in the comparison of rotor tone noise due to atmospheric turbulence between static and flight conditions. Some relevant results are presented in that section.

The following principal results can be inferred directly from the equations of the selected atmospheric turbulence model.

- The standard deviations of the turbulence velocity components are proportional to the friction velocity, which is proportional to the reference wind velocity and increases with the surface roughness scale.
- In the neutral atmosphere the standard deviation of the vertical component is nearly independent of altitude. In unstable conditions it increases, in stable conditions it decreases with altitude.
- The integral scales of all the turbulence components increase with altitude.
- Due to the fact that the standard deviation of the vertical turbulence component is nearly constant throughout the surface layer and because its integral length scale increases with altitude, its power spectrum level at large wave numbers decreases with increasing altitude, Figure 10.

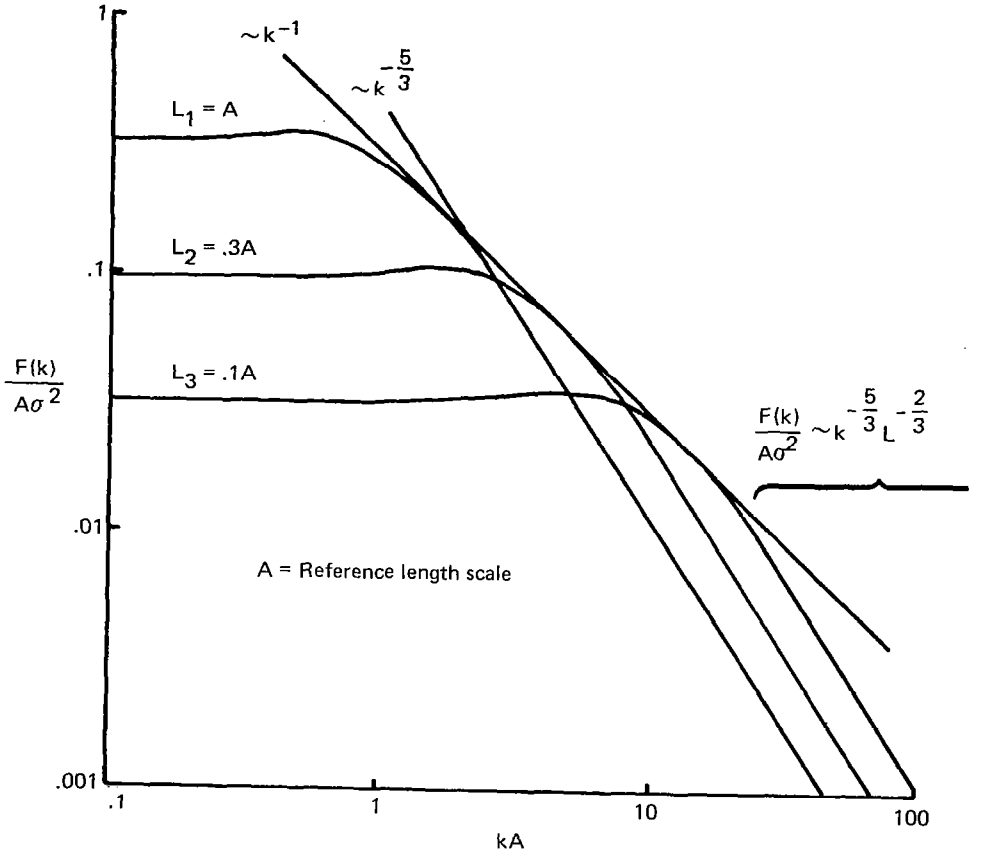

Figure 10.—Spectra Based on the Same Turbulence Variance σ^2 But Different Integral Scales L_i

4.2 INFLOW CONTRACTION MODEL

4.2.1 BACKGROUND

The most significant difference in the fan inflow field between static and flight conditions is the difference in the flow acceleration between the ambient and the fan face conditions. The fan face velocities are very similar for the two conditions, but the acceleration starts from the airplane forward velocity in flight, and from the local mean wind velocity in static tests. Similar flow contractions are present in wind tunnels between the settling chamber and the test section. It is primarily due to those, that aerodynamicists have been interested in the fluid mechanic characteristics of such contractions. It has been found that they have a significant effect on the freestream turbulence carried by the mean flow. This phenomenon has been studied with analytical models (Ref 28 to 30) as well as experimental investigations (Ref 31). Prandtl (Ref 28) studied the contraction effects on turbulence with simple disturbance elements. In the evaluation of the streamwise disturbance velocity, he compared stream filaments that entered the flow contraction at different velocity levels. Assuming that the gain in kinetic energy due to the flow contraction is the same for both filaments, he concluded that the disturbance velocity decreased proportional to the inverse of the contraction ratio, which is the ratio between the post- and pre-contraction mean flow velocities. For the disturbance velocity normal to the mean flow he investigated a cylindrical element with the axis of rotation parallel to the mean flow. Based on the assumption of conservation of angular momentum, he found that the disturbance velocity increased proportional to the square root of the contraction ratio.

A more sophisticated model was introduced by Taylor (Ref 29). He related pre- and post-contraction vorticity through Cauchy's transport equations for vorticity and introduced one of the key assumptions used in all contraction models: the relative motion between neighboring particles due to turbulence must be small in comparison with the relative motion due to the flow contraction. Taylor found explicit solutions for simple, cellular vorticity distributions.

Ribner and Tucker (Ref. 17) and Batchelor and Proudman (Ref. 30) used Taylor's approach and investigated the effect of a flow contraction on isotropic turbulence. They showed that for this type of turbulence the contraction effect on the turbulence variances is independent of the initial spectral distribution. Ribner and Tucker also investigated the effect of an axisymmetric contraction on initially isotropic turbulence with a spectral distribution based on the Dryden spectra.

The turbulence model used in the present investigation is basically the one described in Reference 17. However, additional one-dimensional, post-contraction spectra have been derived.

4.2.2 REVIEW OF ANALYSIS

An accelerating flow field stretches fluid elements in the streamwise direction and causes them to contract laterally. The sides of a cubical element change from D to $\ell_1 D$, $\ell_2 D$ and $\ell_3 D$ as it travels from the pre-contraction position A to the post-contraction position B (Fig. 11). ℓ_1 is defined as the mean velocity or contraction ratio and ℓ_2 and ℓ_3 are the lateral contraction ratios. They are related through the continuity equation

$$\sigma \cdot \ell_1 \cdot \ell_2 \cdot \ell_3 = 1 \quad \ell_1 = \frac{U_B}{U_A} \qquad \sigma = \frac{\rho_B}{\rho_A} \tag{4.2.01}$$

with σ the density ratio.

A separation vector between two fluid particles will change from $\vec{x}_A$ to $\vec{x}_B$ as it is convected from A to B, with

$$x_{iB} = \ell_i \cdot x_{iA} \tag{4.2.02}$$

Fluid filaments are therefore turned into the mean flow direction, unless they are aligned perfectly normal to the mean flow.

The analysis described by Ribner and Tucker in Reference 17, is based on the following assumptions.

- The relative motion between neighboring particles due to turbulence is negligible in comparison with the relative motion due to the flow contraction.
- The contraction is rapid enough so that inertial effects dominate and viscous effects become negligible.
- The lateral dimension of the flow field is large in comparison with the turbulence scale.
- The mean flow field is one-dimensional.
- Density fluctuations due to turbulence are negligible.

Some of these assumptions are in conflict with each other. A rapid distortion for instance will provide one-dimensional flow only on the axis of the flow contraction. The requirement of turbulence scales small in comparison with the lateral dimension of the flow contraction will result in small scales which in turn may lead to turbulence dissipation in the contraction. But, despite these shortcomings, this analysis is one of the most appropriate tools to evaluate the inflow contraction effects on atmospheric turbulence.

The analysis is based on the assumption of conservation of circulation. Cauchy's transport equations for vorticity in Lagrangian form are used to define the post-contraction vorticity Ω_B based on the initial vorticity Ω_A and the mean flow contraction.

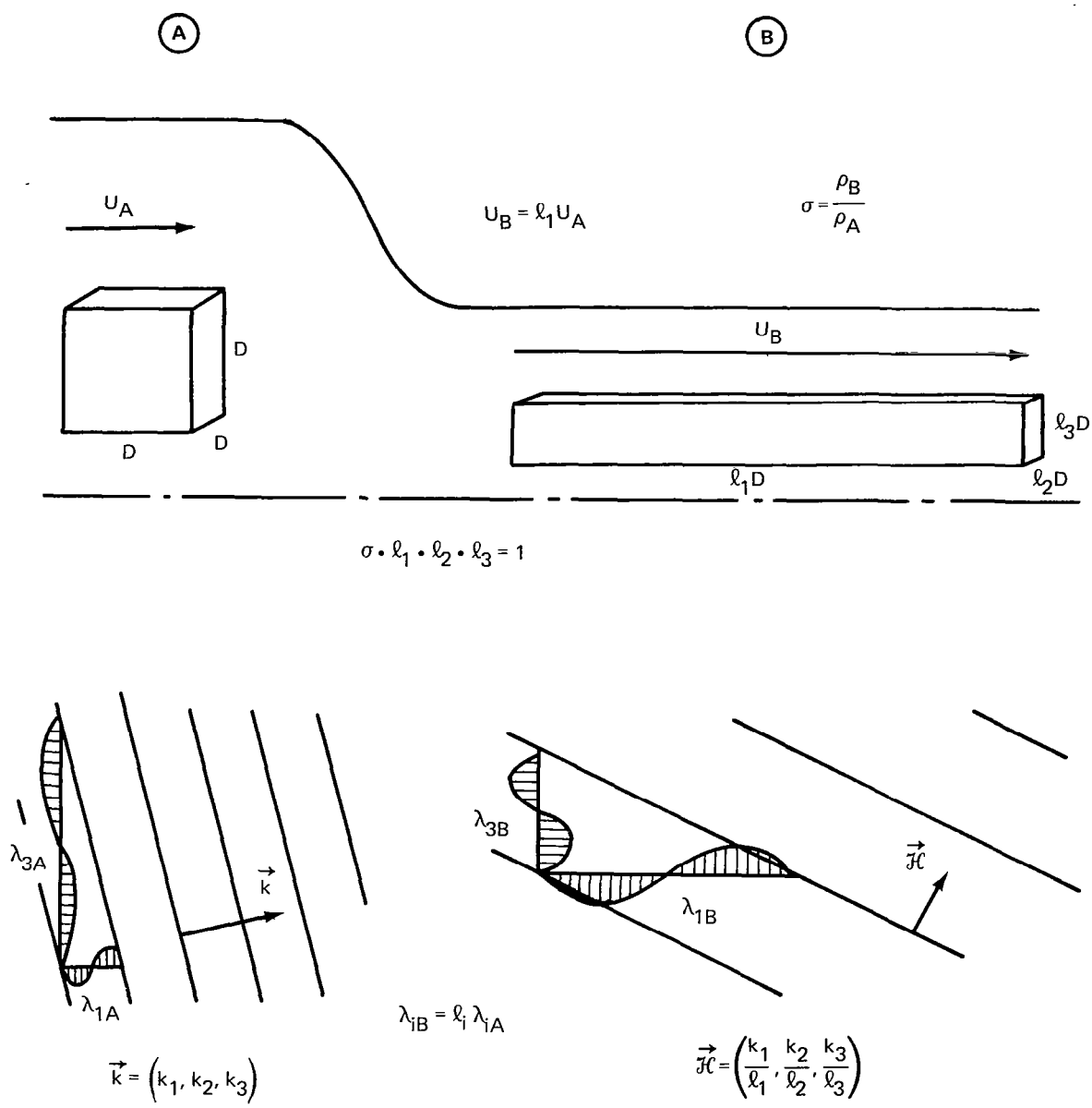

Figure 11.—Linear Transformation of Velocity Waves in a Flow Contraction

$$\Omega_i^B = \sigma \left(\Omega_1^A \frac{\partial x_{iB}}{\partial x_{1A}} + \Omega_2^A \frac{\partial x_{iB}}{\partial x_{2A}} + \Omega_3^A \frac{\partial x_{iB}}{\partial x_{3A}} \right) \tag{4.2.03}$$

Due to the assumption of one-dimensional mean flow and negligible relative motion due to turbulence, the distortion tensor reduces to its diagonal elements and the vorticity equations become

$$\Omega_i^B = \sigma \, \Omega_i^A \frac{\partial x_{iB}}{\partial x_{iA}} \quad \text{with} \quad \frac{\partial x_{iB}}{\partial x_{iA}} = \ell_i \tag{4.2.04}$$

These equations, together with the continuity equation, describe the contraction effect on turbulence. Due to the linearizing assumptions each turbulence wave (each Fourier component of the turbulence field) has to satisfy this system of equations. A Fourier component of the turbulence field at the pre-contraction location is represented by

$$u_i^A = Q_i^A \, e^{i\vec{k}\vec{x}_A} \tag{4.2.05}$$

The relative motion due to turbulence is negligible throughout the contraction and this turbulence wave is transformed into

$$u_i^B = Q_i^B \, e^{i\vec{\mathcal{K}}\vec{x}_B} \tag{4.2.06}$$

at the exit of the contraction. The wavenumber vectors are related by

$$\mathcal{K}_i = \frac{2\pi}{\ell_i \lambda_i} = \frac{k_i}{\ell_i} \tag{4.2.07}$$

See also Figure 11.

The amplitude vector Q for the Fourier components is determined with the continuity and vorticity equations

$$Q_i^B = \frac{1}{\ell_i} \left(Q_i^A - \sum_{j=1}^{3} Q_j^A \frac{k_j \, k_i}{\ell_j^2 \, \mathcal{K}^2} \right) \tag{4.2.08}$$

Based on these relationships Ribner and Tucker derived the equation for the components of the three-dimensional spectrum tensor $\Gamma_{ij}(\vec{\mathcal{K}})$. For an axisymmetric contraction $(\ell_2 = \ell_3)$, it assumes the following form:

$$\Gamma_{ij}{}^{B}(\vec{\mathcal{K}}) = \frac{\ell_1 \ell_2{}^2}{\ell_i \ell_j} \left[\Gamma_{ij}{}^{A} + \frac{\left(\Gamma_{i1}{}^{A} k_j + \Gamma_{1j}{}^{A} k_i\right) k_1 (1-\epsilon)}{\epsilon k_1{}^2 + k_2{}^2 + k_3{}^2} \right.$$

$$\left. + \frac{\Gamma_{11}{}^{A} k_1{}^2 k_i k_j (1-\epsilon)^2}{\left(\epsilon k_1{}^2 + k_2{}^2 + k_3{}^2\right)^2} \right] \qquad (4.2.09)$$

with

$$\epsilon = \frac{\ell_2{}^2}{\ell_1{}^2} \qquad (4.2.10)$$

The components of the three-dimensional spectrum tensor $\Gamma_{ij}{}^{B}(\vec{\mathcal{K}})$ are expressed as a function of the contraction ratios and the corresponding pre-contraction tensor. Further simplifications are possible if the pre-contraction turbulence is isotropic. The pre-contraction spectra then assume the following form:

$$\Gamma_{ij}{}^{A}(k) = G(k) \left(k^2 \partial_{ij} - k_i k_j\right) \qquad (4.2.11)$$

with

$\partial_{ij} = 1.$ for $i = j$

$.0$ for $i \neq j$

The spectrum function G (k), characterizes the spectral distribution of the turbulence. For such pre-contraction turbulence, the diagonal terms in the post-contraction spectrum tensor are

$$\Gamma_{11}{}^{8}(\vec{\mathcal{K}}) = \frac{\ell_2{}^2}{\ell_1} \; G(k) \frac{\left(k^2 - k_1{}^2\right) k^4}{\left(\epsilon k_1{}^2 + k_2{}^2 + k_3{}^2\right)^2} \qquad (4.2.12)$$

$$\Gamma_{22}{}^{B}(\vec{\mathcal{K}}) = \ell_1 \, G(k) \left[k^2 - k_2{}^2 - \frac{2 k_1{}^2 k_2{}^2 (1-\epsilon)}{\epsilon k_1{}^2 + k_2{}^2 + k_3{}^2} \right.$$

$$\left. + \frac{k_1{}^2 k_2{}^2 \left(k^2 - k_1{}^2\right)(1-\epsilon)^2}{\left(\epsilon k_1{}^2 + k_2{}^2 + k_3{}^2\right)^2} \right] \qquad (4.2.13)$$

$\Gamma_{33}^{B}(\vec{\mathcal{K}})$ assumes the same form as $\Gamma_{22}(\vec{\mathcal{K}})$ since the initial turbulence is isotropic and the contraction is axisymmetric.

Three-dimensional spectra provide extremely detailed information about the turbulence field, since the independent variable is a vector. It is, however, difficult to present them and takes an infinite number of standard two-point measurements to determine them experimentally.

Standard one or two-point turbulence measurements provide only one-dimensional spectra, with a single wave-number component as the independent variable. They represent the power of all waves with a given wavenumber component independent of the magnitude of the other two wave number components. They are determined by integration of the three-dimensional spectra over two wavenumber components.

$$F_i^A(k_j) = 2 \iint_{-\infty}^{\infty} \Gamma_{ii}^A(\vec{k})\, \partial k_i\, \partial k_k \qquad (4.2.14)$$

For a given spectrum function G (k), the one-dimensional post-contraction spectra can be determined by integration of the three-dimensional spectra given in equations (4.2.12) and (4.2.13). This integration is however only possible for simple spectrum functions.

One dimensional spectra, that are frequently used to describe turbulence at large Reynolds numbers, are based on the following spectrum function

$$G(k) = \frac{N}{\left(k^2 + \gamma^2\right)^3} \qquad (4.2.15)$$

where N and γ are constants related to the turbulence variance and integral scale (Ref. 17).

$$N = \frac{2}{\pi^2}\,\frac{\sigma^2}{L} \qquad \gamma = \frac{1}{L} \qquad (4.2.16)$$

with

σ = turbulence variance
L = turbulence integral scale

The one-dimensional spectra for the isotropic, pre-contraction turbulence based on this spectrum function are frequently referred to as the Dryden spectra.

$$F_i^A(k_i) = \frac{\pi N}{\left(k_i^2 + \gamma^2\right)} \qquad (4.2.17)$$

$$F_i^A(k_j) = \frac{\pi N\left(3k_j^2 + \gamma^2\right)}{2\left(k_j^2 + \gamma^2\right)^2} \tag{4.2.18}$$

The corresponding post-contraction spectra can be derived with equations (4.2.12) through (4.2.15). They form a matrix of nine spectra

$$F_1^B(\mathcal{K}_1) \quad F_1^B(\mathcal{K}_2) \quad F_1^B(\mathcal{K}_3)$$

$$F_2^B(\mathcal{K}_1) \quad F_2^B(\mathcal{K}_2) \quad F_2^B(\mathcal{K}_3)$$

$$F_3^B(\mathcal{K}_1) \quad F_3^B(\mathcal{K}_2) \quad F_3^B(\mathcal{K}_3)$$

It can be shown that all the corresponding cross spectra are zero. Due to the isotropic initial conditions and the axisymmetric contraction the following equivalences exist:

$$F_1^B(\mathcal{K}_2) = F_1^B(\mathcal{K}_3) \quad F_2^B(\mathcal{K}_1) = F_3^B(\mathcal{K}_1)$$

$$F_2^B(\mathcal{K}_2) = F_3^B(\mathcal{K}_3) \quad F_2^B(\mathcal{K}_3) = F_3^B(\mathcal{K}_2)$$

The entire matrix is therefore determined by five spectra. Two of them $F_1(\mathcal{K}_1)$ and $F_2(\mathcal{K}_1)$ have been derived by Ribner and Tucker. They only provide information about the streamwise correlation of the turbulence. In the generation of rotor tone noise due to convected turbulence, the streamwise as well as the transverse correlations in the turbulence field are significant. For this reason, the remaining three spectra have been derived to complete the matrix. The derivation and the resulting equations are quite lengthy and are presented in the Appendix.

The integral length scales at the post-contraction location are computed with the value of the corresponding spectrum at the wavenumber origin.

$$L_{ij} = \frac{\pi}{2} \cdot \frac{F_i(\mathcal{K}_j = .0)}{\sigma_i^2} \tag{4.2.19}$$

The effect of an axisymmetric contraction on the variance of the initially isotropic turbulence is determined by integration of the three-dimensional spectra in equations (4.2.12) and (4.2.13) over all three wavenumber components. The results as derived by Ribner and Tucker are:

$$\frac{\sigma_{1B}^2}{\sigma_{1A}^2} = \frac{3}{4\,\ell_1^2}\left[-\frac{1}{1-\epsilon} + \frac{2-\epsilon}{(1-\epsilon)^{3/2}}\ \tanh^{-1}\sqrt{1-\epsilon}\right] \tag{4.2.20}$$

$$\frac{\sigma_{2B}^2}{\sigma_{2A}^2} = \frac{3}{8\,\ell_2^2}\left[\frac{2-\epsilon}{1-\epsilon} - \frac{\epsilon^2}{(1-\epsilon)^{3/2}}\ \tanh^{-1}\sqrt{1-\epsilon}\right] \tag{4.2.21}$$

The correlation functions are determined by Fourier transformation of the one-dimensional spectra.

$$R_i\left(x_j\right) = \int_o^\infty F_i\left(k_j\right) \cos k_j\, x_j\, \partial k_j \tag{4.2.22}$$

Correlation functions, as well as spectra, have been normalized with the turbulence variances and integral scales

$$C_i\left(\frac{x_j}{L_{ij}}\right) = \frac{1}{\sigma_i^2}\ R\left(\frac{x_j}{L_{ij}}\right) \tag{4.2.23}$$

$$F_i\left(\mathcal{K}_j\, L_{ij}\right)\frac{1}{\sigma_i^2} = \frac{\ell_j}{L_{ij}\,\sigma_i^2}\ F_i\left(k_j\right) \tag{4.2.24}$$

Equations (4.2.17) through (4.2.24) have been programmed and results are presented in the following section. The remaining integrals in the equations for the correlation functions are solved by numerical methods.

4.2.3 RESULTS

A limited parametric study has been conducted to evaluate the effects of the fan inflow field contraction on convected turbulence. The mean flow Mach numbers in this inflow field are reasonably small, (less than .6). The results indicate that for this range of Mach numbers the compressibility effects on the turbulence transformation are negligible. The results are therefore only a function of the contraction ratio, independent of the absolute Mach number levels. The results are presented as a function of the contraction ratio ℓ_1, the mean flow velocity ratio.

Turbulence Standard Deviation

The effects of the inflow contraction on the standard deviations of the turbulence components are shown in Figure 12. Results based on Prandtl's and Ribner and Tucker's equations are compared. They demonstrate the reasonably good agreement between the two models. Prandtl's simple model seems to overestimate the effects of the inflow contraction. Both models show that the total turbulent energy increases with the contraction ratio. In the positive strain field of the flow contraction, the streamwise vorticity component absorbs energy from the mean flow field. The concurrent energy release from the other vorticity components, which are exposed to a negative strain field, is smaller and a net gain in turbulent energy results. Experimental and analytical data are compared in Figure 13. Uberoi's data were measured in a wind tunnel flow contraction (Ref. 31). The engine inflow field data are based on turbulence measurements in the inflow field of a statically operated engine, outside of the inlet and upstream of the highlight plane (Ref. 32). The fan face data represent turbulence measurements made during a recent joint P&WA and Boeing noise reduction program. The turbulence was measured with split film anemometers at the fan face of a statically operated JT9D engine. The results demonstrate the increase in the separation between the standard deviations of the turbulence components with the contraction ratio. The discrepancy between the analytical and experimental results is mainly due to the insufficient attenuation of the streamwise turbulence component. It has been suggested, that this is due to:

- the tendency of turbulence to change towards isotropy
- the decay of turbulent energy within the contraction
- the contamination of the hot wire anemometer signal representing the streamwise turbulence component by acoustic signals and density fluctuations in highly anisotropic turbulence.

Integral Length Scales

The effect of a flow contraction on the integral scales is shown in Figure 14. The lines labeled ℓ_1 and ℓ_2 represent the streamwise and transverse contraction ratios and therefore represent the simple deformation model of Figure 11. The integral scales are normalized with the scale parallel to the turbulence component in the initial isotropic condition. Depending on their orientation relative to the turbulence component, they assume a value of 1. or .5 in the isotropic conditions.

The integral scales L_{21} and L_{22} of the transverse turbulence component follow the corresponding contraction ratios quite closely. The third integral scale for the transverse component drops off very rapidly. This is due to significant negative values in the correlation function at large separation distances.

The effects of the flow contraction on the integral scales of the streamwise component cannot be explained with the simple deformation model. The streamwise scale L_{11} increases at a slower than expected rate and the transverse scale L_{12} increases rather than decreases with the contraction ratio. Both reflect the fact that the effects of the contraction on the turbulence are wave number dependent.

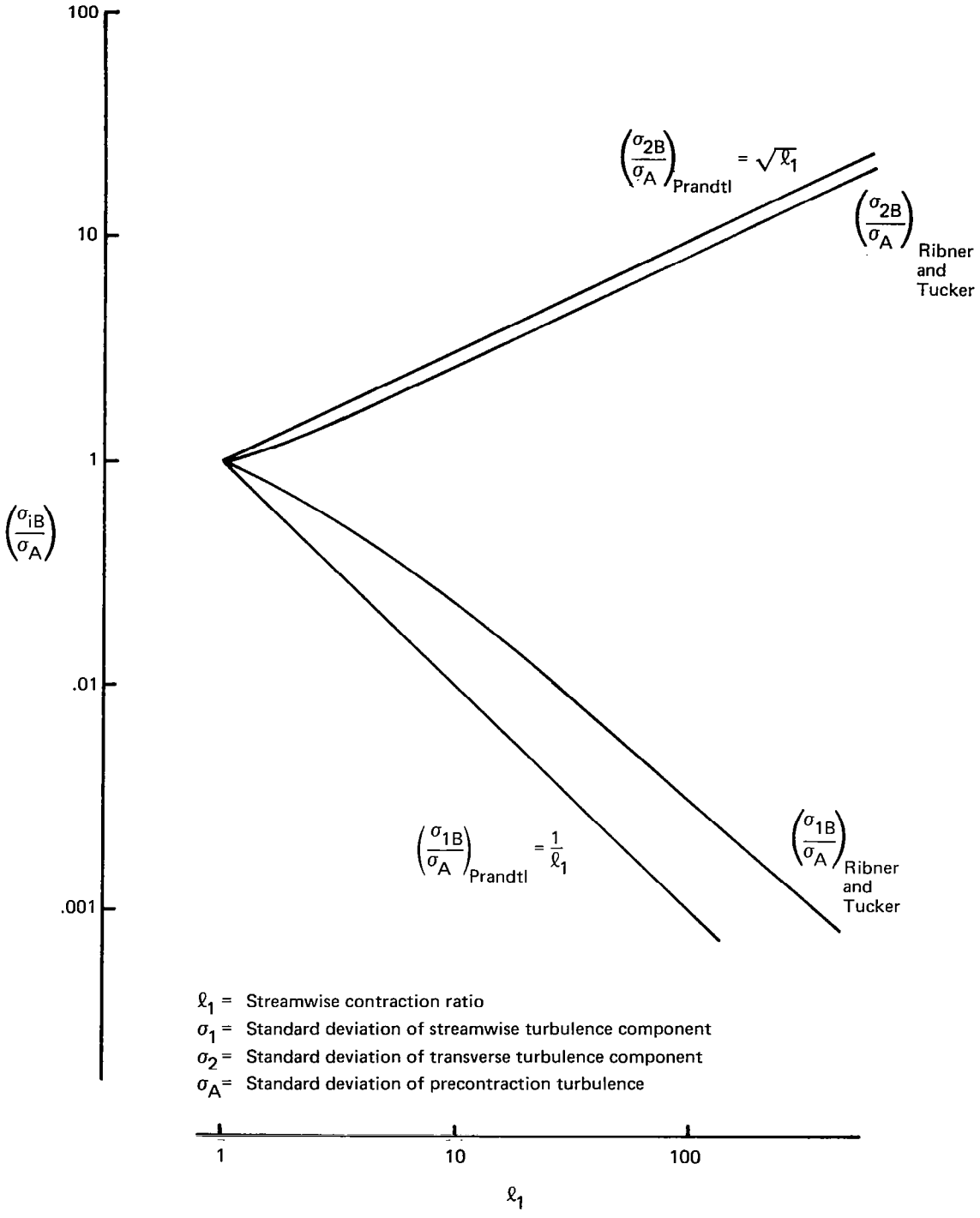

Figure 12.—Effect of Flow Contraction on Standard Deviation of Turbulence

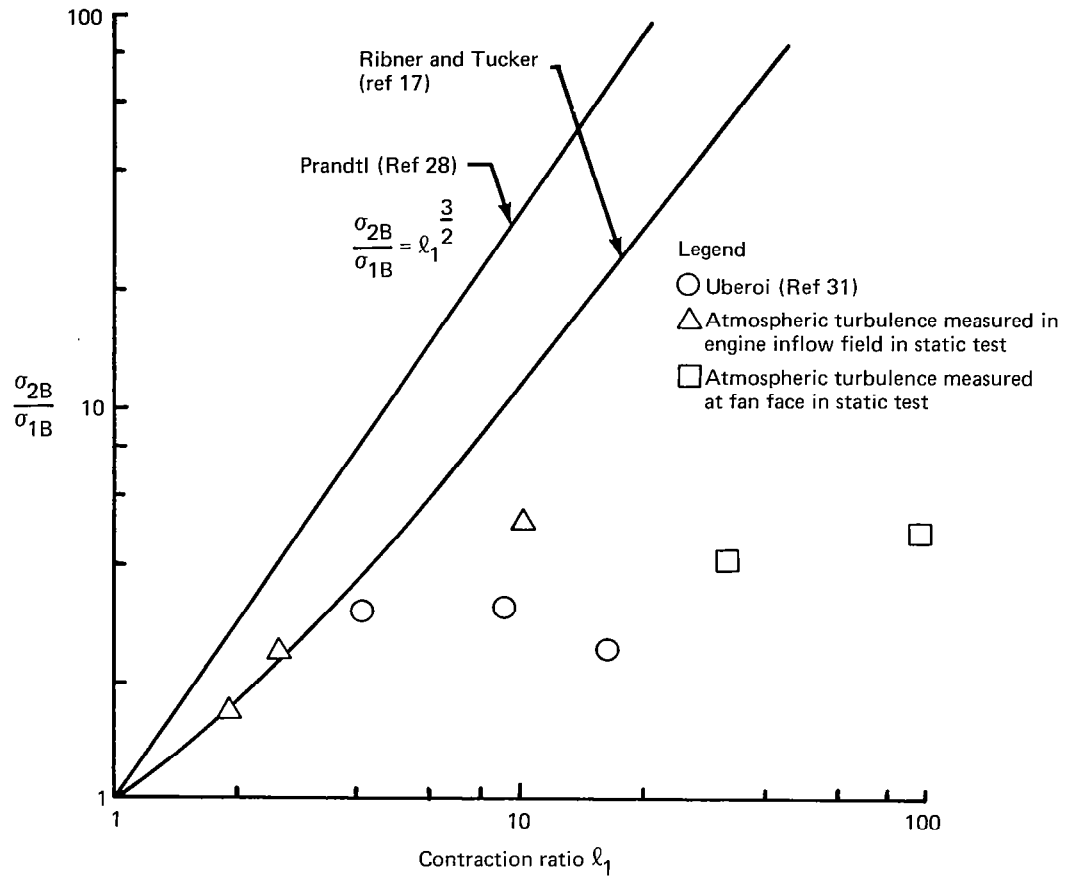

Figure 13.—Ratio Between the Standard Deviations of the Turbulence Velocities in a Flow Contraction

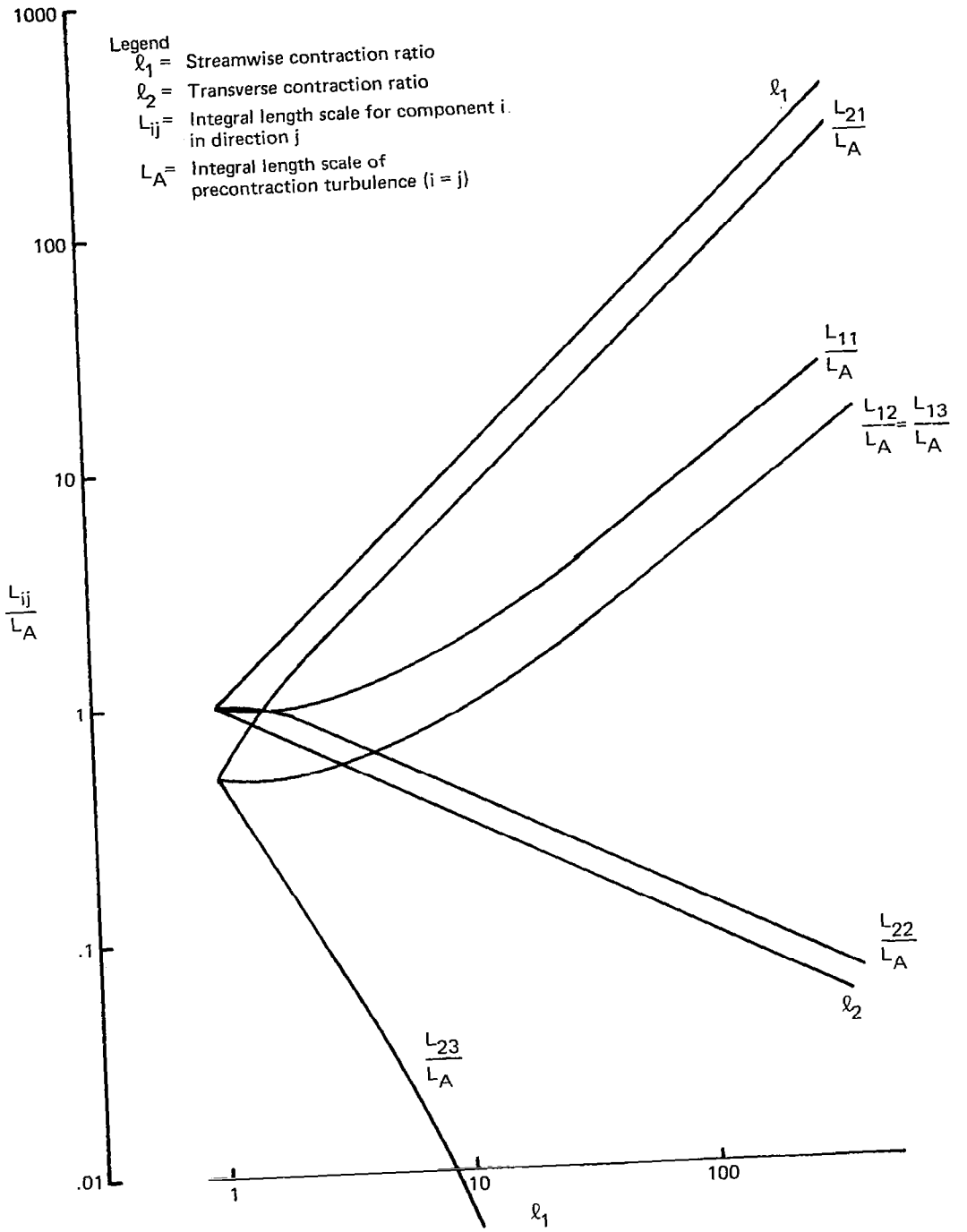

Figure 14.—Effect of Flow Contraction on Turbulence Integral Length Scales

One Dimensional Spectra

The effect of the flow contraction on the one dimensional turbulence spectra is shown in Figures 15 through 18. The spectra in Figures 15 and 16 are normalized with the precontraction variance and length scale and are presented as a function of the streamwise component of the precontraction wave number. The spectra of the transverse turbulence component in Figure 15 show an almost uniform energy increase (independent of wave number) with increasing contraction ratios. The energy increment seems to be wavenumber dependent only for contraction ratios smaller than about 3. The spectra for the streamwise component in Figure 16 demonstrate the significant decrease in the spectrum levels with increasing contraction ratio, as well as a significant change in the spectral distribution of the turbulent energy. This change in the spectral distribution is due to the energy transfer between the turbulence components. At large contraction ratios, it is apparent only in the spectra of the streamwise component, since its energy levels are much lower than the ones for the transverse components.

Figure 17 shows the three one-dimensional post-contraction spectra for the transverse turbulence component. They are normalized with the post-contraction variances and integral length scales and show that the changes in the spectral distributions take place in the initial segment of the contraction (ratios less than 3.). The changes in the spectra $F_2(\mathcal{H}_1)$ and $F_2(\mathcal{H}_2)$ are minimal, but they are significant for $F_2(\mathcal{H}_3)$. Spectra such as the post-contraction spectrum $F_2(\mathcal{H}_3)$ are typical for unidirectional vortex fields as will be shown in Section 4.3. The corresponding spectra for the streamwise turbulence component in Figure 18 demonstrate that the spectral distribution changes up to the largest contraction ratios. These changes will however not be of much concern due to the fact that the streamwise component loses its energy and its significance decreases rapidly with increasing contraction ratios.

Correlation Coefficients

The three correlation coefficients for the transverse turbulence component are shown in Figure 19. The post-contraction coefficients represent results for contraction ratios larger than 3. The abscissa for the pre-contraction coefficients are all normalized with the same integral length scale L_A, measured parallel to the turbulence component. For the post-contraction coefficients it is normalized with integral length scales L_{21} and L_{22}. Only the third correlation coefficient is significantly affected by the contraction. It represents the transverse correlation in the direction normal to the turbulence velocity component and exhibits significant negative correlations at large separation distances.

During a test program jointly conducted by P&WA and Boeing, turbulence data were acquired with split film anemometers in the inlet of a statically operated JT9D engine. Several sensors located on a radial strut measured the transverse circumferential turbulence component. Correlation between the different sensors provided information about the radial correlation of the turbulence. The results are presented in Figure 20 and exhibit large negative values at large radial separations. They therefore agree qualitatively with the predictions of the inflow contraction model.

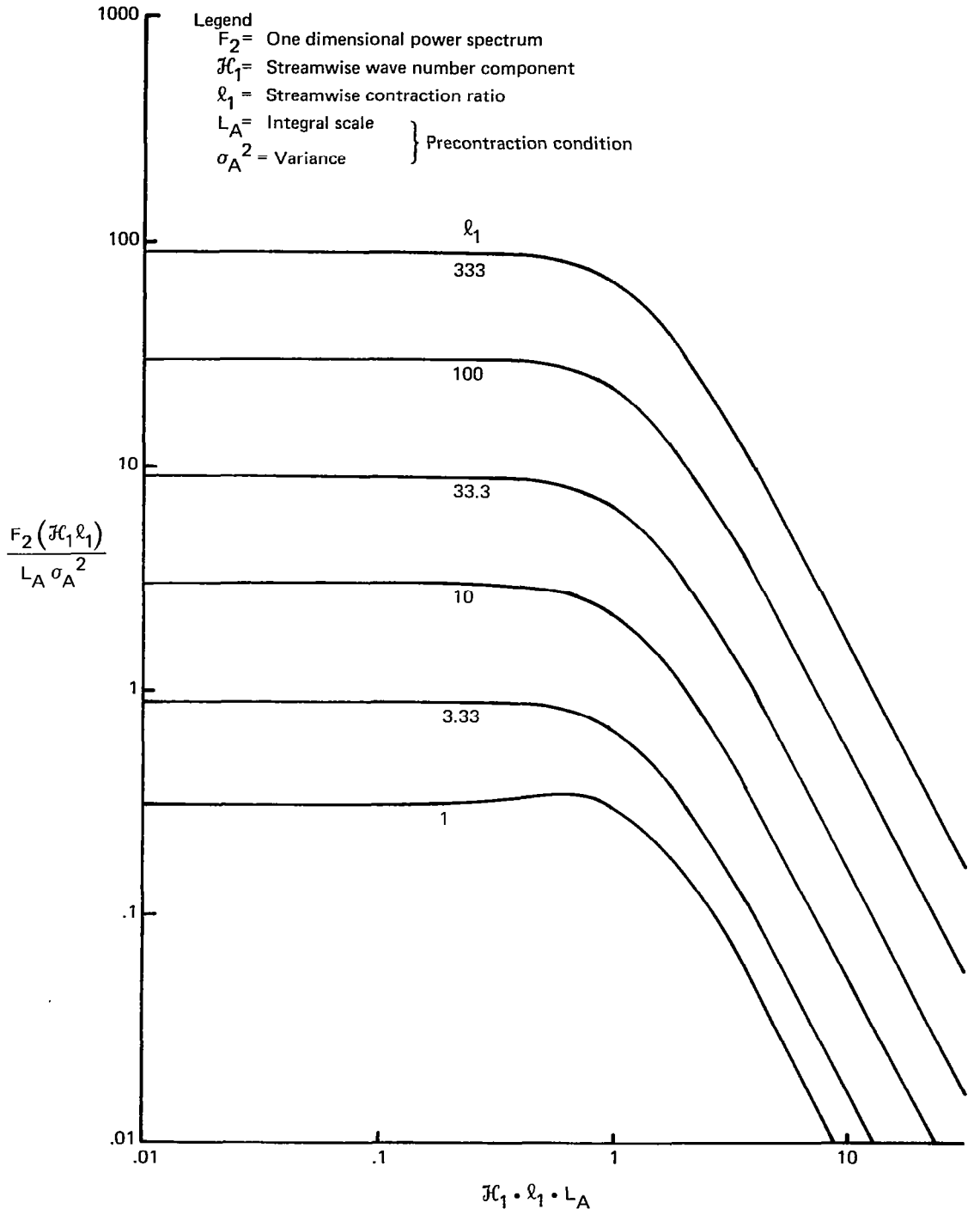

Figure 15.—Effect of Flow Contraction on Spectra of the Transverse Turbulence Component

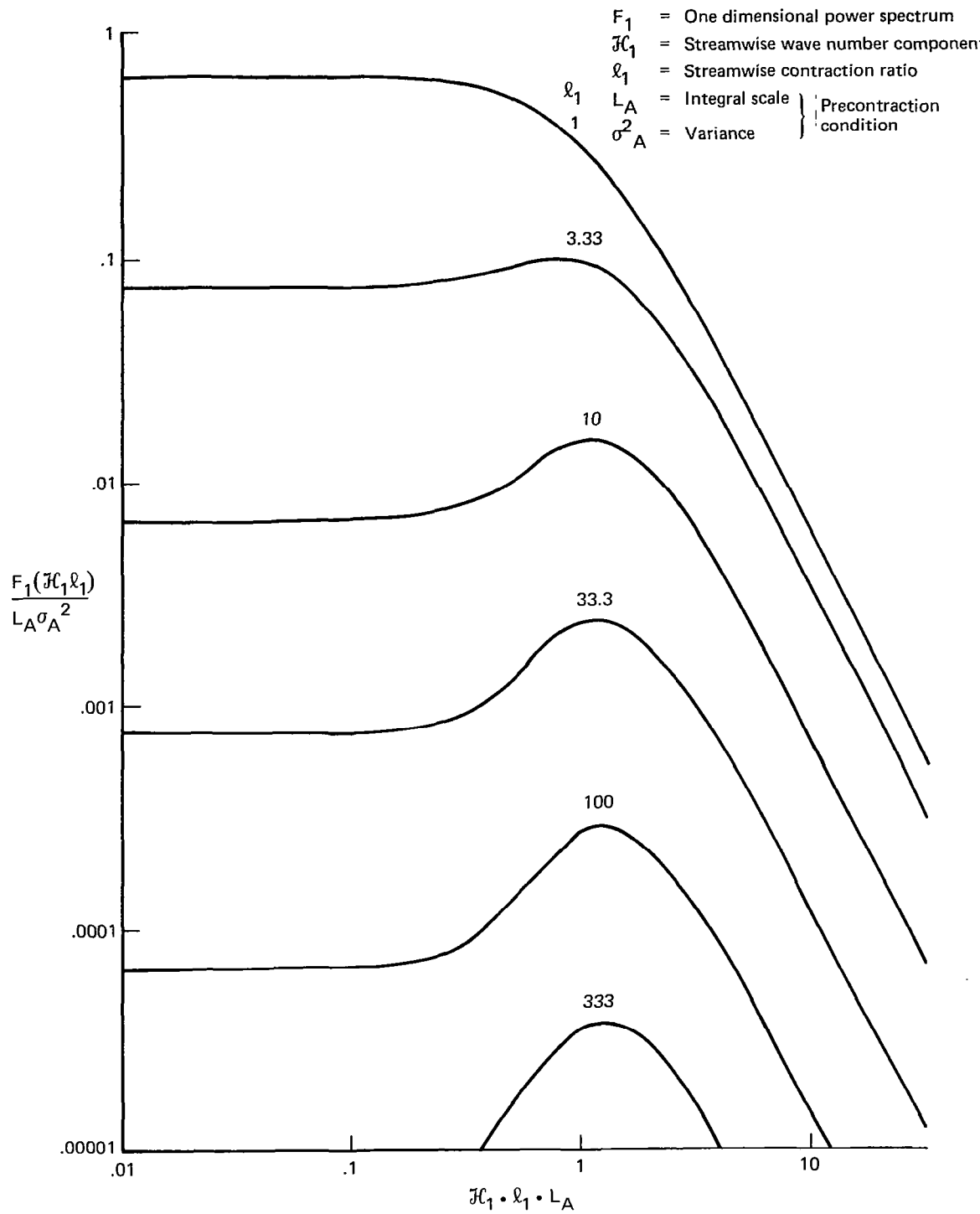

Figure 16.—Effect of Flow Contraction on Spectra of Streamwise Turbulence Component

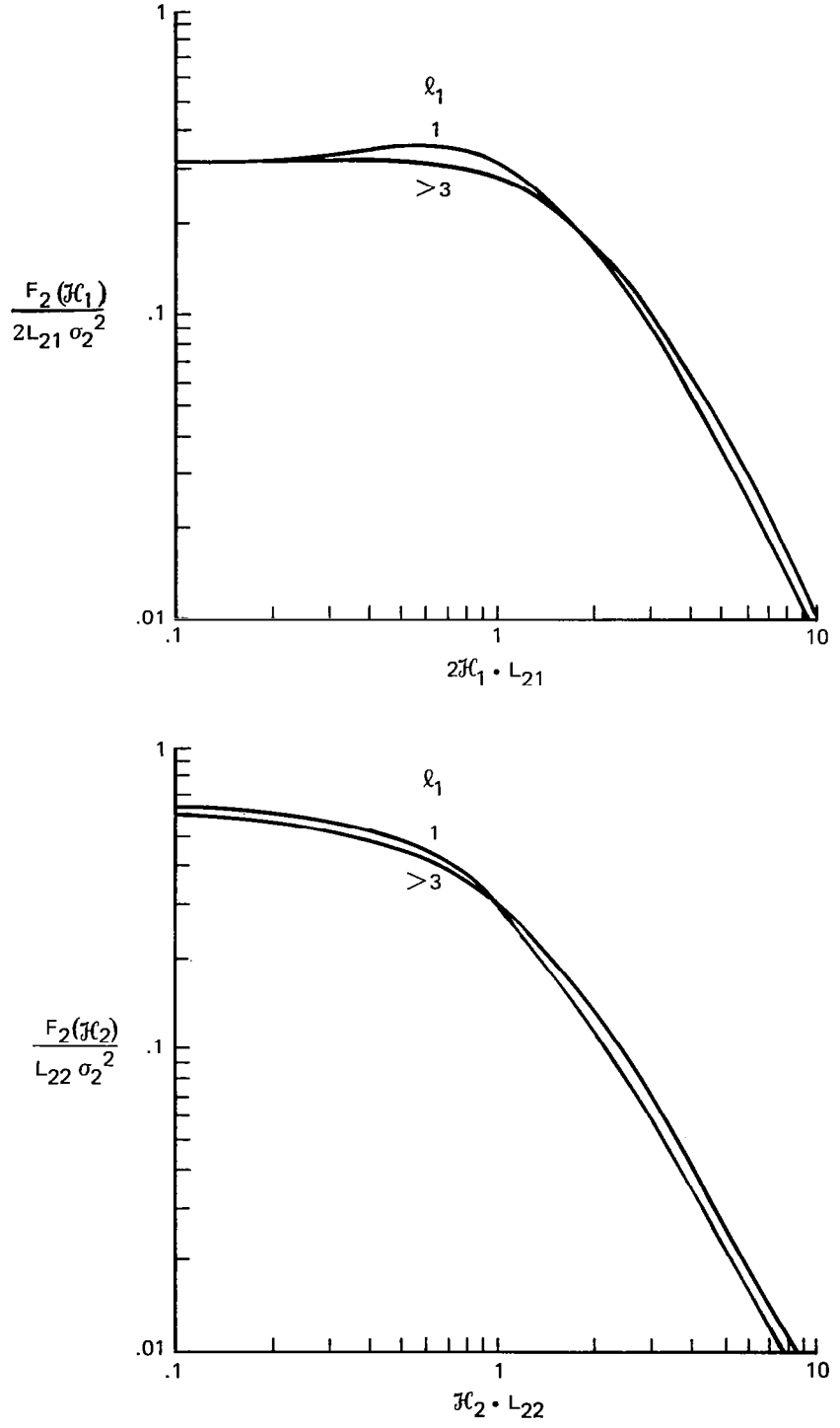

Figure 17.—Normalized Pre- and Post-Contraction Spectra for the Transverse Turbulence Component for Various Contraction Ratios ℓ_1

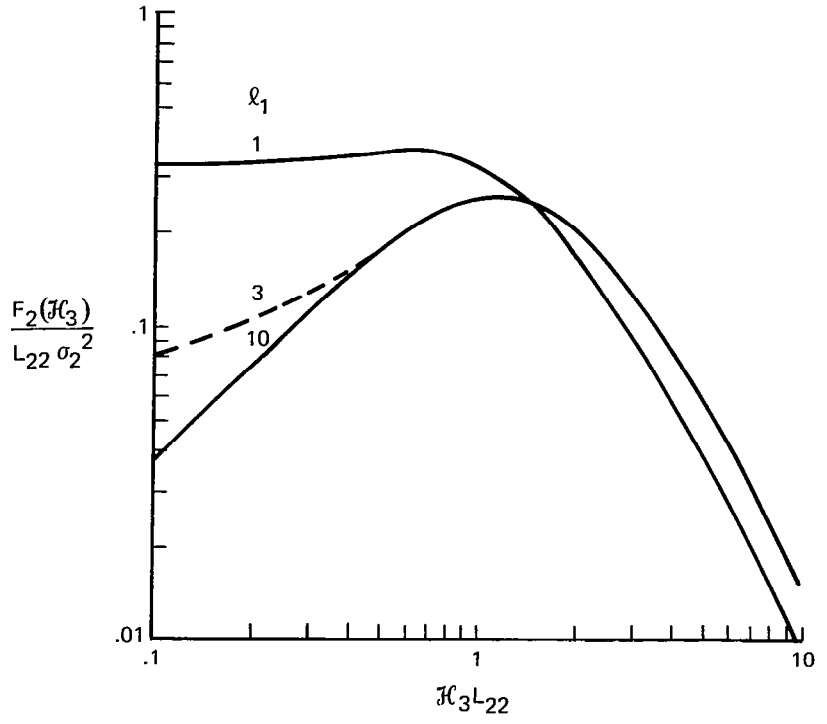

Figure 17.—(Concluded)

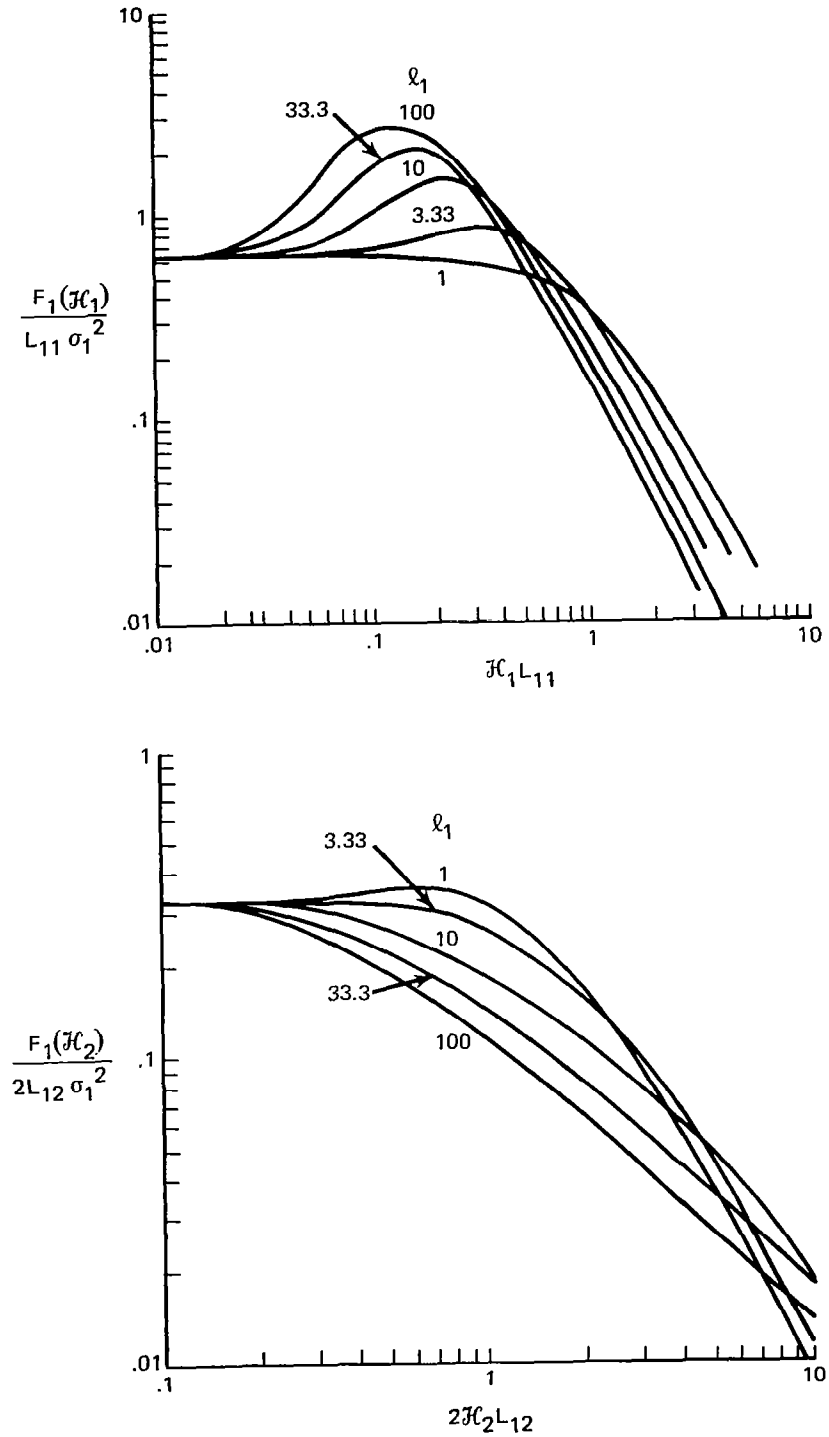

Figure 18.—Normalized Pre- and Post-Contraction Spectra for the Streamwise Turbulence Component for Various Contraction Ratios ℓ_1

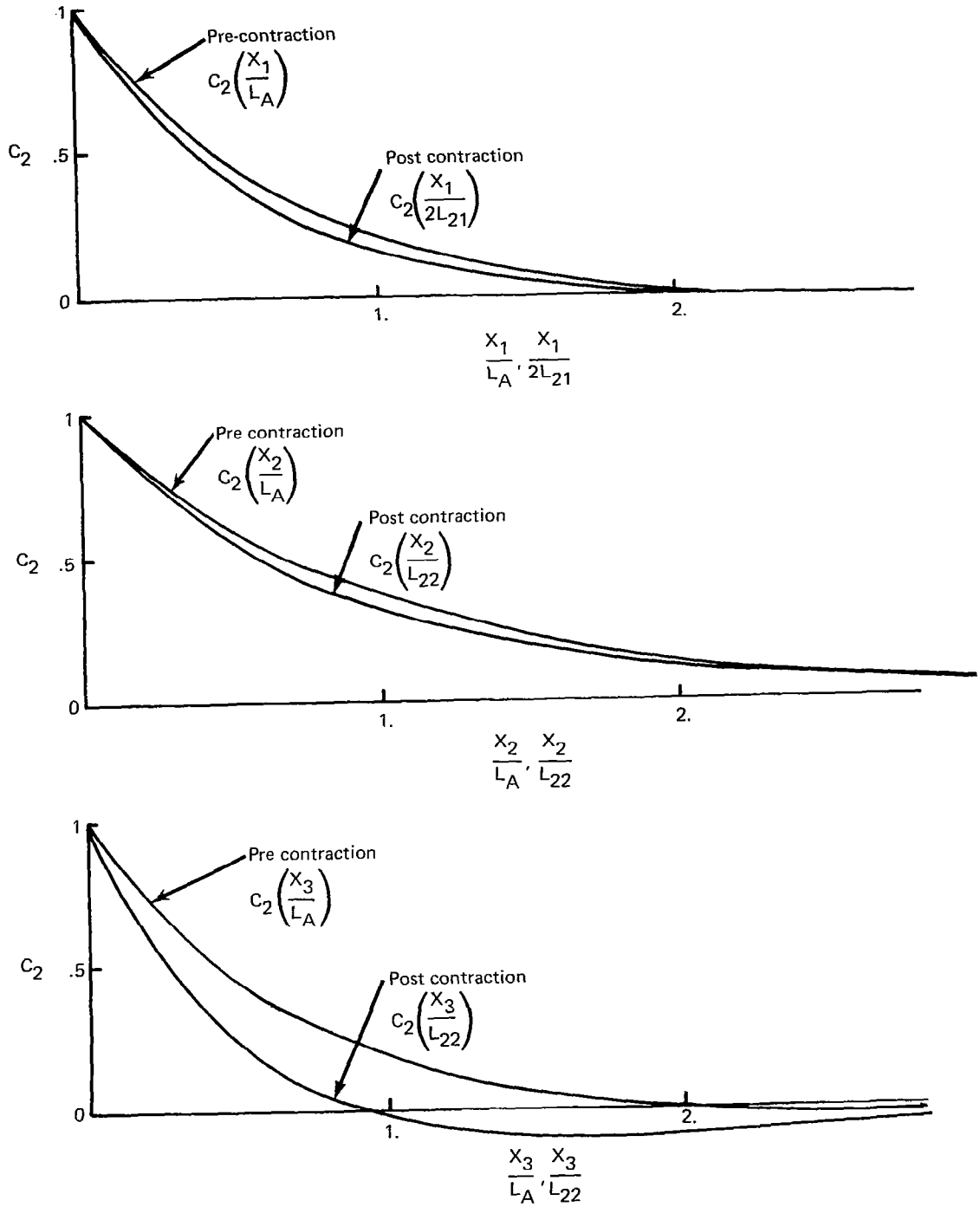

Figure 19.—Pre- and Post-Contraction Correlation Coefficients for the Transverse Turbulence Component

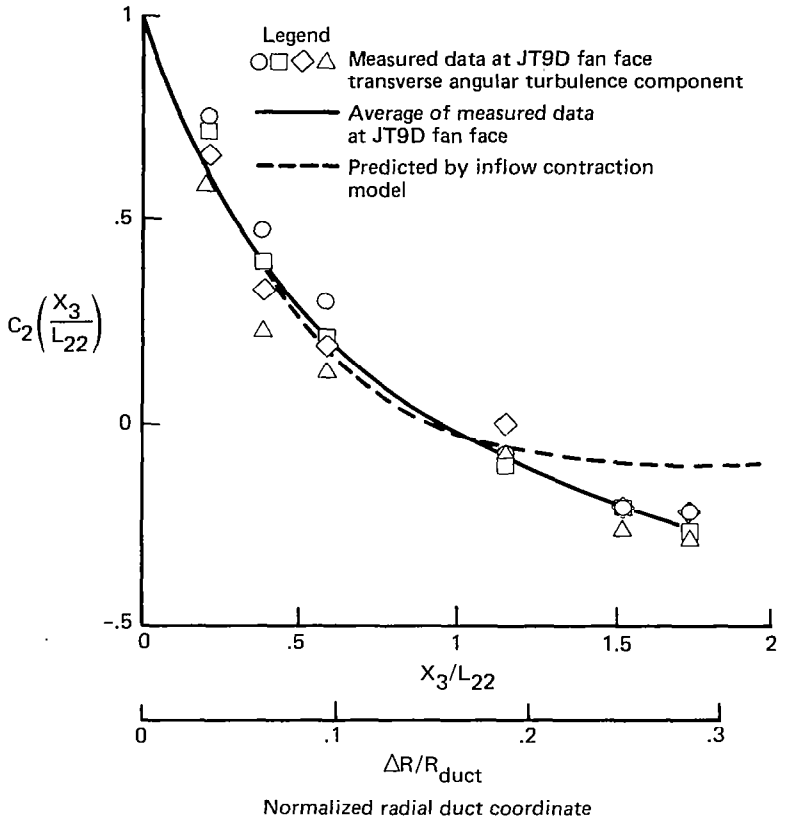

Figure 20.--Comparison of Measured and Predicted Post-Contraction Correlation Coefficients for the Transverse Turbulence Component

4.3 INFLOW TURBULENCE REPRESENTATION

4.3.1 BACKGROUND

The evaluation of blade passage frequency noise due to convected atmospheric turbulence is based on analytical models developed by T.L. Clark at The Boeing Company (Refs. 33 and 34). In these models, the convected turbulence is represented by a homogeneous distribution of distortion elements. The turbulence field at the fan face as predicted by the combined models of Sections 4.1 and 4.2 is however presented in the form of one-dimensional spectra and correlations. To bridge this gap, an inflow turbulence model has been developed, that computes the one-dimensional spectra and correlations for random distributions of distortion elements. This model, which is described in this section, makes it possible to select the distributions of distortion elements that best simulate a given inflow turbulence field.

The model is based on an approach similar to the one used by Melick in Reference 35. Melick's model was developed for the study of compressor stall due to turbulence in the subsonic diffusor of supersonic inlets. The model attempts to simulate the turbulence resulting from the inlet boundary layer and shock-boundary layer interactions. It is based on a two-dimensional flow field and the distortion elements are axisymmetric vortices with their axis normal to the mean flow velocity.

The turbulence model presented here describes the atmospheric turbulence at the fan face after it has been affected by a flow contraction. The distortion elements are axisymmetric with their axis parallel to the mean flow velocity. Their distribution is homogeneous in unbounded, three-dimensional space. The effects of inlet surfaces are neglected.

4.3.2 ANALYSIS

The acoustic models used in this study compute the tone noise resulting from distortion elements that are convected through a fan. In these models, it is assumed that only two unsteady velocity components contribute to fan tone noise, the streamwise component u and the transverse circumferential or angular component v. In the original report (Ref. 33) that describes these models, the distortion elements are represented as Gaussian eddies. The velocity distribution in such eddies is

$$u(\vec{x}) = c_1 \, e^{-\frac{1}{2}\left(\frac{x_1}{\ell}\right)^2} \, e^{-\frac{1}{2}\left(\frac{x_2^2 + x_3^2}{a^2}\right)} \qquad (4.3.01)$$

with

c_1 = velocity scale

ℓ = streamwise length scale

a = transverse length scale

(See also Fig. 21). These Gaussian eddies are used to describe unsteady velocities in the streamwise as well as the transverse direction.

Gaussian eddy

$$U_2 = C_1 e^{-\frac{1}{2}\left(\frac{Ut}{\ell}\right)^2} e^{-\frac{1}{2}\left(\frac{X_2^2 + X_3^2}{a^2}\right)}$$

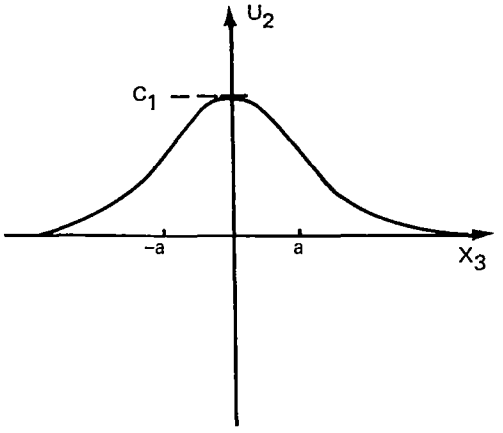

Vortex

$$U_\phi = C_1 \frac{r}{a} e^{-\frac{1}{2}\left(\frac{Ut}{\ell}\right)^2} e^{-\frac{1}{2}\left[\left(\frac{r}{a}\right)^2 - 1\right]}$$

$$U_2 = C_1 \frac{X_3}{a} e^{-\frac{1}{2}\left(\frac{Ut}{\ell}\right)^2} e^{-\frac{1}{2}\left[\frac{X_2^2 + X_3^2}{a^2} - 1\right]}$$

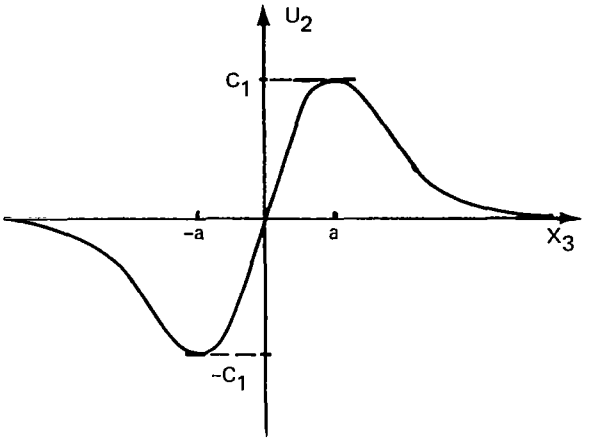

Transverse velocity distribution normal to the turbulence velocity

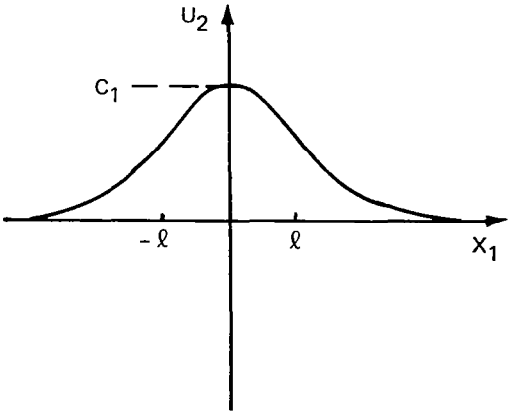

Streamwise velocity distribution

Figure 21.—Velocity Distribution in Distortion Elements

In an attempt to provide a distortion element that is more realistic from the fluid dynamics point of view, a vortex element has been added to the acoustic models. It is used only to represent transverse velocity distortions, and its angular velocity distribution is

$$U_\phi\left(x_1, r, \phi\right) = c_1 \, e^{-\frac{1}{2}\left(\frac{x_1}{\ell}\right)^2} \frac{r}{a} \, e^{-\frac{1}{2}\left[\left(\frac{r}{a}\right)^2 - 1.\right]} \tag{4.3.02}$$

The velocity component u_2 parallel to the x_2 axis (Fig. 21) is therefore

$$V\left(\vec{x}\right) = c_1 \, e^{-\frac{1}{2}\left(\frac{x_1}{\ell}\right)^2} \frac{x_3}{a} \, e^{-\frac{1}{2}\left[\frac{x_2^2 + x_3^2}{a^2} - 1\right]} \tag{4.3.03}$$

The following analysis is based on the vortex element, but the results for the Gaussian eddy are very similar and are summarized at the end of this section.

A vortex element convected along a streamline through point $(0, x_2, x_3)$ will induce a velocity pulse at a point $(0, \xi_2, \xi_3)$

$$V\left(t, \xi_2, \xi_3\right) = c_1 \frac{x_3 - \xi_3}{a} \, e^{-\frac{1}{2}\left(\frac{U \cdot t}{\ell}\right)^2} \, e^{-\frac{1}{2}\left[\frac{\left(x_2 - \xi_2\right)^2 + \left(x_3 - \xi_3\right)^2}{a^2} - 1.\right]} \tag{4.3.04}$$

with

U = mean flow velocity
t = time

This velocity pulse is the same for all points in the (x_2, x_3) plane, except for its amplitude, which is a function of the relative position of streamline (x_2, x_3) and the point (ξ_2, ξ_3). A distribution of vortices convected along the streamline will induce velocity pulses at the origin (0, 0, 0) and at the point $(0, \xi_2, \xi_3)$ (Figure 22). In Reference 36 it is shown that if the vortices are Poisson distributed along the streamline, the correlation function $R_a(\tau, \xi_2, \xi_3)$ is equal to the product of the pulse correlation function $R_p(\tau, \xi_2, \xi_3)$ and the average occurrence rate M.

$$R_a(\tau, \xi_2, \xi_3) = M \cdot R_p(\tau, \xi_2, \xi_3) \tag{4.3.05}$$

$$M = N \cdot U \cdot dx_2 \cdot dx_3 \tag{4.3.06}$$

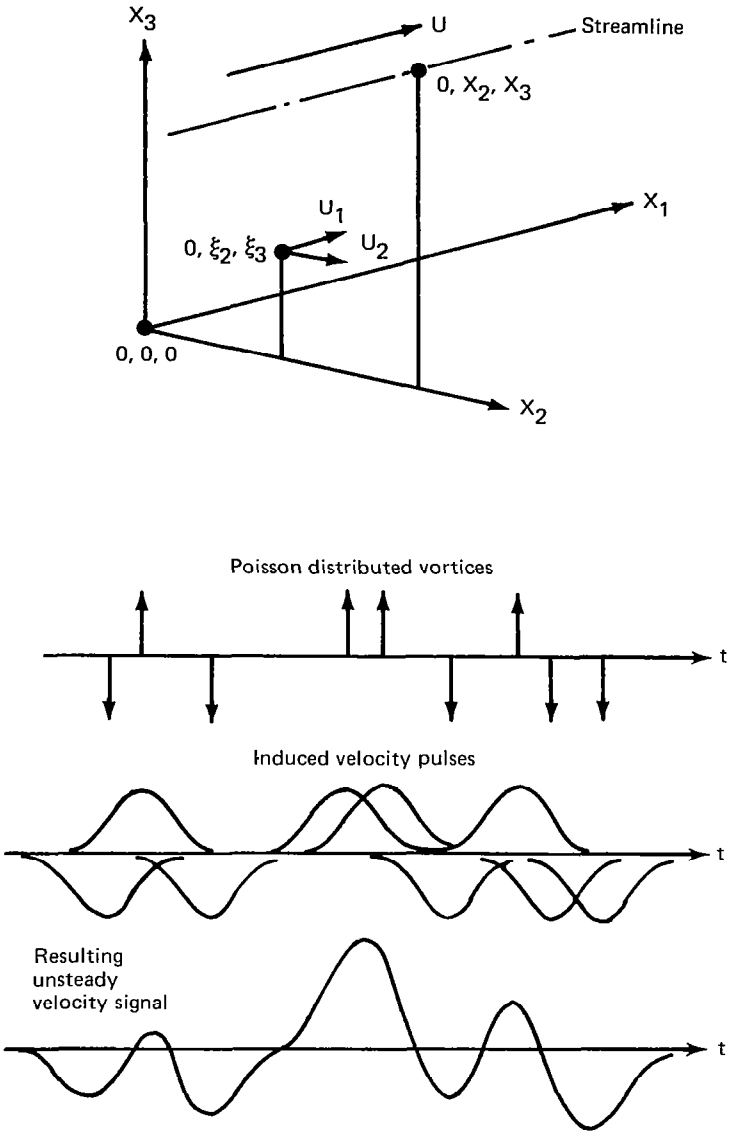

Figure 22.—Unsteady Velocity Due to Vortices of Identical Scales Convected Along a Single Streamline

$$R_p\left(\tau, \xi_2, \xi_3\right) = \sqrt{\pi}\frac{\ell}{U}\, c_1{}^2\, \frac{x_3\left(x_3 - \xi_3\right)}{a}\, e^{-\left(\frac{U\cdot\tau}{2\ell}\right)^2}$$

$$e^{-\frac{1}{2}\left[\frac{x_2{}^2 + x_3{}^2 + \left(x_2 - \xi_2\right)^2 + \left(x_3 - \xi_3\right)^2}{a^2} - 2\right]} \qquad (4.3.07)$$

with N = average number of eddies per volume unit.

In a homogeneous distribution of vortices in unbounded space, Poisson distributed along all streamlines, the three-dimensional correlation function $R_b\,(\tau, \xi_2, \xi_3)$ can be computed by integration of $R_a\,(\tau, \xi_2, \xi_3)$ over x_2 and x_3 and a simple coordinate transform

$$R_b\left(\xi_1, \xi_2, \xi_3\right) = \overline{v^2}\, e^{-\left(\frac{\xi_1}{2\ell}\right)^2} \cdot e^{-\left(\frac{\xi_2}{2a}\right)^2}\left[1 - \frac{1}{2}\left(\frac{\xi_3}{a}\right)^2\right] e^{-\left(\frac{\xi_3}{2a}\right)^2} \qquad (4.3.08$$

$$\overline{v^2} = \frac{e}{2}\,\pi\sqrt{\pi}\, N\, c_1{}^2\, a^2\, \ell \qquad (4.3.09)$$

with $\overline{v^2}$ = variance.

R_b is the correlation function for a distribution of vortices of equal scales a, ℓ and c_1. It is assumed that in an actual turbulence field the random motion is due to a random distribution of vortices of various length and velocity scales. For this reason the scales a, ℓ and c are assumed to be statistically independent random variables, each with its own one-dimensional probability density distribution.

$$P(a),\ P(\ell),\ P(c)$$

Beta probability density distributions are chosen for all three variables to provide flexibility (Figure 23):

$$P(t) = \frac{\Gamma\left(m_a + n_a + 2\right)}{\Gamma\left(m_a + 1\right)\,\Gamma\left(n_a + 1\right)}\, t^{m_a}\,(1 - t)^{n_a} \qquad (4.3.10)$$

with

t = normalized independent variable (a/a_{max})

Γ = gamma function.

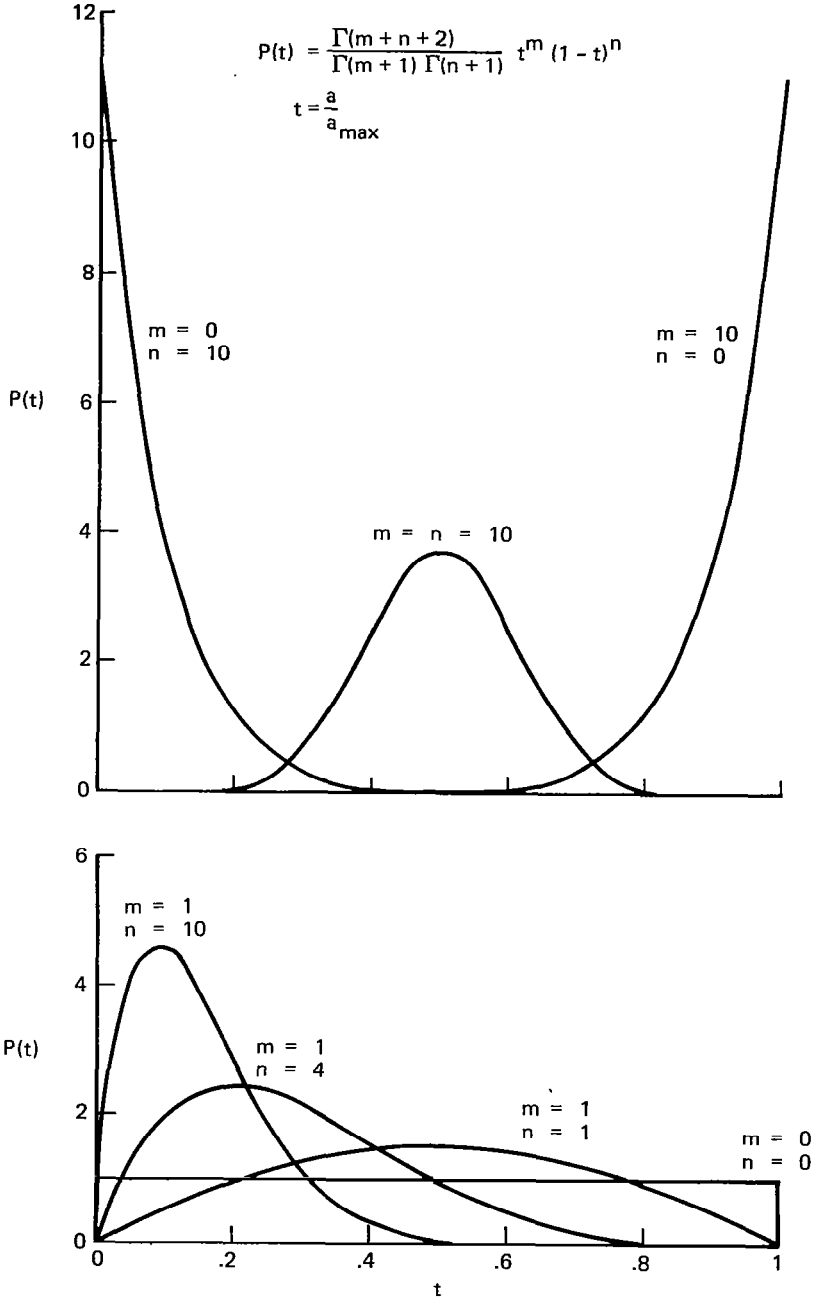

Figure 23.—Beta Probability Density Distribution

To further enhance the flexibility of the model, the following deterministic relationship between velocity and length scales has been assumed.

$$c_1^2 = c^2 \left(\frac{a}{a_{max}}\right)^{-\alpha} \left(\frac{\ell}{\ell_{max}}\right)^{-\beta} \tag{4.3.11}$$

In a random distribution of vortices, the density of vortices with a given set of scales is

$$N \cdot P(a) \cdot P(\ell) \cdot P(c)\, da\, d\ell\, dc \tag{4.3.12}$$

The contribution of vortices of these scales to the correlation function is

$$R_c(\vec{\xi}) = R_b(\vec{\xi}) \cdot P(a) \cdot P(\ell) \cdot P(c)\, da\, d\ell\, dc \tag{4.3.13}$$

The correlation function for a random vortex field is found by integration over the random variables.

$$R_V(\vec{\xi}) = \frac{\overline{V^2}}{\left(\frac{\ell}{\ell_{max}}\right)^{1-\beta} \overline{\left(\frac{a}{a_{max}}\right)^{2-\alpha}}} \int_0^{\ell_{max}} \left(\frac{\ell}{\ell_{max}}\right)^{1-\beta} P(\ell)\, e^{-\left(\frac{\xi_1}{2\ell}\right)^2} d\ell$$

$$\int_0^{a_{max}} \left(\frac{a}{a_{max}}\right)^{2-\alpha} P(a)\, e^{-\left(\frac{\xi_2}{2a}\right)^2} \left[1 - \frac{1}{2}\left(\frac{\xi_3}{a}\right)^2\right] e^{-\left(\frac{\xi_3}{2a}\right)^2} da \tag{4.3.14}$$

with

$$\overline{V^2} = \frac{e}{4} \sqrt{\pi}\, N\, \overline{c^2} \cdot E \overline{\left(\frac{\ell}{\ell_{max}}\right)^{1-\beta}} \overline{\left(\frac{a}{a_{max}}\right)^{2-\alpha}} \tag{4.3.15}$$

$$E = 2\pi\, \ell_{max}\, a_{max}^2 \tag{4.3.16}$$

subscript V stands for vortex.

The turbulence variance is therefore proportional to the product of the mean square maximum velocity $\overline{c^2}$ of the largest vortices, the vortex density N and the volume E of the largest vortices.

The corresponding one-dimensional correlation coefficients are found by setting two components of the separation vector ($\vec{\xi}$) to zero and normalizing with the variance $\overline{v^2}$.

$$C_v\left(\frac{\xi_1}{L_1}, 0., 0.\right) = \frac{\Gamma\left(m_\ell + n_\ell + 3 - \beta\right)}{\Gamma\left(m_\ell + 2 - \beta\right)\Gamma\left(n_\ell + 1\right)} \int_0^1 t^{m_\ell + 1 - \beta} (1 - t)^{n_\ell}$$

$$e^{-\left(\frac{\xi_1}{L_1}\frac{L_1}{2\ell_{max}}\frac{1}{t}\right)^2} dt \qquad (4.3.17)$$

$$C_v\left(.0, \frac{\xi_2}{L_2}, .0\right) = \frac{\Gamma\left(m_a + n_a + 4 - \alpha\right)}{\Gamma\left(m_a + 3 - \alpha\right)\Gamma\left(n_a + 1\right)} \int_0^1 t^{m_a + 2 - \alpha} (1 - t)^{n_a}$$

$$e^{-\left(\frac{\xi_2}{L_2}\frac{L_2}{2\,a_{max}}\frac{1}{t}\right)^2} dt \qquad (4.3.18)$$

$$C_v\left(0, 0, \frac{\xi_3}{L_2}\right) = \frac{\Gamma\left(m_a + n_a + 4 - \alpha\right)}{\Gamma\left(m_a + 3 - \alpha\right)\Gamma\left(n_a + 1\right)} \int_0^1 t^{m_a + 2 - \alpha} (1 - t)^{n_a}$$

$$\left[1 - \frac{1}{2}\left(\frac{\xi_3}{2\,a_{max}\,t}\right)^2\right] e^{-\left(\frac{\xi_3}{2\,a_{max}\,t}\right)^2} dt \qquad (4.3.19)$$

where L_1 and L_2 are the corresponding integral length scales.

$$L_1 = \sqrt{\pi}\ \ell_{max}\ \frac{m_\ell + 2 - \beta}{m_\ell + n_\ell + 3 - \beta} \tag{4.3.20}$$

$$L_2 = \sqrt{\pi}\ a_{max}\ \frac{m_a + 3 - \alpha}{m_a + n_a + 4 - \alpha} \tag{4.3.21}$$

m and n are the exponents in the Beta probability density distributions for the length scales a and ℓ, while a_{max} and ℓ_{max} are the upper bounds on the distributions of these variables.

The normalized, one-sided, one-dimensional spectra are determined by Fourier transformation of the corresponding correlation coefficients.

$$\frac{F_v(k_1)}{L_1 \overline{v^2}} = \frac{2\,\Gamma(m_\ell + n_\ell + 4 - \beta)}{\pi\,\Gamma(m_\ell + 3 - \beta)\,\Gamma(n_\ell + 1)} \int_0^1 t^{m_\ell + 2 - \beta} (1-t)^{n_\ell} \, e^{-\left(k_1 L_1 \frac{\ell_{max}}{L_1} \frac{1}{t}\right)^2} dt \tag{4.3.22}$$

$$\frac{F_v(k_2)}{L_2 \overline{v^2}} = \frac{2\,\Gamma(m_a + n_a + 5 - \alpha)}{\pi\,\Gamma(m_a + 4 - \alpha)\,\Gamma(n_a + 1)} \int_0^1 t^{m_a + 3 - \alpha} (1-t)^{n_a} \, e^{-\left(k_2 L_2 \frac{a_{max}}{L_2} \frac{1}{t}\right)^2} dt \tag{4.3.23}$$

$$\frac{F_v\left(k_3\right)}{L_2\,\overline{v^2}} = \frac{4\,\Gamma\left(m_a + n_a + 5 - \alpha\right)}{\pi\,\Gamma\left(m_a + 4 - \alpha\right)\,\Gamma\left(n_a + 1\right)} \left(k_3\,L_2\,\frac{a_{max}}{L_2}\right)^2 \int_0^1 t^{m_a + 3 - \alpha} (1 - t)^{n_a}$$

$$e^{-\left(k_3\,L_2\,\frac{a_{max}}{L_2}\,\frac{1}{t}\right)^2} dt \qquad (4.2.24)$$

Most of these equations are also valid for a random distribution of Gaussian eddies. But the velocity distribution in the Gaussian eddy is axisymmetric and therefore the one-dimensional correlation functions for the x_2 and x_3 components of the separation vector must be the same.

The statistical averages for the random Gaussian eddy distribution are

Variance $$\overline{v_E^2} = \pi\sqrt{\pi}\,N\,\bar{c}^2\,a_{max}^2\,\ell_{max}\,\overline{\left(\frac{a}{a_{max}}\right)^{2-\alpha}}\;\overline{\left(\frac{\ell}{\ell_{max}}\right)^{1-\beta}} \qquad (4.3.25)$$

Integral length scales

$$L_{E1} = L_{V1} = L_1$$

$$L_{E2} = L_{E3} = L_{V2} = L_2$$

Correlation coefficients

$$C_E\left(\frac{\xi_1}{L_1}\right) = C_V\left(\frac{\xi_1}{L_1}\right)$$

$$C_E\left(\frac{\xi_2}{L_2}\right) = C_E\left(\frac{\xi_3}{L_2}\right) = C_V\left(\frac{\xi_2}{L_2}\right)$$

Spectra

$$\frac{F_E\left(k_1\right)}{L_1\,\overline{v^2}} = \frac{F_V\left(k_1\right)}{L_1\,\overline{v^2}}$$

$$\frac{F_E\left(k_2\right)}{L_2\,\overline{v^2}} = \frac{F_E\left(k_3\right)}{L_2\,\overline{v^2}} = \frac{F_V\left(k_2\right)}{L_2\,\overline{v^2}}$$

4.3.3 RESULTS

Equations (4.3.15) through (4.3.25) have been programmed. The integrals in the equations for the correlation coefficients and the spectra are solved by numerical methods. A limited parametric study has been conducted to determine the effects of the probability density distributions on the correlations and spectra and to find the appropriate distributions to represent the turbulence at the fan face.

Turbulence Variance

Equations (4.3.15) and 4.3.25) indicate that for given scale distributions P(a) and P(ℓ) the turbulence variance is proportional to:

N = density of eddies or vortices (number of eddies per unit volume)

$\overline{c^2}$ = mean squared maximum velocity of the largest eddies

E = volume of the largest eddies.

The volume E is of course related to the integral scales of the turbulence. The product $N\overline{c^2}$ appears only in the equation for the turbulence variance and the two variables cannot be separated.

For the same set of parameters N, $\overline{c^2}$ and E and the same scale distributions the variance of a vortex field is larger by a factor of e/2 than the one of a Gaussian eddy field.

Integral Length Scales

The integral scales in a vortex field are the same as in a Gaussian eddy field, except for the transverse scale normal to the turbulence velocity component. The latter is equal to zero in a vortex field, whereas both transverse integral scales are the same in a Gaussian eddy field. The ratio between the integral and the maximum scale tends towards one for large values of m and towards zero for large values of n, with m and n the exponents in the probability density function.

Spectra and Correlations

Correlation coefficients and one-dimensional spectra for a field of identical vortices (a single scale vortex field) are shown in Figures 24 and 25. They do not compare well with the corresponding results presented in Section 4.2.3. The correlation coefficients are too wide at the apex and the spectra fall off too rapidly at large wavenumbers. Both discrepancies result from a lack of high wavenumber, small scale turbulence energy.

Turbulence spectra that represent scale distributions rather than single scales are shown in Figures 26 through 31. They are based on equations (4.3.17) through (4.3.24). The parameters that control the shape of the spectra and correlations are the exponents m_ℓ, n_ℓ and β for the streamwise correlation and the corresponding spectrum and m_a, n_a and α for the transverse correlations and the corresponding spectra.

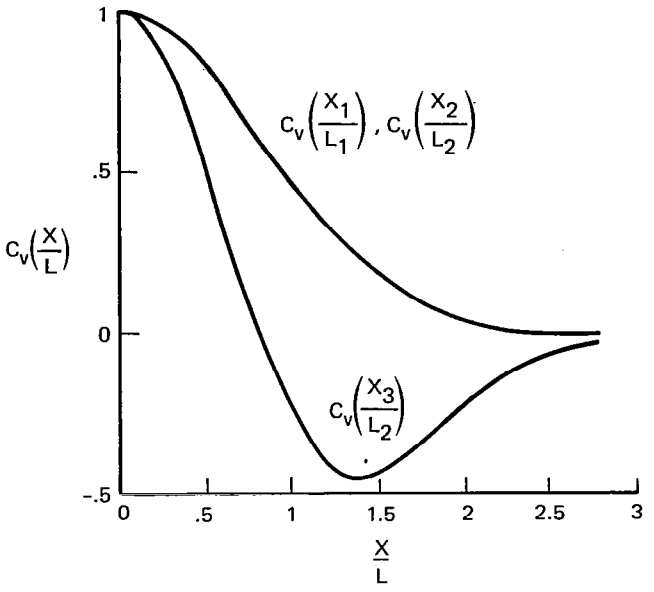

Figure 24.—Correlation Coefficients in a Single Scale Vortex Field

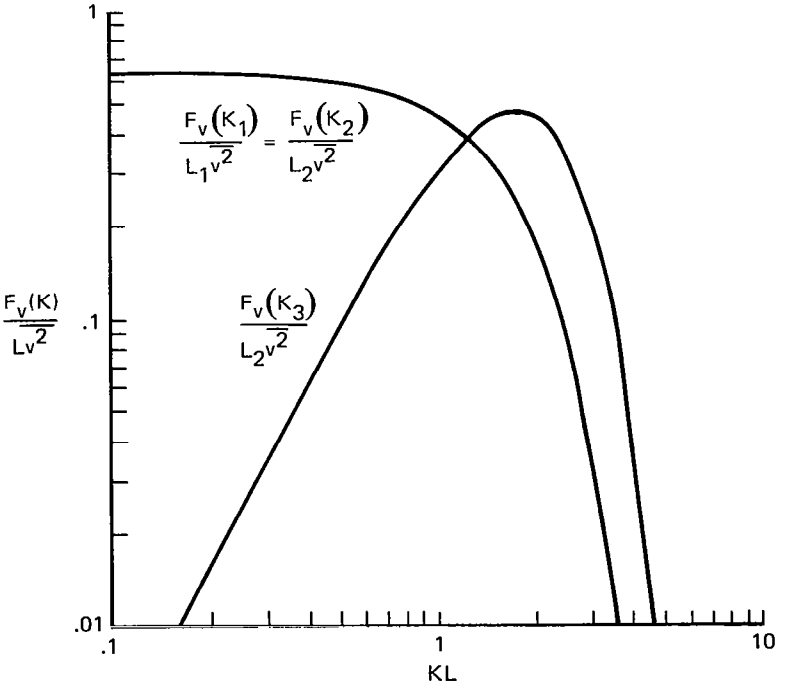

Figure 25.—Normalized Spectra in a Single Scale Vortex Field

The exponents m_ℓ and β, as well as m_a and α appear only in the form of the differences $m_a - \alpha$ and $m_\ell - \beta$ in the equations for the spectra and correlations. The number of shape factors for each spectrum is therefore reduced to two.

Spectra based on such scale distributions form an exponential relationship at large wave numbers. The exponent of this relationship is a function of the difference $(m_\ell - \beta)$ or $(m_a - \alpha)$, see Figure 26. In actual turbulence spectra this exponential relationship represents the inertial subrange. In the von Karman spectra the exponent assumes a value of (-5/3), whereas in the spectra of Section 4.2 it is (-2). In order to simulate spectra with such small negative exponents, based on scale distributions with finite probability densities, it was necessary to introduce the exponents α and β. The proper representation of the inertial subrange is important and the exponents $(m_a - \alpha)$ and $(m_\ell - \beta)$ are selected accordingly.

The effect of the exponents n_a and n_ℓ on the spectra is shown in Figure 27. The variation of n is restricted by numerical limits, the values -.5 and 50. are close to the actual limits. The results indicate that even with the flexibility of the Beta probability density function, the spectra and correlations are strongly dominated by the corresponding functions of the single element.

The normalized spectra and correlations for the vortex and the Gaussian eddy field are the same except for the ones in the direction normal to the mean flow and the turbulence velocity. For the Gaussian eddy field, the two transverse correlations and the corresponding spectra are the same due to its symmetry.

Representation of the Turbulence at the Fan Face

Based on the comparison of the spectra of this section with those of Section 4.2, it appears that in general the post-contraction turbulence field cannot be represented by simple Gaussian eddy and vortex distributions. However, in the evaluation of fan tone noise due to atmospheric turbulence, there are only two conditions of primary interest, static (ground test) and approach flight. The static condition is characterized by its large contraction ratios. The turbulence field at the fan face is dominated by the transverse turbulence component and can be well represented by a vortex field. The turbulence field associated with the streamwise component can be neglected. The approach flight condition is characterized by its small contraction ratios (between 1. and 2.). In Section 5.3 it is shown that in such situations the tone noise generation is dominated by the streamwise turbulence component. In this condition the turbulence at the fan face can be well represented by a distribution of Gaussian eddies.

The results of Section 4.2 indicate that the exponential relationship at large wavenumbers is the same for the pre- and post-contraction spectra. In the large scale turbulence the exponent is (-5/3), representative for an inertial subrange. The same exponent has been selected for the representation of the turbulence at the fan face and the exponents m_a, m_ℓ, α and β assume the following values

$$m_a = m_\ell = .0 \quad \alpha = \frac{7}{3} \quad \beta = \frac{4}{3}$$

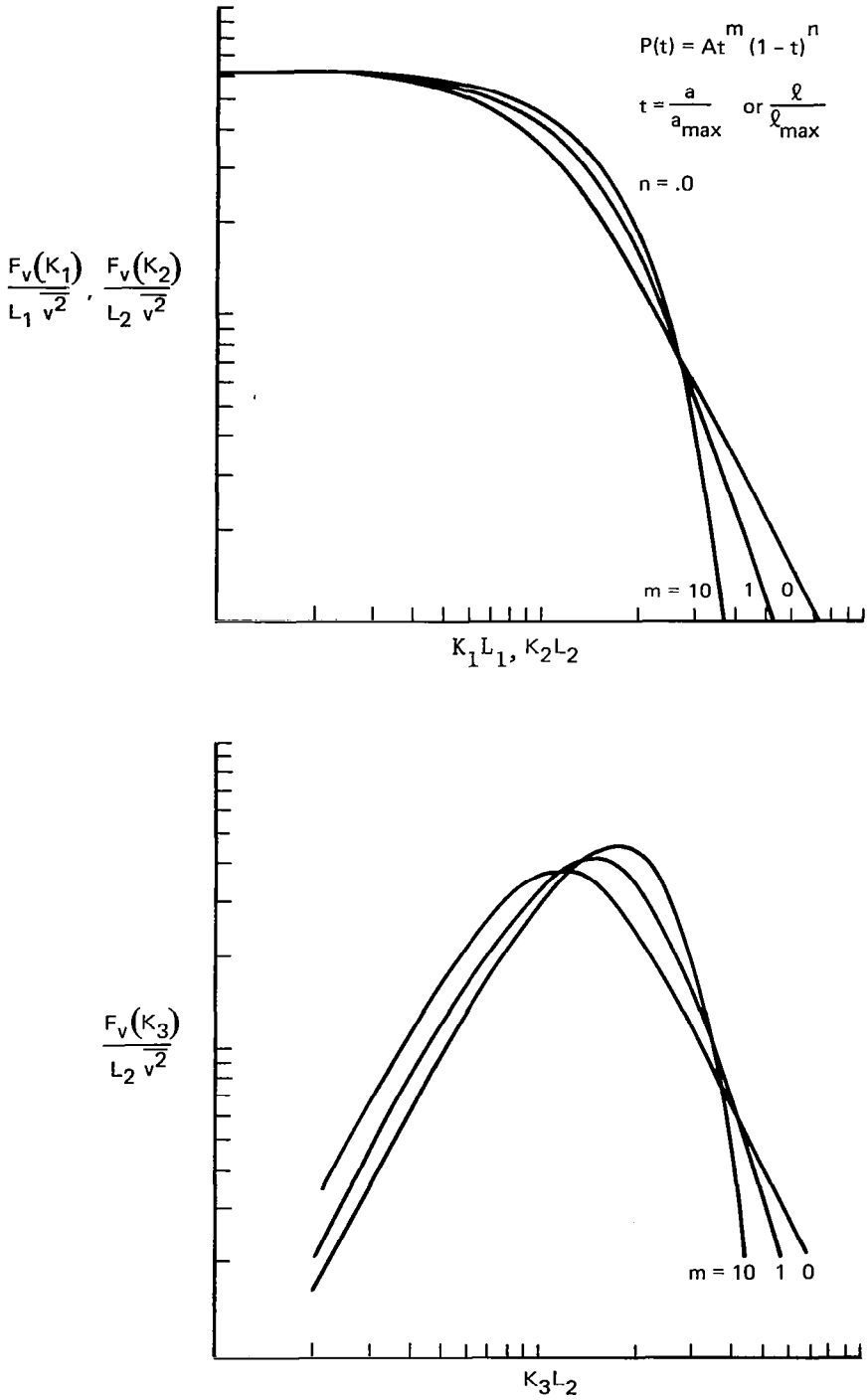

Figure 26.—Normalized Spectra in Vortex Field for Various Exponents m in the Probability Density Distribution P(t)

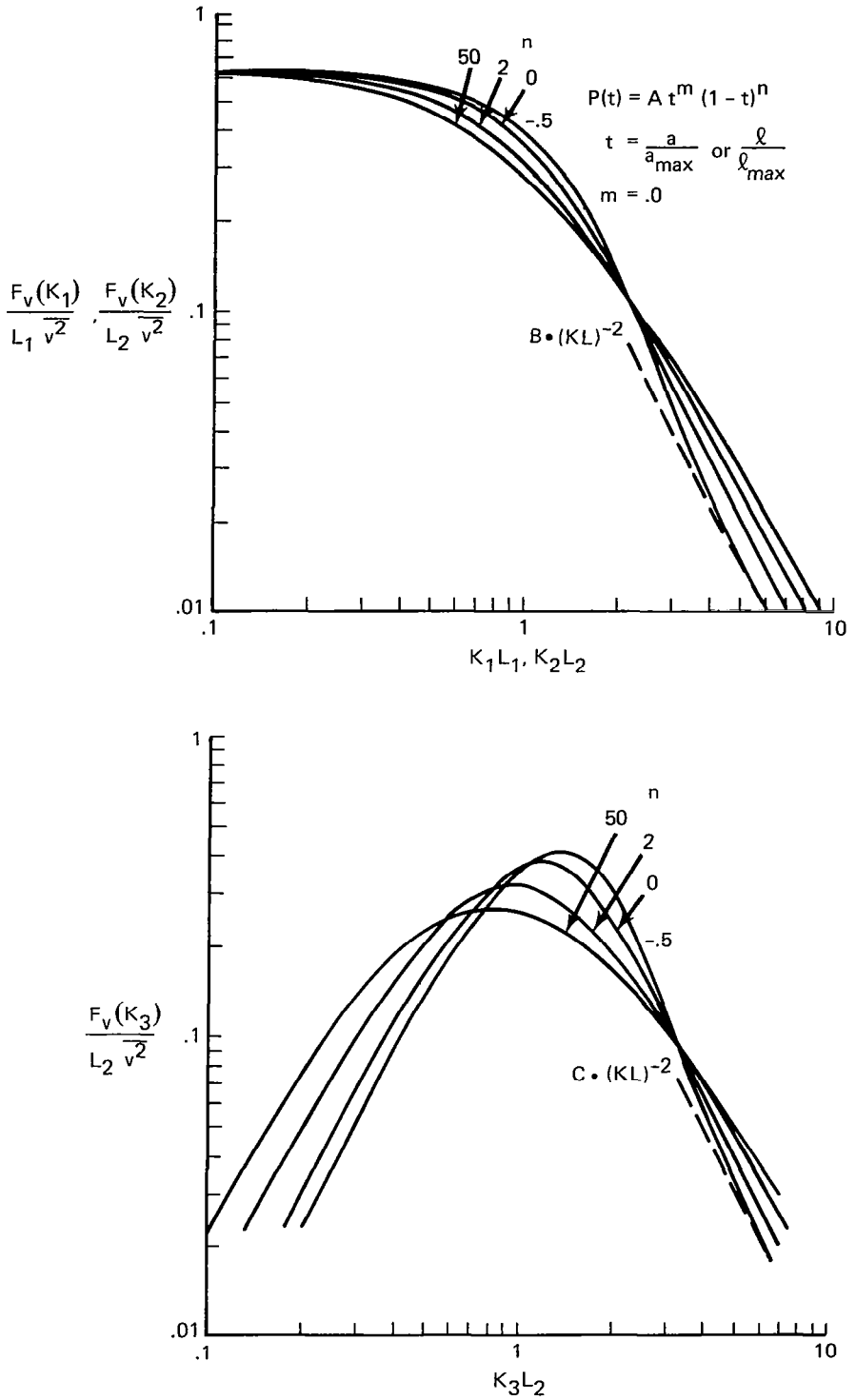

Figure 27.—Normalized Spectra in Vortex Field for Various Exponents n in the Probability Density Distribution P(t)

The exponents n_a and n_ℓ have only a minor effect on the spectra and are assumed to be zero

$$n_a = n_\ell = .0$$

The normalized spectra for a Gaussian eddy field are compared with the von Karman spectra in Figure 28. They show reasonably good agreement. The normalized spectra of the vortex field based on the selected exponents are compared with the corresponding post-contraction spectra in Figure 29. Again the agreement is quite close.

The contributions of various segments of the scale distribution to a spectrum is shown in Figure 30. This result demonstrates that in this particular representation of the turbulence the various segments of the spectrum are dominated by certain ranges of scales. The effect of the elimination of the largest scales within a distribution on the spectra is shown in Figure 31. For the assumed scale distribution (m = n = .0) the shape of the normalized spectrum does not change, only the integral scale and the turbulence variance are affected. This feature of the model is used in the evaluation of the atmospheric turbulence in flight conditions, where only a limited segment of the total range of scales is of interest.

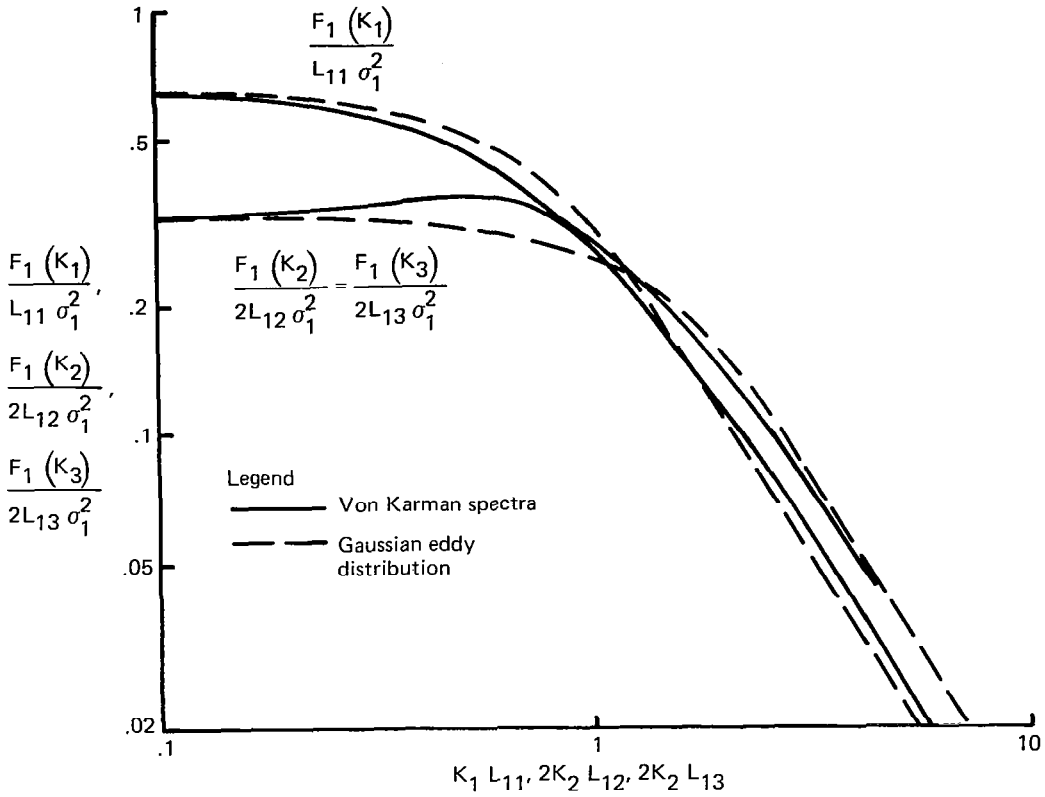

Figure 28.—Comparison of Spectra Based on Von Karman Formulas and Gaussian Eddy Distribution

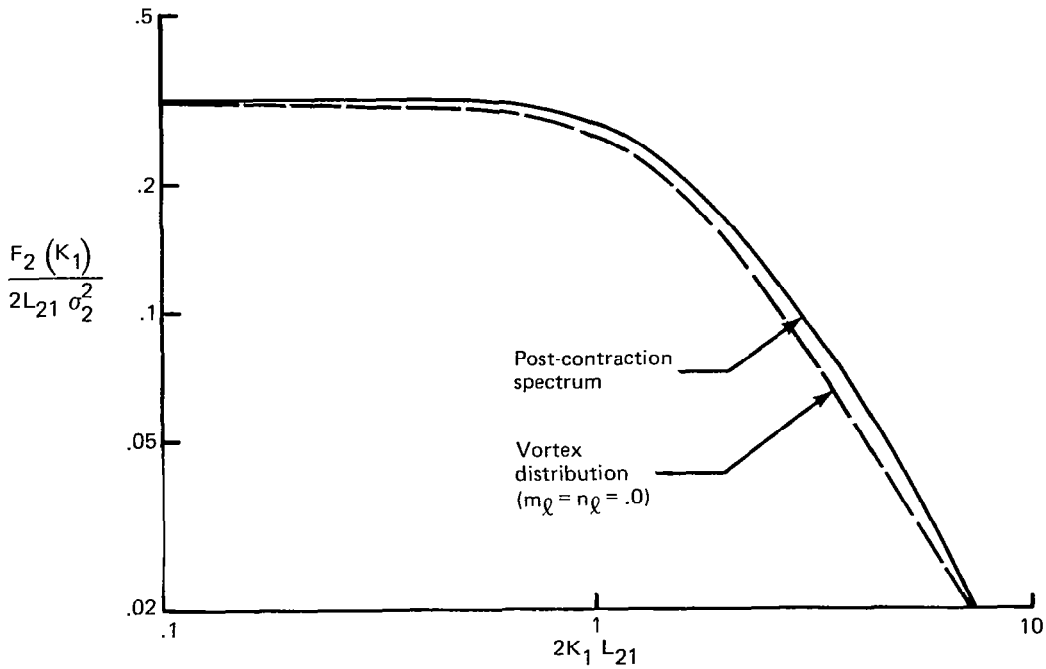

Figure 29.—Comparison of Spectra Based on Contraction Model and Vortex Distribution

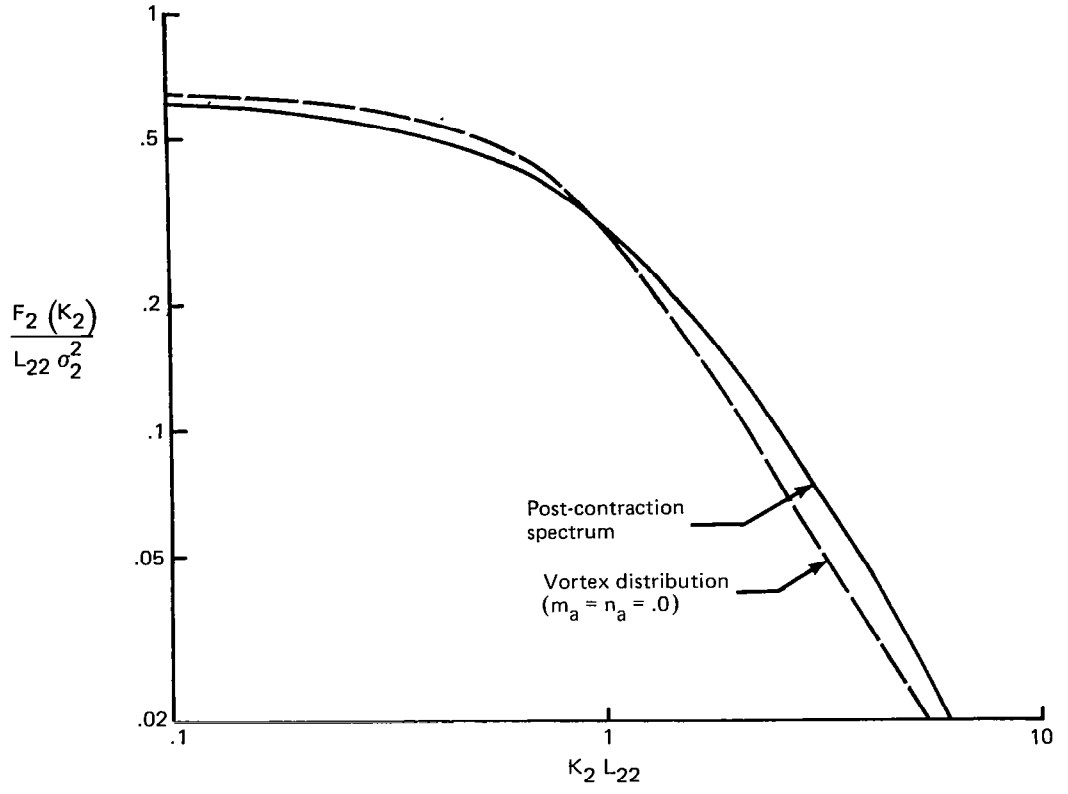

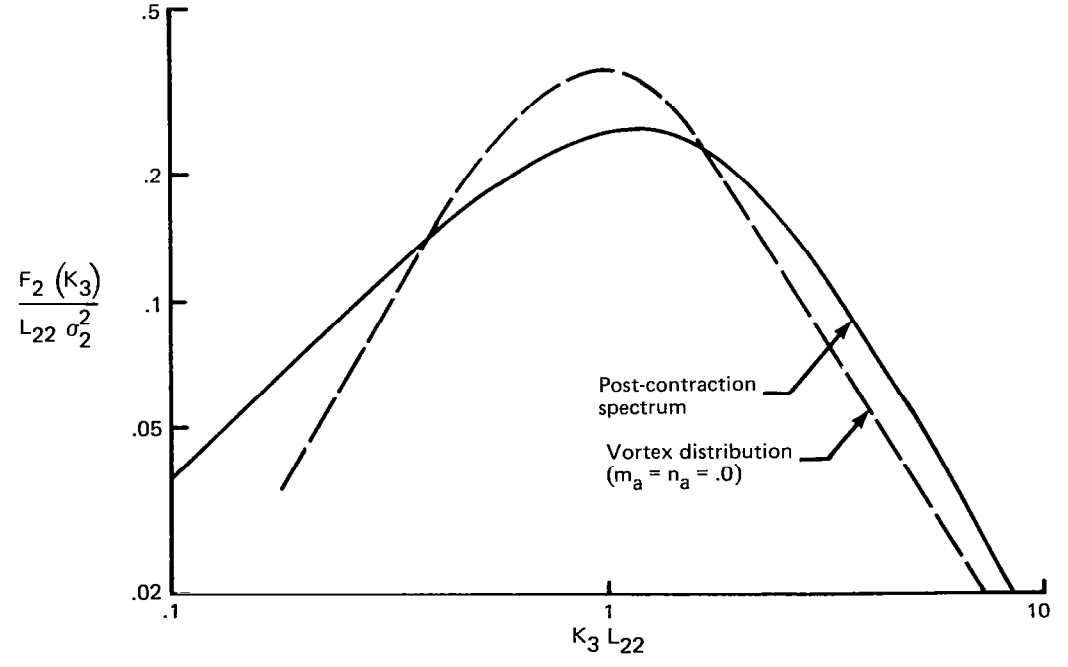

Figure 29 (Concluded)

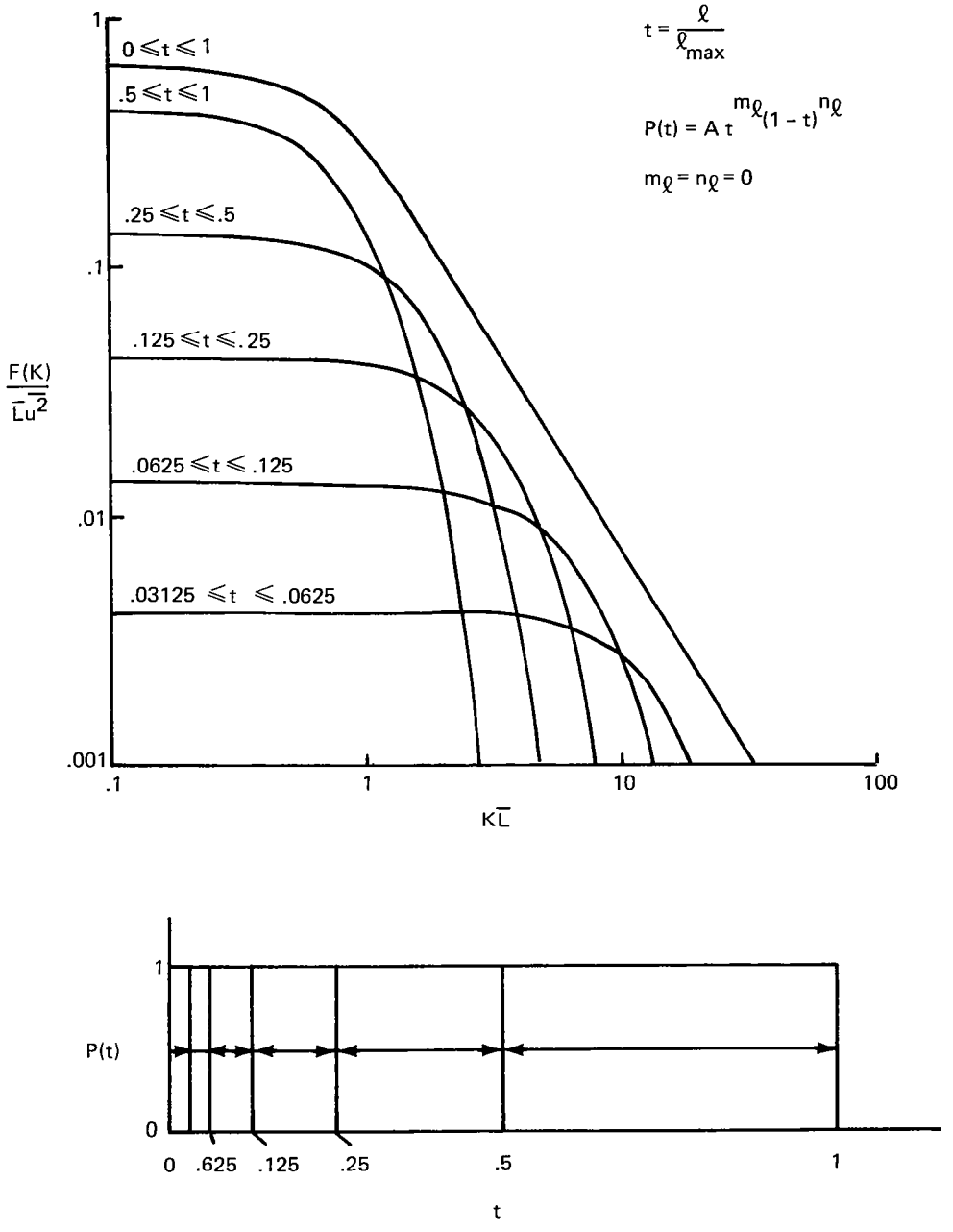

Figure 30.—Contribution of Various Scale Ranges to the Overall Turbulence Spectrum

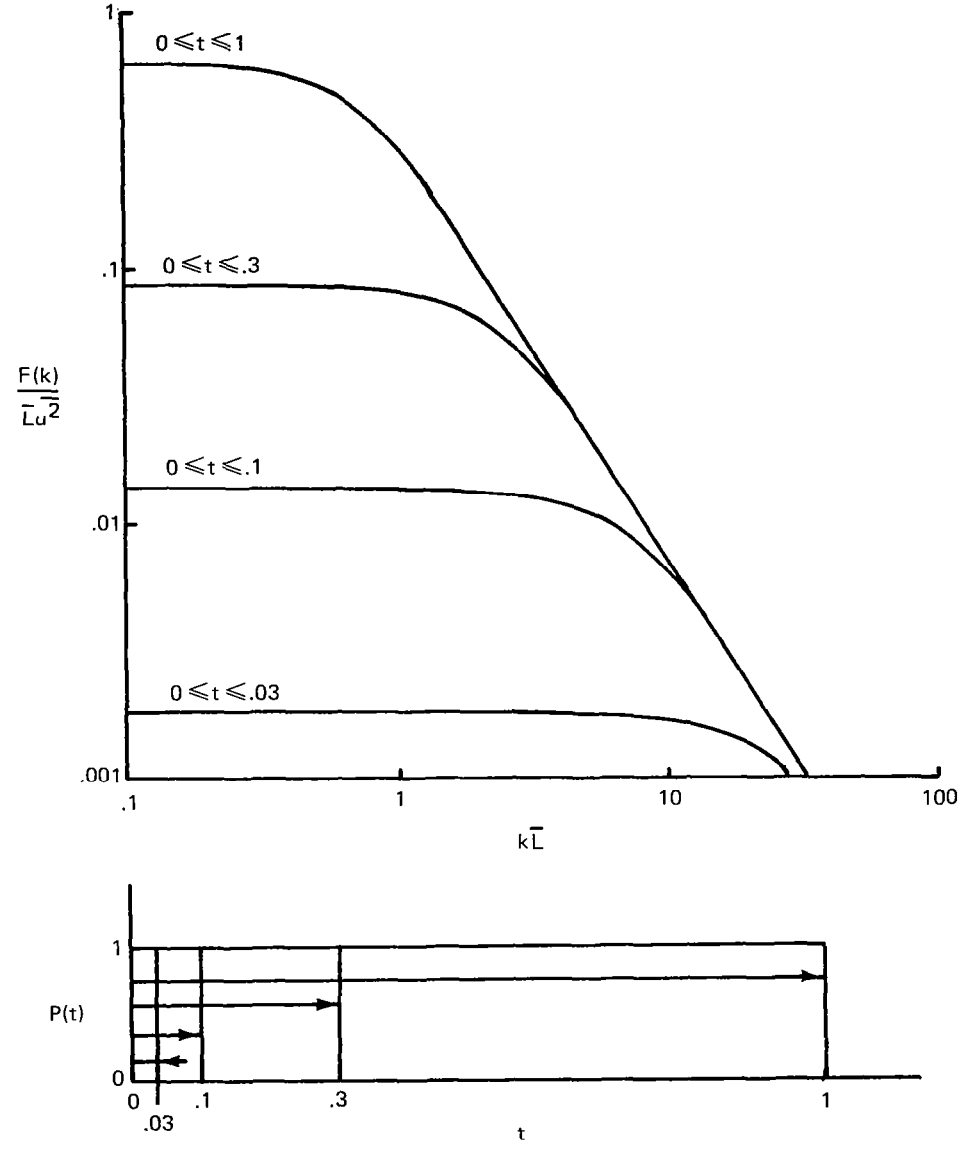

Figure 31.—Effect of Upper Limit of Scale Range on Turbulence Spectra

5.0 ROTOR TONE NOISE STUDIES

This section describes the analytical evaluation of fan tone noise resulting from atmospheric turbulence in the fan inflow field. The investigation is based on analytical fan noise models developed by T. L. Clark at The Boeing Company. The investigation is divided into 3 segments. In Section 5.1 tone noise resulting from single distortion elements is evaluated to determine the range of scales that cause significant tone noise levels. In Section 5.2 a parametric study of rotor tone noise due to convected turbulence is presented. The turbulence is based on predicted spectral distributions and is represented by a homogeneous distribution of distortion elements. In Section 5.3, the difference in rotor tone noise due to atmospheric turbulence between static and flight conditions is estimated based on the models and the results described in the preceding sections.

5.1 ROTOR TONE NOISE DUE TO UNSTEADY DISTORTION

5.1.1 REVIEW OF ANALYSIS

This investigation is based on the analysis of Reference 33. The acoustic models described in that reference compute the sound pressure field at the harmonics of the blade passing frequency, radiated from a fan stage into an infinite, hardwalled annulus. The duct pressure field is described in the form of an eigenfunction expansion.

$$P(\rho, \phi, z, t) = \frac{\rho_o c_o^2}{(2\pi)^2} \sum_{k=-\infty}^{\infty} \sum_{m=-\infty}^{\infty} \sum_{n=0}^{\infty} A_{mnk}^{\pm} \Re_m \left(\mu_{mn} \rho\right) e^{i\left(m\phi + k_{mn}^{\pm} z - \omega_o kt\right)} \qquad (5.1.01)$$

with

ρ, ϕ, z = duct coordinates
ρ_o = air density
c_o = speed of sound
k = harmonic index
m = spinning order
n = radial order
k_{mn} = axial wavenumber
ω_o = blade passing frequency
$A_{mn\,k}$ = non-dimensional mode amplitude
$\Re_m\left(\mu_{mn}\rho\right)$ = normalized radial eigenfunction
μ_{mn} = annular duct eigenvalue

The analysis is based on the linearized theory of compressible fluids. Its applicability is therefore restricted to subsonic relative flow velocities.

The noise generating mechanism considered in these models is the unsteady pressure force exerted by blade elements of the fan stage on the fluid. Such forces result from distortions in the mean flow field, which appear as unsteady velocity disturbances to the fan blades. The unsteady pressure distribution on the fan rotor blades is computed with the response function described by Naumann and Yeh (Ref. 37). Since this is a two-dimensional single airfoil response function, its validity is restricted to fan rotors of low solidity. The expansion coefficients, the mode amplitudes, are determined from the unsteady pressure distributions on the blades of the fan stage.

The acoustic model used in the present study is the unsteady distortion or single eddy model. It computes the mode amplitudes resulting from a distortion element convected through a fan rotor. The considered elements are the same as in Section 4.3, the vortex and the Gaussian eddy. In the fan rotor plane, these distortion elements appear as distortions of modulated amplitude. The vortex distortion assumes the following form in the polar coordinates of the rotor plane.

$$V(\rho, \phi, t) = \frac{c_1 \sqrt{e}}{a} e^{-\frac{1}{2}\left(\frac{\rho^2 + R^2}{a^2}\right)} \left[\rho - R\cos(\Phi - \phi)\right] e^{\frac{R\rho}{a^2}\cos(\Phi - \phi)} e^{-\frac{1}{2}\left(\frac{Mt - z}{\ell}\right)^2} \qquad (5.1.02)$$

with

V = angular velocity component

R, Φ, z = coordinates of vortex center at $t = 0$

a, ℓ = radial and axial vortex length scales

c_1 = vortex velocity scale

A similar equation describes the disturbance velocity field of the Gaussian eddy.

After Fourier decomposition of its angular terms and Fourier transform of its time dependent term, equation (5.1.02) becomes

$$V(\rho, \phi, t) = \frac{1}{2\pi} \sum_{\ell^* = -\infty}^{\infty} c_1 \sqrt{e}\; e^{-\frac{\rho^2 + R^2}{2a^2}} \left\{ \frac{\rho}{a} \left[1 - \ell^* \left(\frac{a}{\rho} \right)^2 \right] I_{\ell^*} \left(\frac{R\rho}{a^2} \right) - \left(\frac{R}{a} \right) I_{\ell^* + 1} \left(\frac{R\rho}{a^2} \right) \right\}$$

$$\cdot \frac{1}{\sqrt{2\pi}} \cdot \frac{\ell}{M} e^{i\ell^*(\phi - \Phi)} \int_{-\infty}^{\infty} e^{-\frac{1}{2}\left(\frac{\omega\ell}{M}\right)^2} e^{-i\omega\left(t - \frac{z}{M}\right)}\, d\omega \qquad (5.1.03)$$

with

ℓ^* = harmonic distortion order

ω = distortion modulation frequency

I_{ℓ^*} = modified Bessel function of first kind and order ℓ^*

The ℓ^{*th} harmonic of the disturbance velocity field is therefore composed of an infinite number of components, rotating at different angular velocities ω/ℓ^*

$$V_{\ell^*}(\rho, \phi, t) = F_{1\ell^*}(\rho) \int_{-\infty}^{\infty} F_2(\omega)\, e^{i(\ell^*\phi - \omega t)}\, \partial\omega \qquad (5.1.04)$$

A fan rotor cutting through such a rotating distortion pattern creates a sound pressure field at frequencies separated by the modulation frequency from the blade passing frequency. The amplitude modulated velocity distortion in the plane of a rotating fan, representing a convected distortion element, therefore results in a sound pressure field in frequency bands centered around the blade passing frequencies. The modulation spectrum appears in the sidebands of these center frequencies. The equations for the mode amplitudes representing such a sound pressure field have been derived in Reference 33.

$$|A_{mnk}(\omega_o\, k)| = \frac{N}{4\sqrt{(\omega_o\, k)^2 - (1 - M)^2\, \mu_{mn}{}^2}} \cdot \int_{\eta}^{1} \left(\frac{m}{\rho} \cos\gamma + k_{mn}^{\pm} \sin\gamma \right)$$

$$\mathcal{R}_m \left(\mu_{mn}\, \rho \right) \sum_{k = -\infty}^{\infty} \partial \left(\omega_o\, k - KNM_t \right)$$

$$C_h \frac{\partial C_L}{\partial \alpha} M_M V_{\ell^*} \cos\gamma \, E^* | G_{mn\ell^*} | d\rho$$

with

$$V_{\ell^*} = 2\pi c_1 \sqrt{e}\, e^{-\left(\frac{\rho^2 + R^2}{2a^2}\right)} \left\{ \frac{\rho}{a} \left[1 - \ell^* \left(\frac{a}{\rho}\right)^2 \right] I_{\ell^*} \left(\frac{R\rho}{a^2}\right) - \frac{R}{a} I_{\ell^*+1} \left(\frac{R\rho}{a^2}\right) \right\} \quad (5.1.06)$$

$$E^* = \frac{1}{\sqrt{2\pi}} \frac{\ell}{M} \int_{-B}^{B} e^{-\frac{1}{2}\left(\omega \frac{\ell}{M}\right)^2} \cos\left(\omega \frac{z}{M}\right) d\omega \quad (5.1.07)$$

$$\ell^* = m - kN \quad (5.1.08)$$

N = number of rotor blades
η = hub to tip ratio
c_h = rotor blade chord
$\partial c_L/\partial\alpha$ = derivative of blade lift coefficient
M_M = blade relative Mach number
M_t = blade tip Mach number
γ = stagger angle
B = half bandwidth

In the derivation of the equation for the mode amplitude, it has been assumed that only the sound pressure field within a small frequency band is considered. This band is centered around the blade passing frequency or its harmonics and its width (2B) is assumed to be small in comparison with the blade passing frequency. It further has been assumed that all the modes of order m and n at frequencies within the band can be integrated into a single mode with amplitude $|A_{mnk}|$ at the center frequency. The phase relationship between the modes that contribute to this narrowband mode varies with time and due to this the amplitude of the resulting mode varies with time.

Equation (5.1.05) defines the mode amplitude resulting from a single vortex convected through a fan rotor. The corresponding equation for a Gaussian eddy is very similar and is shown in Reference 33.

The integrals in equation (5.1.05) are solved by numerical methods. The results are presented in the form of in-duct power levels W. The latter is determined by integration of the local, axial acoustic energy flux I_z and is based on the following equation.

$$W_k = \int_0^{2\pi} \int_\eta^1 I_z \rho d\rho \, d\phi = \frac{R_o^2 \rho_o c_o^3}{(2\pi)^2} \sum_{m=-\infty}^{\infty} \sum_{n=0}^{\infty} \frac{1}{\pi}$$

$$\left(1 - M^2\right)^2 \frac{\sqrt{1 - \left(1 - M^2\right)\left(\frac{\mu_{mn}}{k\omega_o}\right)^2}}{\left[1 \mp M\sqrt{1 - \left(1 - M^2\right)\left(\frac{\mu_{mn}}{k\omega_o}\right)^2}\right]^2} |A_{mnk}|^2 \qquad (5.1.09)$$

with R_o the outer annulus radius.

In the summation over the spinning and radial orders m and n the cutoff criteria is used to select the propagating modes. They satisfy the well known condition

$$\mu_{mn} \leqslant \frac{\omega_o k}{\sqrt{1 - M^2}} \qquad (5.1.10)$$

5.1.2 RESULTS

A parametric study of rotor tone noise due to convected distortion elements has been conducted using the model described in the preceding section. The purpose of this study is to determine the transverse length scales of distortion elements, eddies or vortices, that cause significant tone noise levels. The rotor geometry represents a typical single stage, high bypass ratio fan (JT9D, CF6, RB.211) with

hub to tip ratio	η = .38
rotor solidity	= 1.55

The rotor blades are represented as twisted flat plates. The chord lines are aligned with the local mean flow velocity at the leading edge.

relative mean flow angle (deg)	tip	20
	hub	43

The fan operating conditions cover the approach power range (high subsonic tip speed). The ranges of the parameters investigated in this study and the base case, the reference case are summarized in the following table.

Parameter	Range	Base case
Number of rotor blades	12 46	23
Mechanical tip Mach number	.7 .9	.876
Relative tip Mach number	.745 .958	.930
Transverse eddy scale (duct radii)	.01 1.0	.1
Streamwise eddy scale (duct radii)	10.	10.
Radial location of eddy center (duct radii)	.9	.9
Distortion velocity components	streamwise, transverse angular	transverse angular
Distortion elements	vortex, Gaussian eddy	Gaussian eddy

Radial locations of the distortion centers other than the 90% of the inlet radius have been evaluated during this study. But the results indicated that the sound pressure field due to distortions in the fan tip region is significantly higher than the one resulting from distortions at other radii. The results presented in Section 5.1 of this study are therefore limited to distortions at this particular radial location. The studies described in Sections 5.2 and 5.3 are concerned with rotor tone noise due to convected homogeneous turbulence and are therefore concerned with distortions at all radial locations within the inlet. The parametric study was limited to the blade passing frequency and provided the following results.

Transverse Distortion Scale

The transverse scale controls the relative magnitude of the distortion velocity coefficients. A very large distortion with the scale in the order of the duct radius contributes primarily to the few lowest orders. For very small distortions with the scale in the order of one percent of the duct radius, the distortion coefficients are almost constant up to very high orders. In both cases, distortion coefficients of substantial magnitude contribute to non-propagating modes. It therefore can be assumed that there exists an intermediate range of scales where most of the significant distortion coefficients couple into propagating modes. The highest sound power levels are expected to occur in this intermediate range of scales. This is confirmed by the results presented in Figure 32, where the power level at the blade passing frequency is shown for the base case and a range of transverse scales. The results are based on the assumption that the maximum velocity is the same for all eddies independent of the transverse scale. For such eddies, the peak power level occurs at a transverse scale of about 10% of the duct radius or 50% of the rotor blade spacing in the fan tip region.

Distortion Velocity Components

In most situations the unsteady blade lift forces are dominated by the effects of the distortion velocity component normal to the blade surface. Due to the small relative mean flow angle in the fan tip region, a streamwise distortion velocity component produces a larger blade normal component than the corresponding transverse distortion component. For the same velocity scale, Gaussian eddies representing streamwise distortions therefore produce higher sound power levels. For the investigated rotor geometry the difference in the fan tone power level between the two distortion velocity components is 7.6 dB for eddies in the fan tip region (Figure 32) and reduces to zero dB at the hub. Only the Gaussian eddy is used to represent transverse as well as streamwise distortion velocities.

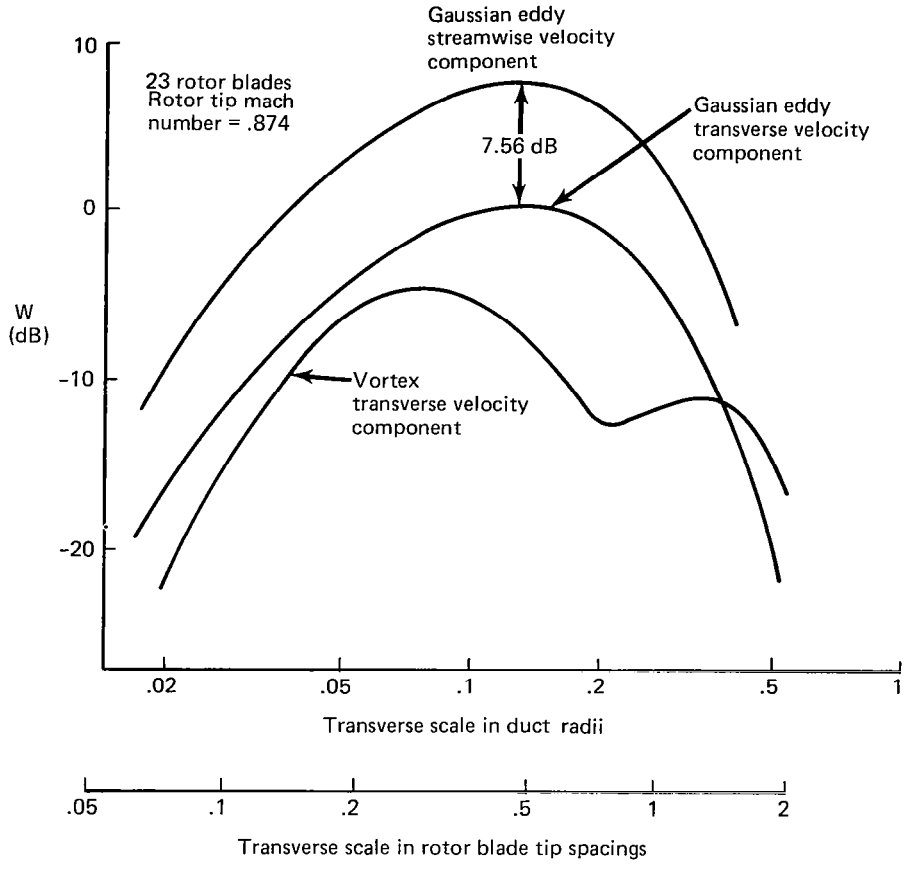

Figure 32.—Sound Power Level W as a Function of Transverse Scale for Various Distortion Elements

Distortion Elements, Gaussian Eddy and Vortex

The distribution of the distortion velocity coefficients for the base case, a Gaussian eddy, and the corresponding vortex are shown in Figure 33. The relationship between the distortion coefficients and the harmonic order is very similar for the two elements at the dominating radial locations. However, the two elements differ significantly in the radial distribution of the distortion coefficients. For the Gaussian eddy, the radial distribution is a nearly even function compared to an almost pure uneven function for the vortex. Based on these distributions, it can be expected that for distortion elements in the fan tip region the eddies couple well into the lowest radial order modes, whereas the vortex couples better into the higher radial order modes. This is confirmed in Figure 34 which shows the modal power distribution for the two distortion elements. The total sound power is shown as a function of the transverse scale in Figure 32. Both distortion elements show similar trends, with the power levels falling off at very small as well as at very large transverse scales. The significantly lower levels for the vortex at intermediate transverse scales must be due to the fact that a substantial amount of the distortion is lost to higher radial order modes, which do not propagate. This comparison points out the significance of the radial velocity distribution, which is frequently neglected.

Distortion Velocity Scale

The assumption of a constant velocity scale independent of the transverse length scale does not conform with the energy distribution in actual turbulence. A simple relationship between the velocity scale and the transverse length scale can be used to approximate the turbulence energy relationship in the inertial subrange. It is assumed that each discrete eddy represents the eddies within a range of transverse scales, which is small in comparison with and proportional to the transverse eddy scale. Based on the results of Section 4.3 it can be shown that the turbulent energy ΔE within such a range is

$$\Delta E = B_1 \, a^{2/3}$$

indicating that the energy is increasing with scale. In the same section it has been shown that the turbulence variance of a single scale eddy field is proportional to the product of the velocity scale squared and the eddy volume. In this simple representation, the eddy density and streamwise length scale are assumed to be independent of the transverse scale and therefore

$$\Delta E = B_2 \, c_1^{\,2} \, a^2$$

These 2 equations for the turbulent energy provide the relationship between velocity scale and transverse length scale in this simple representation of turbulence by single eddies

$$c_1^{\,2} = B_3 \, a^{-4/3} \qquad (5.1.11)$$

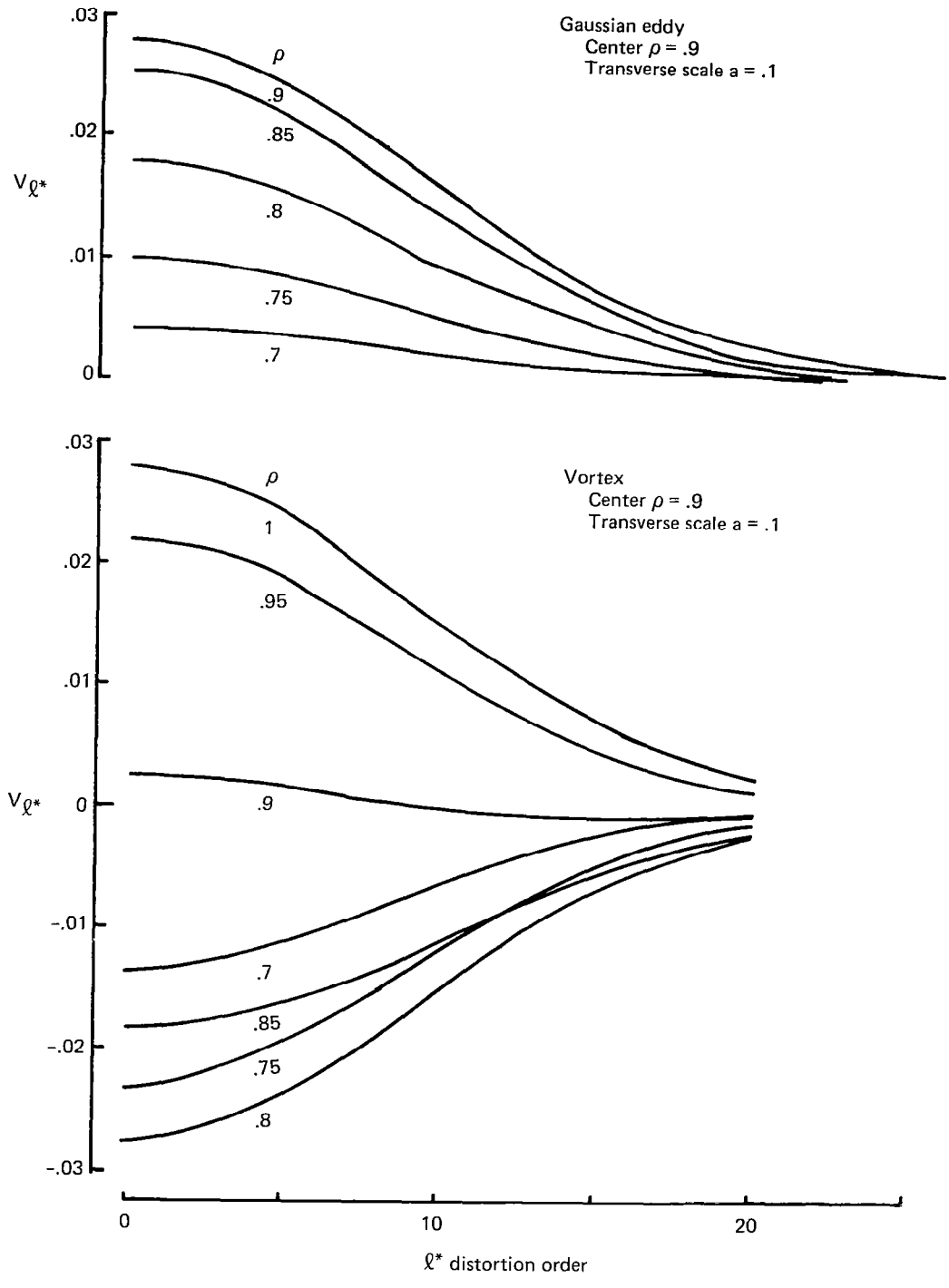

Figure 33.—Distortion Coefficients $V_{\ell *}$ for a Gaussian Eddy and a Vortex at Various Radial Locations ρ

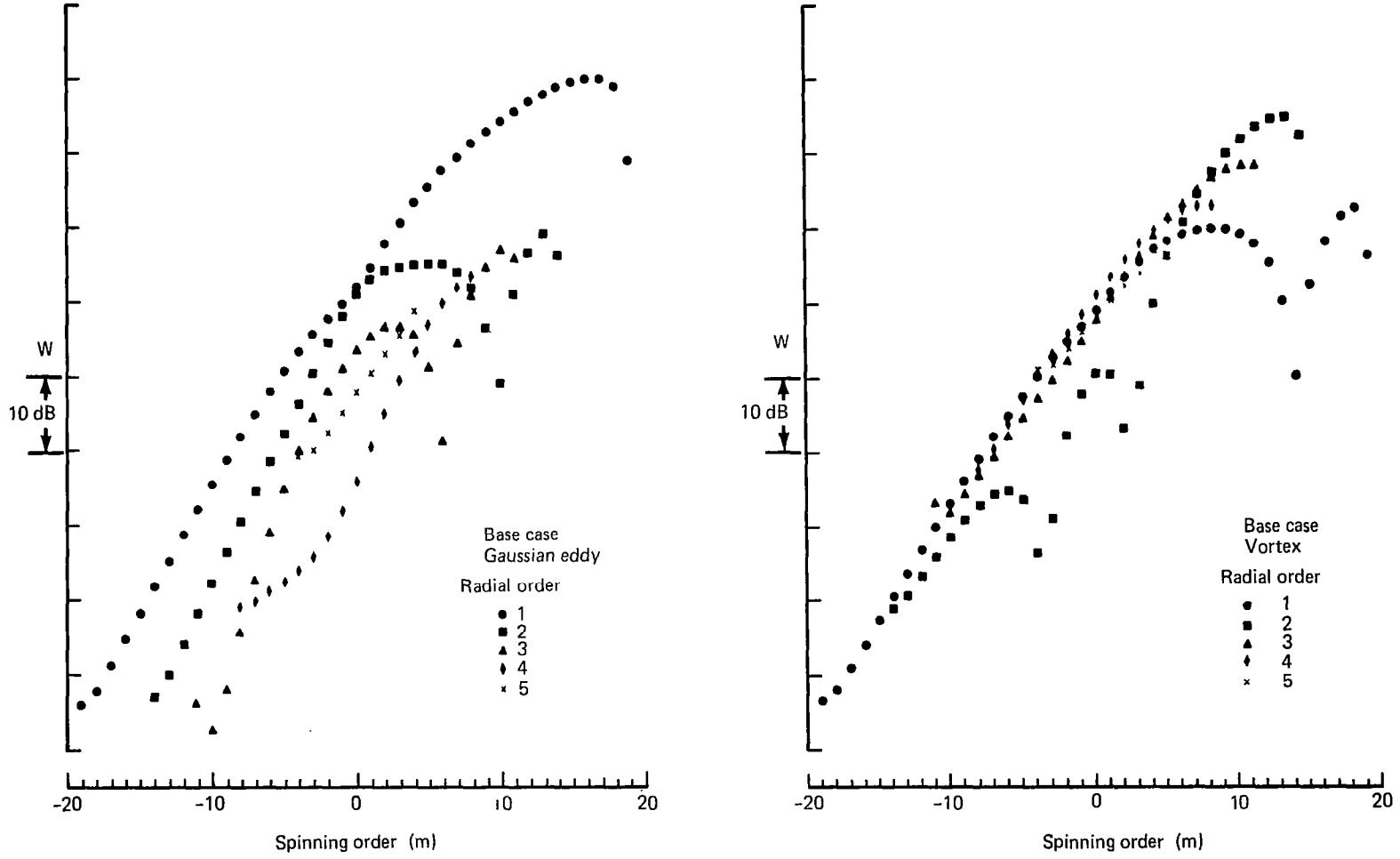

Figure 34.—Modal Power Distribution for Single Distortion Elements

The assumption of a constant velocity scale corresponds to an exponent of minus 3 in the inertial subrange, underestimating the energy in the small scales. The relationship of Equation (5.1.11) has been used to determine the relative sound power levels resulting from the eddies of different scales that represent the inertial subrange of a turbulence field. The following results are presented for the constant velocity scale as well as the relationship of Equation (5.1.11).

Rotor Blade Gap in the Fan Tip Region

This comparison is based on constant rotor solidity, the ratio between the total blading surface and the annular cross section. For a given rotor operating condition, the field of propagating modes at blade passing frequency is increasing with the number of rotor blades. Both the lower as well as the upper limit of the distortion orders contributing to propagating modes are increasing. It can therefore be expected that with increasing number of blades, the peak power level shifts towards smaller transverse scales. This is confirmed by the results shown in Figure 35. For the constant velocity scale data the peak occurs at transverse scales in the order of 50% of the blade gap in the fan tip region. For the case where the velocity scale is based on the turbulence energy distribution, it occurs at a transverse scale of about 25% of the blade gap. The following table summarizes the results for the JT9D and JT15D engines.

Engine	Inlet radius	Number of rotor blades	Transverse scale at peak power level					
			Constant velocity scale			Turbulence energy distribution		
	R_o(cm)	N	$\frac{a}{R_o}$	$\frac{a\,N}{2\pi R_o}$	a(cm)	$\frac{a}{R_o}$	$\frac{a\,N}{2\pi R_o}$	a(cm)
JT9D	118.	46	.08	.60	9.4	.04	.30	4.7
JT15D	27.	28	.11	.50	3.0	.065	.30	1.8

Mechanical Tip Mach Number

With increasing tip Mach number, the field of propagating modes widens and distortion coefficients of lower, as well as higher harmonic orders start to contribute to propagating modes. High sound power levels will occur at larger as well as smaller transverse scales. This trend is demonstrated by the results shown in Figure 36. The results also indicate a shift of the peak power level towards larger transverse scales with increasing tip Mach number. The peak occurs at transverse scales in the order of 30% to 60% of the fan blade gap for the constant velocity scale and at 20% to 30% of the blade gap for the velocity scale based on the turbulence energy distribution representing an inertial subrange.

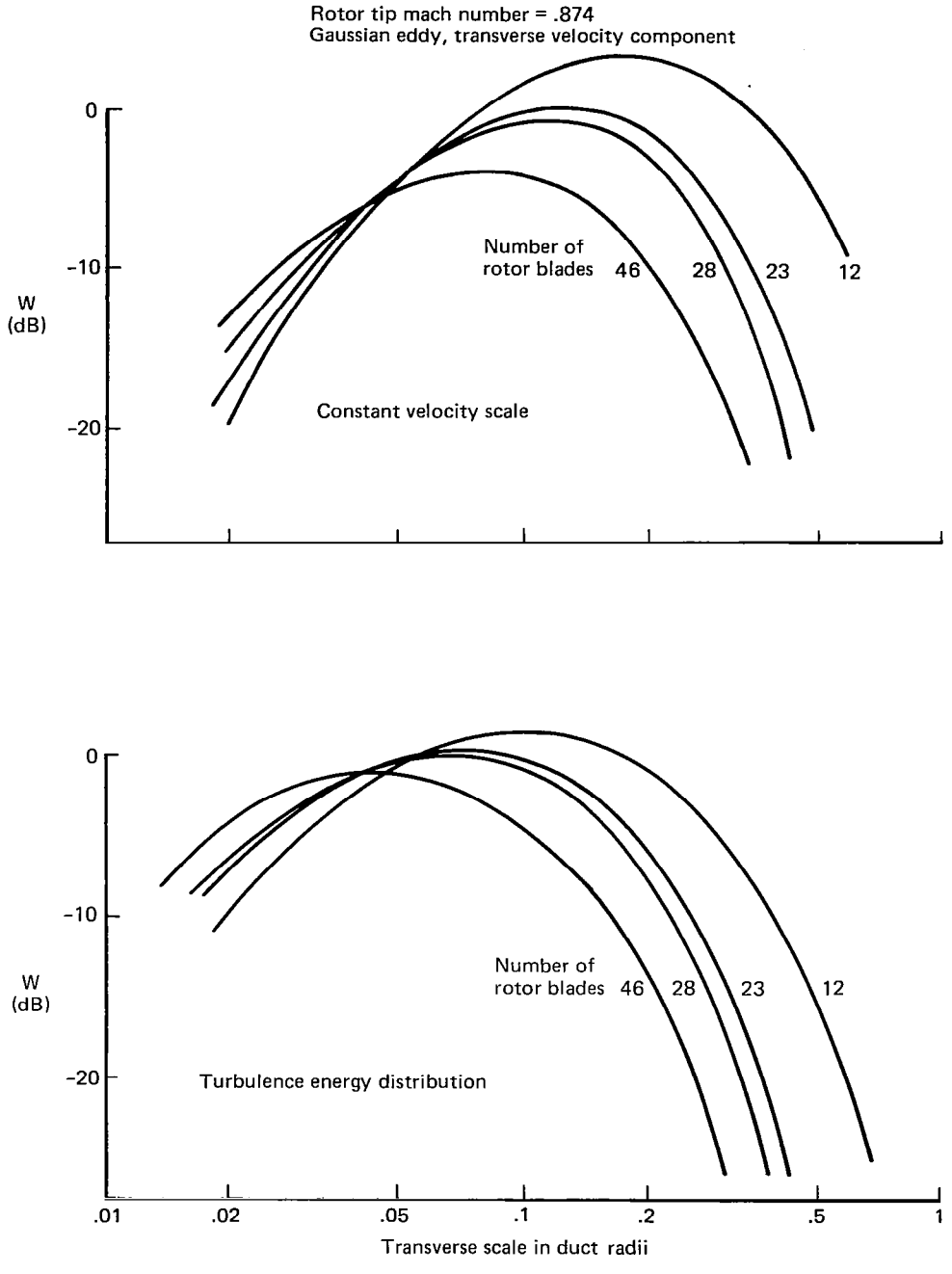

Figure 35.—Sound Power Level W as a Function of Transverse Scale for Various Numbers of Rotor Blades

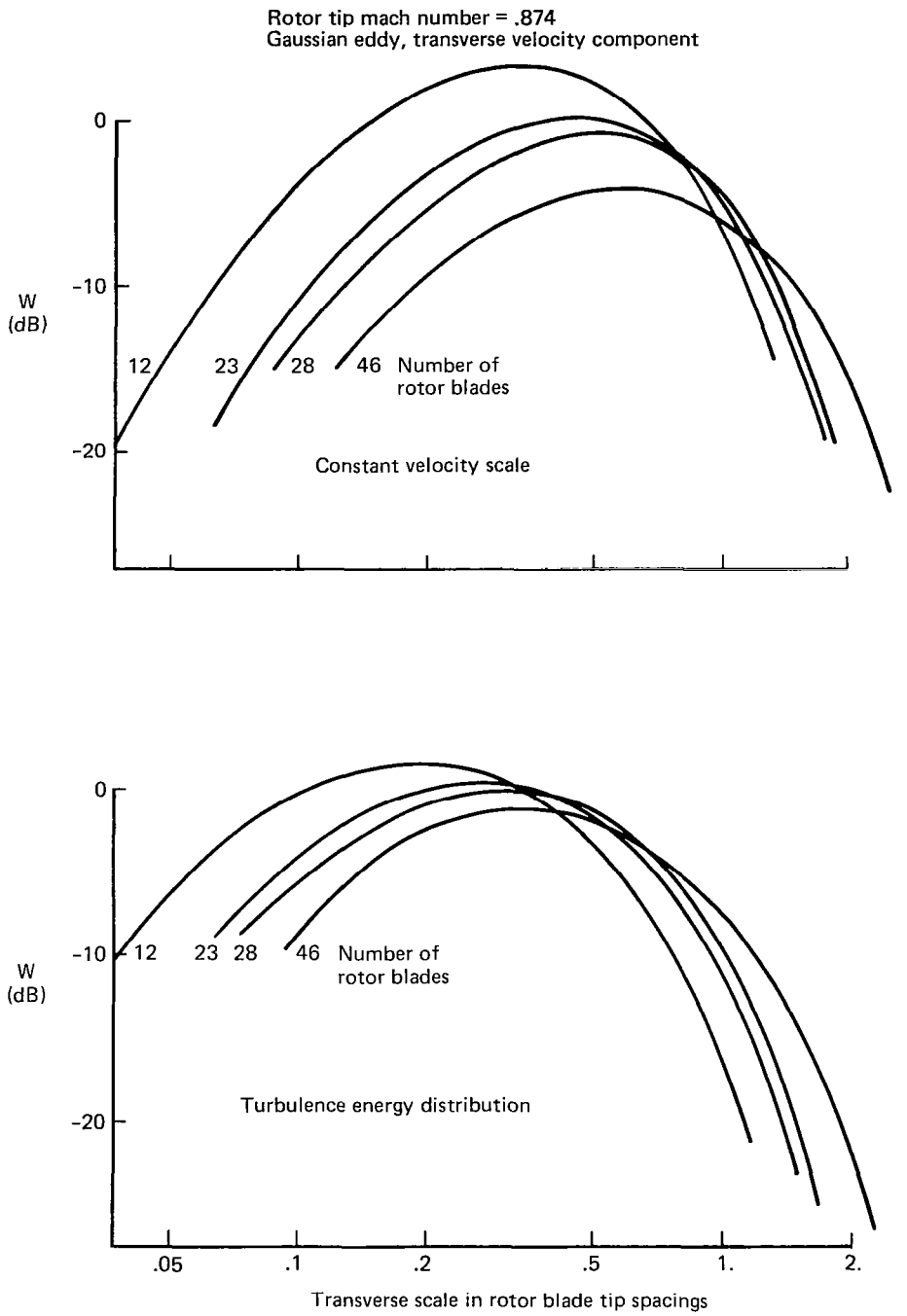

Figure 35 (Continued)

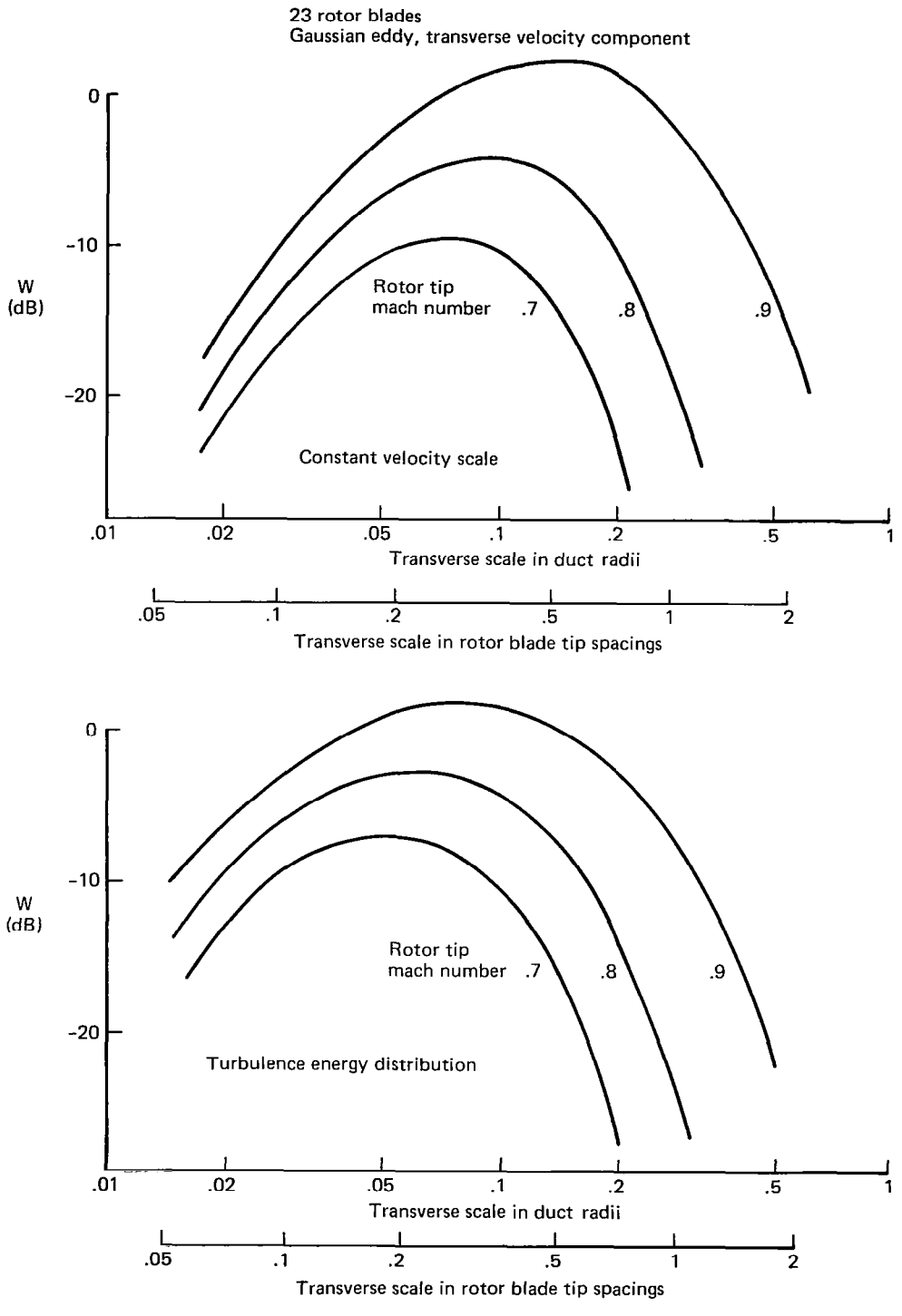

Figure 36.—Sound Power Level W as a Function of Transverse Scale for Various Rotor Tip Mach Numbers

5.2 ROTOR TONE NOISE DUE TO TURBULENCE

5.2.1 REVIEW OF ANALYSIS

The turbulence rotor tone noise model is an extension of the unsteady distortion model described in the preceding section. It computes the mean power level at the blade passing frequency and its harmonics resulting from a homogeneous turbulence field convecting through a fan. The turbulence is represented by a homogeneous distribution of distortion elements (eddies) as described in Section 4.3.

A convected eddy can be represented by an amplitude modulated distortion in the fan rotor plane. The sound pressure field resulting from a fan rotor cutting through such a distortion is not composed of pure tones, but narrowband sound centered around the blade passing frequency and its harmonics. The modulation spectrum appears in the sidebands of these frequencies. The primary subject of this study is tone noise and therefore only the sound pressure field within a narrowband is considered. The width (2B) of this band is assumed to be small in comparison with the blade passing frequency. It is further assumed that the sound pressure field of the $(m,n)^{th}$ mode of all the frequencies within such a band can be represented by a single mode at the center frequency. The equation for the amplitude of such a narrowband mode has been shown in the preceding section, where it also has been pointed out that this amplitude is modulated. An eddy convected through a fan creates a set of pulsed modes. For a given fan and fan operating condition, these pulses are a function of the eddy parameters

R, Φ eddy center coordinates
a, ℓ, c_1 eddy scales

The results of this section are presented in the form of sound power levels, which are a function of the mean squared mode amplitudes. The major task of the analysis is therefore to compute the mean squared mode amplitudes resulting from a homogeneous distribution of eddies convecting through a fan.

The mode amplitude as defined by equation (5.1.05) contains only one time dependent term

$$E^* = \frac{1}{\sqrt{2\pi}} \cdot \frac{\ell}{M} \int_{-B}^{B} e^{-\frac{1}{2}\left(\frac{\omega\ell}{M}\right)^2} \cos \omega t \, d\omega \qquad (5.2.01)$$

This function describes the mode amplitude pulse and becomes a Gaussian for large temporal scales ℓ/M and large bandwidth B. The determination of the mean square mode amplitudes is based on the turbulence representation used in Section 4.3. First, a set of identical eddies, Poisson distributed along a streamline is considered. The average occurrence rate at a stationary point is Q R $d\Phi dR$. Based on Lee (Ref. 36), the mean square value for such a pulse distribution is equal to the product of the pulse energy and the average occurrence rate. The energy of the mode amplitude pulse is

$$\int_{-\infty}^{\infty} |A_{mnk}|^2 dt = \left|\frac{A_{mnk}}{c_1 E^*}\right|^2 c_1^2 \int_{-\infty}^{\infty} (E^*)^2 dt \qquad (5.2.02)$$

with

$$\int_{-\infty}^{\infty} (E^*)^2 dt = \sqrt{\pi}\,\frac{\ell}{M}\,\mathrm{erf}\left(\frac{B\ell}{M}\right) \qquad (5.2.03)$$

The mean square mode amplitude due to Poisson distributed, identical eddies on a single streamline is therefore

$$\overline{|A_{mnk}|^2_{SL}} = \left|\frac{A_{mnk}}{c_1 E^*}\right|^2 c_1^2 \sqrt{\pi}\,\frac{\ell}{M}\,\mathrm{erf}\left(\frac{B\ell}{M}\right) Q\,R\,d\Phi dR \qquad (5.2.04)$$

For a homogeneous field of identical eddies Poisson distributed along all streamlines in the annulus and with independent distributions on all streamlines, the mean square mode amplitude becomes

$$\overline{|A_{mnk}|^2_{SS}} = 2\pi\sqrt{\pi}\,Q\frac{\ell}{M}\,\mathrm{erf}\left(\frac{B\ell}{M}\right) c_1^2 \int_{\eta}^{1} \left|\frac{A_{mnk}}{c_1 E^*}\right|^2 R\,dR \qquad (5.2.05)$$

In this formulation the interference between the solid annulus walls and the convected distortion elements has of course been neglected.

So far, only eddies of identical scales have been considered. In order to represent actual turbulence, the homogeneous field is composed of eddies with different length and velocity scales. In the general representation of the turbulent inflow field the scales a, ℓ and c are assumed to be random variables. The mean square mode amplitude resulting from such a field is

$$\overline{|A_{mnk}|^2} = \int_0^{a_{max}} \int_0^{\ell_{max}} \int_0^{c_{max}} \overline{|A_{mnk}|^2_{SS}}\, P(a, \ell, c)\, dc d\ell da \qquad (5.2.06)$$

with

$P(a, \ell, c)$ = joint probability density distribution for the eddy scales

$\overline{|A_{mnk}|^2_{SS}}$ = single scale mean square mode amplitude

In order to make the above integrations feasible, it is assumed that the eddy scales are statistically independent random variables, each with its own probability density distribution

$$P(a) \quad P(\ell) \quad P(c)$$

In order to conform with the model described in Section 4.3, Beta probability density functions are used for all three variables

$$P(t) = \frac{\Gamma\left(m_\ell + n_\ell + 2\right)}{\Gamma\left(m_\ell + 1\right)\,\Gamma\left(n_\ell + 1\right)}\, t^{m_\ell}\,(1-t)^{n_\ell} \qquad t = \frac{\ell}{\ell_{max}} \tag{5.2.07}$$

with

t = normalized random variable

Γ = gamma function

and the velocity scale and the length scales are related through the following deterministic relationship.

$$c_1{}^2 = c^2 \left(\frac{a}{a_{max}}\right)^{-\alpha} \left(\frac{\ell}{\ell_{max}}\right)^{-\beta} \tag{5.2.08}$$

Based on the assumption of statistical independence for the three random variables the integrations can be separated and the equation for the mean square mode amplitude is

$$\overline{|A_{mnk}|^2} = 2\pi\sqrt{\pi}\; Q \int_0^{c_{max}} c^2\, P(c)\, dc.$$

$$\int_0^{\ell_{max}} \frac{\ell}{M}\, crf\left(\frac{B\ell}{M}\right) \left(\frac{\ell}{\ell_{max}}\right)^{-\beta} P(\ell) d\ell \int_\eta^1 \int_0^{a_{max}} \left|\frac{A_{mnk}}{c_1\, E^*}\right|^2$$

$$\left(\frac{a}{a_{max}}\right)^{-\alpha} P(a)\, da\, R dR \tag{5.2.09}$$

In Section 4.3 formulas have been shown for the turbulence variance of a homogeneous random vortex and eddy field. Based on these equations ((4.3.15) and (4.3.25)), the mean square mode amplitudes can be related to the turbulence variance.

$$\overline{|A_{mnk}|^2} = 2d\left(\frac{\sigma}{M}\right)^2 \cdot \frac{H}{a_{max}^2} \int_0^1 t^{m_\ell + 1 - \beta} (1-t)^{n_\ell} \operatorname{erf}\left(\frac{Bt}{M}\, \ell_{max}\right) dt$$

$$\int_\eta^1 \int_0^1 \left|\frac{A_{mnk}}{c_1 E^*}\right|^2 S^{m_a - \alpha} (1-S)^{n_a}\, dS\, R\, dR \qquad (5.2.10)$$

$$H = \frac{\Gamma(m_a + n_a + 4 - \alpha)\, \Gamma(m_\ell + n_\ell + 3 - \beta)}{\Gamma(m_a + 3 - \alpha)\, \Gamma(n_a + 1)\, \Gamma(n_\ell + 1)\, \Gamma(m_\ell + 2 - \beta)} \qquad (5.2.11)$$

with

σ/M = turbulence intensity

d = 1. for Gaussian eddy

= 2/e for Vortex

$S = \frac{a}{a_{max}}$

The integrals in equation (5.2.10) are solved by numerical methods.

The mean acoustic power resulting from a homogeneous random eddy field convected through a fan rotor is computed with equation (5.1.09) based on the mean square mode amplitudes. The cutoff criterion is again used to select the propagating modes. It is assumed that the cutoff condition at the blade passing frequency and its harmonics is approximately valid for all frequencies within the band of width 2B.

5.2.2 RESULTS

A parametric study of rotor tone noise due to convected turbulence has been conducted based on the model described in the preceding section. The purpose of this study is to determine the sensitivity of the sound power level at blade passing frequency to various turbulence and fan rotor parameters. The study is based on the fan geometry described in Section 5.1.2. The fan operating conditions are again limited to the approach power range,

high subsonic tip speeds. The parameters investigated, their ranges and the reference case are shown in the following table.

Parameter	Range	Base case
Number of rotor blades	12 46	23
Mechanical tip Mach number	.7 .874	.874
Relative tip Mach number	.745 .930	.930
Transverse integral length scale (duct radii)	.01 .5	.5
Streamwise integral length scale (duct radii)	.1 100.	100.
Distortion velocity component	streamwise, transverse angular	transverse angular
Distortion element	vortex Gaussian eddy	Gaussian eddy

The parametric study of rotor tone noise due to convected turbulence has provided the following results:

Turbulence Variance

Equation (5.2.10) indicates that the sound power is proportional to the relative turbulence variance $(\sigma/M)^2$, which is the same for all results shown in this section.

Transverse Integral Scale

The effect of the transverse integral scale on the sound power level seems to be rather small, as indicated in Figure 37. Especially at large integral scales, the power level decreases at a small rate. At first this seems to be in contradiction with the unsteady distortion results shown in Section 5.1.2, where the power level dropped off very rapidly with increasing scale. It must be emphasized that we are now considering the sound pressure field due to a field of distortion elements of various sizes, whereas the results of Section 5.1.2 are based on single distortion elements. The results of this section simply indicate that even for large integral scales there is a sufficient amount of energy in the eddies with smaller scales that dominate the contributions to the sound pressure field. Based on the spectral distribution of the turbulent energy, the sound power assumes an exponential relationship with the integral scale at scales that are sufficiently larger than the scale at the peak power level. The exponent is (-2/3), due to the (-5/3) exponent for the inertial subrange of the turbulence and the assumption of a constant turbulence variance (see Fig. 10). The peak power level occurs at a transverse integral scale similar to the transverse eddy scale predicted by the unsteady distortion results.

Turbulence Components

In Section 5.1.2 it has been pointed out that the streamwise turbulence component has a larger blade normal velocity component than the transverse turbulence component in the rotor tip region. For turbulence of the same variance and spectral distribution, this results in higher sound power levels for the streamwise component. For a homogeneous distribution

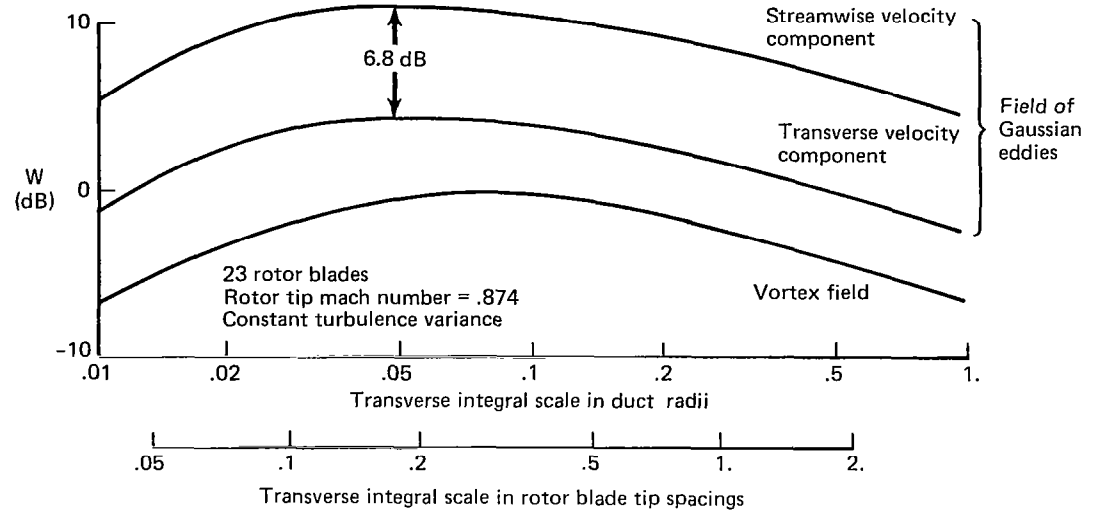

Figure 37.—Sound Power Level for Homogeneous Distributions of Various Distortion Elements

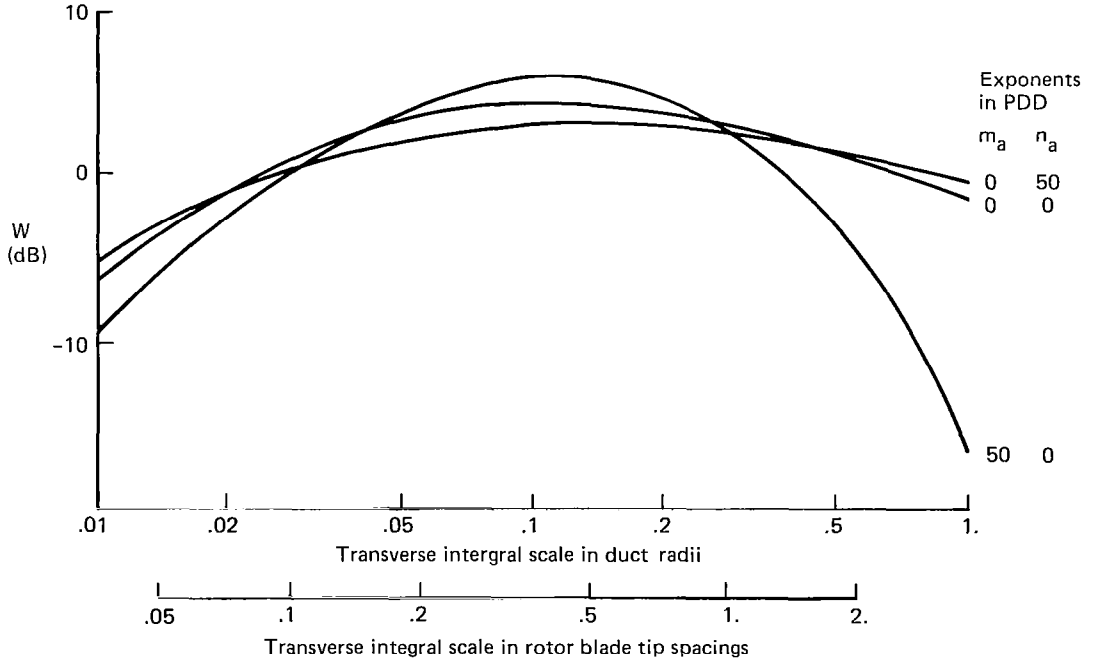

Figure 38.—Sound Power Level as a Function of Transverse Integral Scale for Various Transverse Scale Distributions

of Gaussian eddies representing turbulence of the same intensity for the streamwise and the transverse turbulence components, the difference in the sound power level is 6.8 dB (Fig. 37).

Distortion Elements, Gaussian Eddy or Vortex

The sound power level due to a Gaussian eddy field and a vortex field are compared in Figure 37. As in the unsteady distortion results, the power levels for the vortex field are significantly lower. The reason for these lower levels is the fact that the sound pressure field due to a vortex does not couple well into the lower radial order modes. This is demonstrated by the modal power distributions shown in Figures 39 and 40. The power levels of the highest radial order (n = 3) modes are very similar, but for the lowest radial order (n = 1) the power levels are much higher for the Gaussian eddy field. This difference decreases with increasing power contribution from higher radial order modes, for example, for rotors with large numbers of blades and high fan tip Mach numbers.

Probability Density Distribution (PDD) for the Transverse Scale

In Section 4.3.3 it has been shown that the PDD for the scales have a significant effect on the turbulence spectra. It is therefore of interest to know their effect on the corresponding sound power levels which result from the turbulence convecting through a fan rotor. Three PDD's are considered: the standard PDD (m_a = .0, n_a = .0) which has been used to compute the bulk of the data presented in this report; a right-sided PDD (m_a = 50., n_a = .0) with its highest probability densities close to the maximum scale, and a left-sided PDD (m_a = .0, n_a = 50.) with its highest probability densities in the smallest scales. Sound power levels for the three distributions as a function of transverse integral scale are shown in Figure 38. The largest deviations from the power levels based on the standard PDD occur for the right-sided PDD. The latter approximates a delta function at a scale close to the maximum scale, and the spectrum for the transverse wavenumber component approaches the shape of a Gaussian distribution function. This explains the rapid decrease of the sound power levels at large integral scales for this distribution, similar to the results reported in Reference 38.

Rotor Blade Spacing

This comparison is based on constant rotor solidity. Sound power levels for fan rotors with different numbers of blades are shown in Figure 41 as a function of the transverse integral scale. The peak power levels are nearly the same but occur at different transverse integral scales. The scales corresponding to the peak power levels are in the order of 25% of the rotor blade gap. The following table summarizes the results for the JT9D and JT15D engines.

Engine	Inlet radius R_o(cm)	Number of rotor blades N	Transverse integral scale at peak power level		
			$\frac{L}{R_o}$	$\frac{L\,N}{2\pi R_o}$	L(cm)
JT9D	118.	46	.035	.25	4.1
JT15D	27.	28	.05	.25	1.3

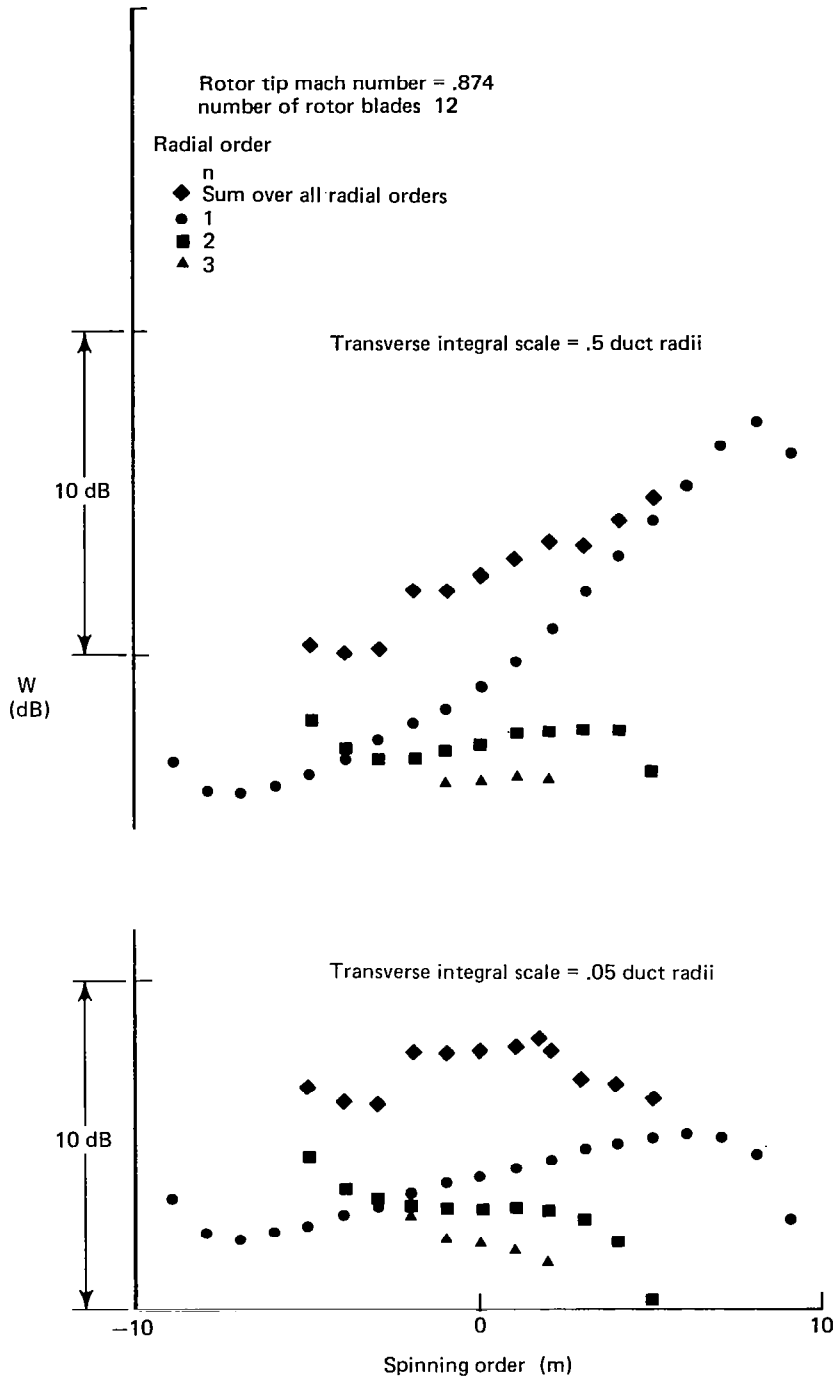

Figure 39.—Modal Power Distribution for a Field of Gaussian Eddies

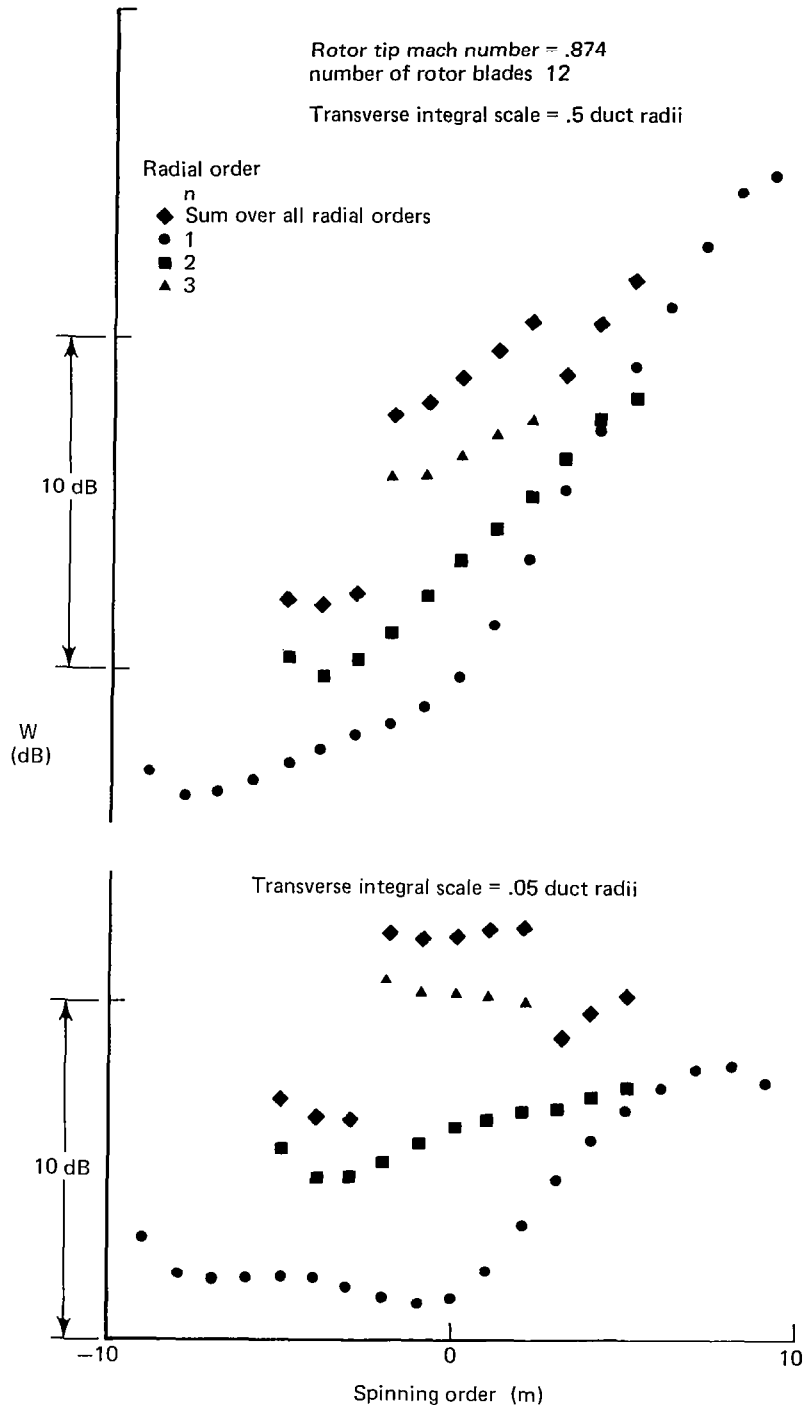

Figure 40.—Modal Power Distribution for a Vortex Field

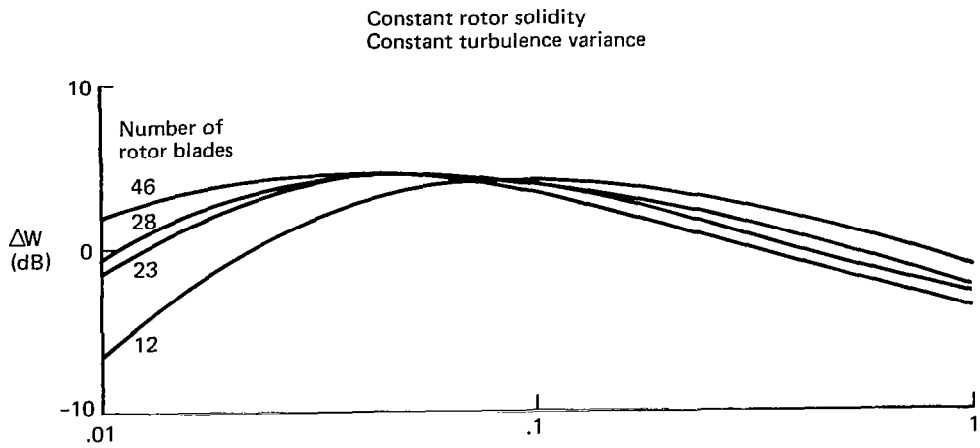

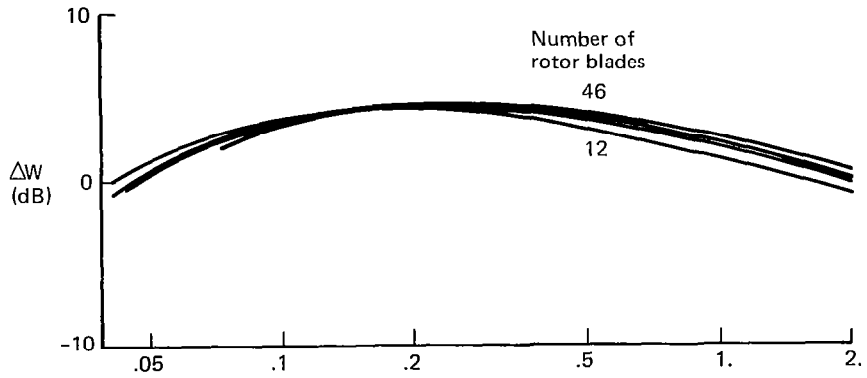

Figure 41.—Sound Power Level as a Function of Transverse Integral Scale for Various Numbers of Rotor Blades

In Figure 42 the cumulative power level is shown as a function of the upper bound on the scale distribution. In these results, only a limited segment of the total scale distribution has been considered, namely the scales smaller than the transverse scale limit. The cumulative power level represents the sound power resulting from all the eddies smaller than the scale limit within a fixed scale distribution. The minus 3 dB point (the half power point) occurs at scales in the order of 25% of the rotor blade gap. The results also show that only a very small amount of sound power is generated by scales larger than about four times the scale at the peak power level. This indicates again that even though the power level is only a weak function of the integral transverse scale, the bulk of the sound power is generated by a narrow range of transverse scales centered around a transverse scale of about 25% of the rotor blade spacing in the fan tip region.

Tip Mach Number

Results for three different tip Mach numbers are presented in Figure 43. The results show that the peak power level shifts towards larger integral scales with increasing tip Mach number. The increase in the power level with the tip Mach number is scale dependent. Based on the data the exponent of the Mach number in a power law relationship with the sound power would vary between 4 and 7.

Higher Order Harmonics of the Blade Passing Frequency

Power levels for the second and fourth harmonic of the blade passing frequency are shown in Figure 44. The data demonstrate a clear dominance of the blade passing frequency over its harmonics. The presented results are based on a rotor with 12 blades. For the larger blade numbers (23 or 46) the blade passing frequency would dominate throughout the whole range of investigated transverse integral scales.

Streamwise Integral Scale

The effect of the streamwise scale distribution on the mean square mode amplitudes and the sound power is represented by the integral over the normalized streamwise scale parameter t in equation (5.2.10). For a given scale distribution, a set of exponents m_ℓ and n_ℓ, this integral is only a function of the parameter combination $(B \cdot \ell_{MAX}/M)$. Therefore the mean square mode amplitudes as well as the sound pressure level resulting from a given scale distribution can be presented as a function of this parameter combination. The maximum scale ℓ_{max} can be substituted with the integral scale L and the parameter group can be presented in various forms.

$$Q = \frac{1}{2\pi}\,\frac{BL}{M} = \frac{1}{2\pi}\,BT = S\frac{B}{\omega_o} = \frac{1}{2\pi}\,\frac{B}{\omega_o}\,\frac{M_{tip}}{M}\,NL$$

with

T	=	temporal integral scales
S	=	number of rotor blades cutting through an eddy of length L
ω_o	=	angular blade passing frequency
N	=	number of rotor blades

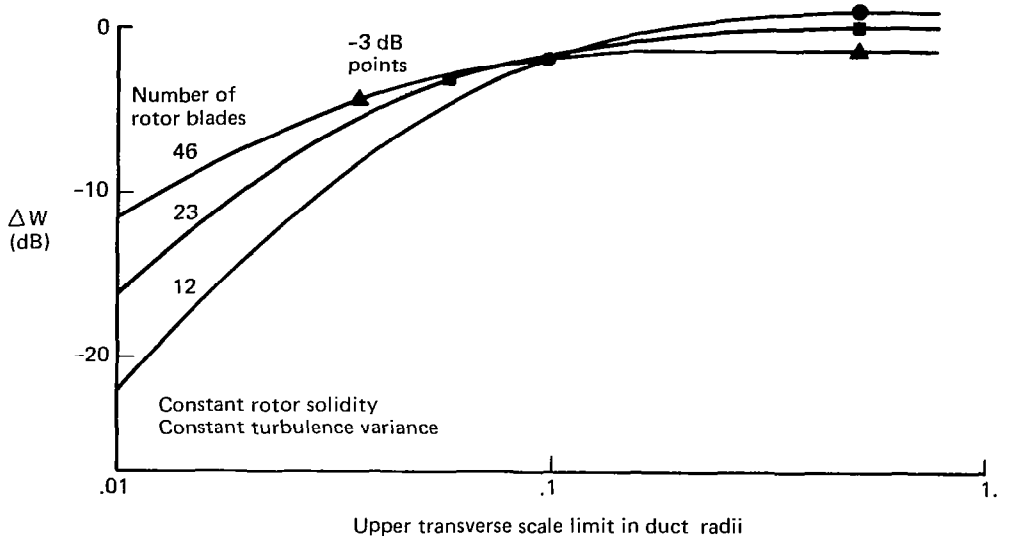

Figure 42.—Sound Power Level as a Function of the Upper Limit on the Transverse Scale Range

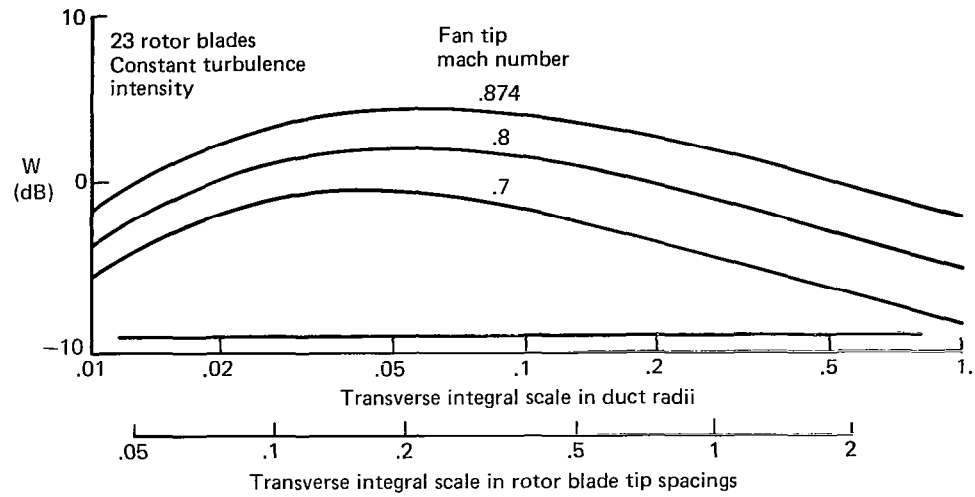

Figure 43.—Sound Power Level as a Function of Transverse Integral Scale and Fan Tip Mach Number

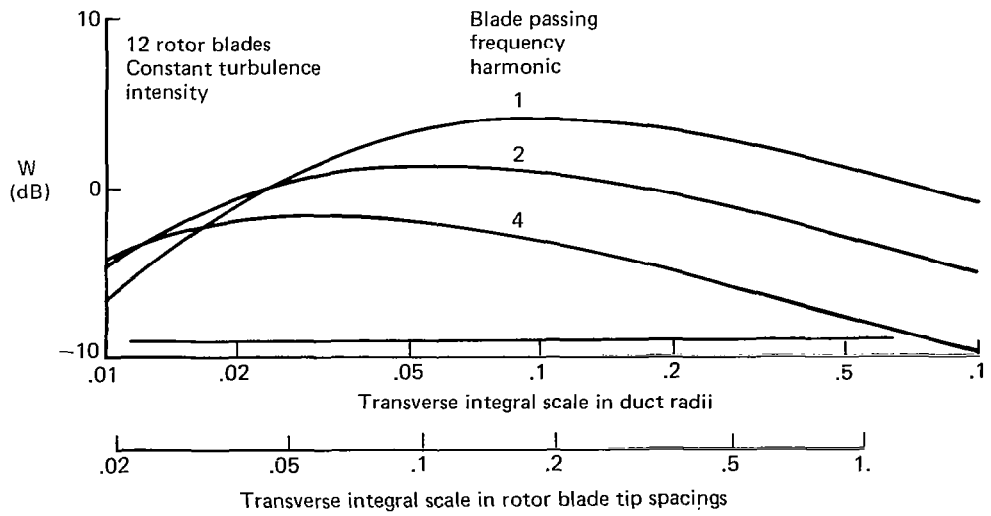

Figure 44.—Sound Power Level as a Function of Transverse Integral Scale for Several Blade Passing Frequency Harmonics

All parameters are non-dimensionalized with the inlet radius and the speed of sound. For the selected scale distribution ($m_\ell = n_\ell = .0$) the sound power level is presented as a function of Q in Figure 45. The nature of the relationship can be explained by the characteristics of the error function. For small values of Q the sound power level is proportional to it. At large values of Q the sound power level becomes independent of it. The minus 2 dB point which represents about two-thirds of the maximum sound power occurs roughly at the point where the two limit solutions intersect and the corresponding value for Q is about .25. This value can be used to define the conditions for which most of the power of rotor tone noise due to convected turbulence is concentrated within a band of width 2 B around the blade passing frequency and its harmonics. For the selected fan geometry the conditions are:

$$L > \frac{\pi}{2}\frac{M}{B} \qquad T > \frac{\pi}{2B} \qquad S > .25\frac{\omega_o}{B} \qquad L > \frac{\pi}{2}\frac{\omega_o}{BN}\cdot\frac{M}{M_{tip}}$$

If the bandwidth (2 B) is 1% of the blade passing frequency, then the average eddy of integral scale L should be cut by 50 rotor blades. For a fixed bandwidth the length scale requirements are independent of the number of rotor blades and the rotor size.

5.3 ROTOR TONE NOISE DUE TO ATMOSPHERIC TURBULENCE

5.3.1 BACKGROUND

It has long been known that steady and unsteady distortions in the inflow field of the fan of a stationary engine can cause significant fan noise levels in the vicinity of the blade passing frequency and its harmonics (Refs. 1 through 6). These distortions have been attributed to the atmospheric turbulence, the ground vortex and the flow field around the test stand structure (Refs. 5 through 8). The interference of these distortions with the inlet boundary layer and the resulting distortions have also been suggested as a significant cause of fan tone noise (Refs. 6 and 20). Most of these distortions do not exist in flight and as a result of this, the fan sound pressure field changes significantly between the two conditions. The distortions associated with the atmospheric turbulence are present throughout the atmospheric boundary layer and therefore could possibly affect fan noise along the approach flight path. Very little work has been done in the assessment of fan tone noise due to atmospheric turbulence in flight. A Boeing report used simple turbulence and acoustic models to estimate fan tone noise due to atmospheric turbulence and showed significant differences between static and flight conditions. In this section these differences are evaluated based on the models described in the preceding sections. The tone noise generation due to atmospheric turbulence convected through a fan is a rather complex process. Many simplifying assumptions had to

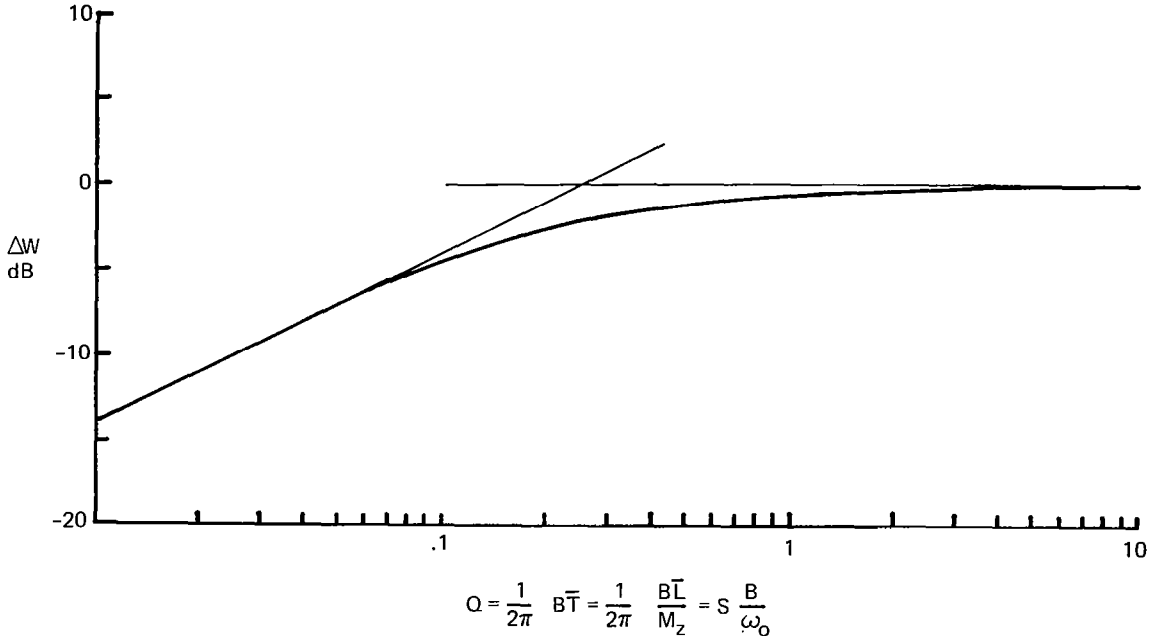

Figure 45.—Combined Effect of Bandwidth B and Integral Temporal Scale $\bar{T}$ on Sound Power Level

be made in order to provide a prediction based on analytical models. Due to these simplifications, the results must be considered rough estimates at best. The study is only concerned with the changes in the sound source, differences in the sound propagation and radiation are not considered.

5.3.2 APPROACH

In this study it is assumed that the turbulence convecting through a fan evolves from the turbulence in the atmospheric boundary layer. In this process a small segment of the entire boundary layer is strained by the fan inflow field and is ingested into the fan. The difference in the resulting fan tone noise between static and flight conditions is due to two principal causes.

- Differences in the inflow contraction between the ambient and fan face conditions.
- Changes in the atmospheric turbulence with altitude and the surrounding environment.

In the following outline of the approach, an approximate relationship between the turbulence involved in the tone noise generation and the turbulence of the atmospheric boundary layer is derived. The results presented at the end of this section are based on the exact equations of the models described previously.

Atmospheric Turbulence

The description of the atmospheric turbulence is based on the model of Section 4.1. The turbulence is characterized by its large scale. All integral scales increase with altitude. The streamwise integral scale of the vertical turbulence component is

$$L_w = .5\ z \tag{5.3.01}$$

The turbulence standard deviations are proportional to the friction velocity $u_{\bigstar o}$, which is a function of the wind velocity U_{ref} and the surface roughness z_o. It can be approximated by

$$u_{\bigstar o} = .4\ \frac{U_{REF}}{\ell n\left(\frac{z_{REF}}{z_o}\right)} \tag{5.3.02}$$

For neutral stability the relationship between the standard deviation of the vertical turbulence component σ_w and the friction velocity is

$$\sigma_w = 1.3 \cdot u_{\bigstar o} \tag{5.3.03}$$

In the first order approximation σ_w is independent of altitude. These three relationships indicate that the spectral distribution of the turbulence must change with altitude. Due to this the turbulence is assumed homogeneous only in horizontal planes.

In neutral atmospheric conditions, the mean wind velocity can be approximated by

$$U = 2.5\, u_{*_0}\, \ell n\left(\frac{z}{z_0}\right) = U_{REF}\, \frac{\ell n\left(\frac{z}{z_0}\right)}{\ell n\left(\frac{z_{REF}}{z_0}\right)} \qquad (5.3.04)$$

The preceding formulas are used to describe the atmospheric turbulence in the approximate relationship between the turbulence involved in fan tone noise generation and the atmospheric turbulence.

The Inflow Streamtube

The inflow field of a fan can be described as a streamtube in the ambient flow field. The size (radius R_A) of this streamtube is a function of the contraction ratio ℓ_1, and the radius of the inlet R_0

$$R_A \cong R_0 \sqrt{\ell_1} \qquad (5.3.04)$$

The contraction ratio is defined as the ratio between the mean flow velocity at the fan face and the relative velocity between the inlet and the ambient air. The latter is the local wind velocity U(z) in static conditions, and the airplane velocity V_{ap} in flight conditions. This streamtube is approximately circular in flight and its diameter is in the order of the inlet diameter. In static tests, where the wind velocities are required to be small, the streamtube becomes very large and thus the mean flow velocity distribution within the tube cannot be assumed uniform.

For several reasons, it is desireable to define the turbulence associated with distortion elements of transverse scales smaller than the radius of the inflow streamtube.

- In static tests, elements with scales in the order of the streamtube radius are only partially affected by the inflow contraction. The increase in the energy of the transverse turbulence component of such elements will not be as large as for smaller elements, completely contained within the streamtube.

- In the turbulence model of Section 4.3 which forms the basis of the rotor tone noise model of Section 5.2, it is assumed that the streamwise and transverse length scales are statistically independent random variables. This assumption can lead to unrealistic results, if the range of scales contributing significantly to rotor tone noise comprises only a small segment of the total distribution of scales.

- Distortion elements of the transverse turbulence component with scales in the order of their separation distance from the inlet surface are suppressed.

- The results of Sections 5.1 and 5.2 indicate that the distortion elements with transverse length scales in the order of one-half of the duct radius or larger contribute only a negligible amount to the sound pressure field resulting from convected turbulence.

For these reasons, the study of rotor tone noise due to atmospheric turbulence will be based on the turbulence resulting from the scales smaller than one-half of the streamtube radius.

$$a \leqslant .5\ R_A$$

The atmospheric turbulence due to a limited scale range is determined with the inflow turbulence model of Section 4.3. Spectra based on this model representing different ranges of scales are shown in Figure 31. Based on this simple model, the variances σ^2 and the integral scales L of the limited (subscript A) and the full range of scales are related by the following equation:

$$\frac{\sigma_A^2}{\sigma^2} = \left(\frac{L_A}{L}\right)^{2/3} \tag{5.3.05}$$

This relationship is of course based on spectra with an inertial subrange exponent of (-5/3).

Various investigators (Refs. 26 and 27) have shown that atmospheric turbulence becomes isotropic at wavelengths small in comparison with the altitude above ground. Teuniessen (Ref. 21) suggests that isotropy occurs for wavelengths $< z/3$.

In the flight condition, the mean flow velocity is uniform throughout the streamtube and the maximum scale of the limited scale range is only a small fraction of the altitude. The turbulence based on the limited scale range is therefore homogeneous and isotropic.

In static conditions, the situation is more complex. The wind velocity varies significantly across the streamtube. Depending on the streamtube size and the engine height above the ground, the maximum scale of the limited scale range can be in the order of the altitude above the ground. The precontraction turbulence is therefore neither homogeneous nor isotropic. The flow contraction model is, however, based on isotropic, homogeneous turbulence. Some simplifying assumptions must be made in order to conform with the requirements of this model.

At low altitudes, the vertical turbulence component has a smaller variance and integral scale than the horizontal components. In the spectra, this difference manifests itself in the dominance of the horizontal components at small wavenumbers. It is assumed that this large scale horizontal motion does not contribute to the turbulence in the fan inflow field.

At large wavenumbers the spectra of the three components merge. A limited segment of the atmospheric turbulence is assumed to be isotropic. The integral scales and variances of this turbulence are assumed to be equal to the corresponding values for the vertical component.

$$L = L_w \qquad \sigma = \sigma_w \tag{5.3.06}$$

The range of scales that is used to represent the turbulence in the fan inflow field is a function of the relative size of the streamtube and the integral scale L_w. For the selected scale distributions with the exponents m and n set equal to zero, the ratio between the maximum scale and the integral scale is 1.41. Therefore, if the maximum scale of the considered scale range is one-half of the streamtube radius,

$$a_{max} = .5\ R_A$$

Then the integral scale of the precontraction turbulence is

$$L_A = .355 \cdot R_A$$

If this integral length scale is smaller than the integral length scale of the vertical turbulence component L_w then only a limited scale range of the actual turbulence is considered. But if the length scale based on the above equation is larger than L_w, then the full spectrum of the vertical turbulence component is used. These two conditions are described by the following equations.

$$L_w > .355\ R_A \qquad \frac{\sigma_A^2}{\sigma_w^2} = \left(\frac{.355\ R_A}{L_w}\right)^{2/3}, \quad L_A = .355\ R_A$$

$$L_w \leq .355\ R_A \qquad \sigma_A = \sigma_w \qquad , L_A = L_w \tag{5.3.07}$$

Based on the approximate equations for the atmospheric turbulence and the assumption $L_w > .355\ R_A$, the standard deviation for the fan inflow turbulence is

$$\sigma_A = \sigma_w \left(\frac{.355\ R_A}{L_w}\right)^{1/3} \qquad R_A = R_o \left(\frac{U_B}{U}\right)^{1/2} \tag{5.3.08}$$

$$\sigma_A = .472\ R_o^{1/3} \cdot U_{REF}^{5/6} \cdot U_B^{1/6} \cdot Z^{-1/3} \frac{1}{\left(\ln \frac{z}{z_o}\right)^{1/6} \left(\ln \frac{z_{REF}}{z_o}\right)^{5/6}} \tag{5.3.09}$$

Inflow Contraction

The effects of the inflow contraction are estimated based on the contraction models of Section 4.2. The model is used to compute the post contraction integral scales and variances. In the first order approximation, it is assumed that the scales are changed proportional to the corresponding contraction ratios. The post-contraction standard deviations of the turbulence are approximated with Prandtl's formulas

$$\sigma_{1B} = \frac{1}{\ell_1}\ \sigma_A \qquad \sigma_{2B} = \sqrt{\ell_1}\cdot\sigma_A \tag{5.3.10}$$

which lead to the following approximate formulas for the fan face turbulence intensities.

$$\frac{\sigma_{1B}}{U_B} = .472\left(\frac{R_o}{z}\right)^{1/3}\left(\frac{U_{REF}}{U_B}\right)^{11/6}\frac{\left(\ell n\ \frac{z}{z_o}\right)^{5/6}}{\left(\ell n\ \frac{z_{REF}}{z_o}\right)^{11/6}} \tag{5.3.11}$$

$$\frac{\sigma_{2B}}{U_B} = .472\left(\frac{R_o}{z}\right)^{1/3}\left(\frac{U_{REF}}{U_B}\right)^{1/3}\frac{1}{\left(\ell n\ \frac{z}{z_o}\right)^{2/3}\left(\ell n\ \frac{z_{REF}}{z_o}\right)^{1/3}} \tag{5.3.12}$$

The above equations represent first order approximations for the static test conditions. In-flight conditions the airplane velocity U_{AP} enters the contraction ratio

$$\ell_1 = \frac{U_B}{U_{AP}} \tag{5.3.13}$$

and the corresponding approximate equations for the turbulence standard deviations are:

$$\frac{\sigma_{1B}}{U_B} = .472\left(\frac{R_o}{z}\right)^{1/3}\frac{U_{REF}}{U_B}\left(\frac{U_{AP}}{U_B}\right)^{5/6}\frac{1}{\ell n\left(\frac{z_{REF}}{z_o}\right)} \tag{5.3.14}$$

$$\frac{\sigma_{2B}}{U_B} = .472 \left(\frac{R_o}{z}\right)^{1/3} \frac{U_{REF}}{U_B} \left(\frac{U_B}{U_{AP}}\right)^{2/3} \frac{1}{\ell n \left(\frac{z_{REF}}{z_o}\right)} \qquad (5.3.15)$$

Fan Tone Noise

Differences in fan tone noise due to atmospheric turbulence between static and flight conditions are evaluated with the model described in Section 5.2. In this comparison the turbulence intensities, the streamwise and transverse length scales and the general character of the spectral distributions are taken into account.

In static conditions the turbulence at the fan face is dominated by the transverse component. Due to the large contraction in the inflow field the turbulence is well represented by a vortex field. In flight conditions all turbulence components are of similar magnitude due to the small inflow contraction ratio. According to the results of Section 5.2 the streamwise turbulence component causes significantly higher noise levels in such conditions, due to the fact that it has a larger blade normal velocity component. For the small contraction ratios typical for the flight condition the turbulence is represented with distributions of Gaussian eddies.

5.3.3 RESULTS

A limited parametric study of rotor tone noise due to atmospheric turbulence has been conducted to estimate the difference between static and flight conditions. The study is based on the exact equations of the models described in the preceding sections and on the approach outlined in Section 5.3.2. It is limited to the approach power range and the rotor geometry is described in Section 5.1.2. In Section 5.2.2 rotor tone noise due to homogeneous but anisotropic turbulence has been investigated for different fan rotors and operating conditions. The following study is primarily concerned with the effects of the parameters that describe the atmospheric turbulence. It is based on the fan size of a JT9D engine and is centered around two reference conditions representing static and flight tests.

Reference conditions	Static	Flight
Altitude	4.88 m	120 m
Reference altitude	4.88 m	10 m
Wind velocity at reference altitude	2.68 m/s	5.14 m/s
Richardson number at reference altitude	.0	.0
Roughness scale	.2 m	.02 m
Boundary layer thickness	600 m	
Equivalence altitude	600 m	
Airplane velocity	.0	82.3 m/s
Rotor radius	1.16 m	
Axial Mach number at fan face	.35	
Relative tip Mach number	.93	
Number of rotor blades	23	
Bandwidth 2B	1% of BPF	

The static condition represents typical test stand operation. The engine axis is 4.88 m (16 ft) above the ground. The wind velocity at engine axis height is 2.68 m/s (6 MPH) which represents an upper limit on winds from the forward arc. This limit is usually lower for wind directions at an angle relative to the inlet axis and drops further for crosswinds and winds from the aft arc. The flight condition is based on landing approach at the FAR Part 36 measuring station. The wind velocity corresponds to the upper limit of the test window.

According to Reference 22 a roughness scale of .02 meters is typical for airport environments and is used for the flight condition. A value of .2 meters has been selected for the static test stand environment.

A boundary layer thickness of 600 meters as suggested in References 21 and 23 has been used. Throughout this study it is assumed to be invariant and the same for both conditions.

Since this study is concerned with narrowband noise only, the rotor noise within a small band centered around BPF is considered. A bandwidth of 1% of BPF has been assumed.

Comparison of the Two Reference Conditions

The difference in fan narrowband noise due to atmopheric turbulence between static and flight conditions is due to the following discrepancies:

- At the low wind velocities of static tests (2.68 m/s, 6 MPH) a large flow field contraction exists between the ambient and the fan face conditions. This contraction causes an increase in the transverse turbulence velocities. The corresponding flow contraction in flight is small due to the airplane forward velocity.

- Due to the difference in the contraction ratios, the turbulence originates from larger scales and therefore higher turbulence energy levels in static tests.

- Due to the difference in the contraction ratios, the streamwise integral scale is much larger in static tests. Therefore a larger amount of the turbulence energy contributes to narrowband sound in a small band centered around the BPF. In flight the streamwise integral scale is small and therefore only a fraction of the total turbulent energy contributes to narrowband sound at BPF.

- Due to the difference in contraction ratios, the streamwise turbulence component dominates the noise generation in flight, whereas the transverse component dominates in static conditions.

- Within the surface layer of a neutral atmospheric boundary layer the turbulence variances are nearly independent of height, but the integral length scales increase with altitude. At large wavenumbers this results in a decrease of the energy within a given wavenumber band with altitude. In other words, the energy associated with a turbulence scale decreases with altitude.

All these differences except the fourth one lead towards higher fan tone noise levels in static tests.

The approximate intensities of the turbulence involved in the tone noise generation can be estimated with equations (5.3.12) and (5.3.14). Based on the assumptions that $Z = Z_{REF}$ in static conditions the ratio between the turbulence intensities for flight and static conditions is

$$\frac{\left(\frac{\sigma_{1B}}{U_B}\right)_F}{\left(\frac{\sigma_{2B}}{U_B}\right)_S} = \left(\frac{Z_S}{Z_F}\right)^{1/3} \frac{\left(\frac{U_{REF}}{U_B}\right)_F \left(\frac{U_{AP}}{U_B}\right)_F^{5/6} \ell n \left(\frac{Z_{REF}}{Z_o}\right)_F}{\left(\frac{U_{REF}}{U_B}\right)_S^{1/3} \ell n \left(\frac{Z_{REF}}{Z_o}\right)_S} \qquad (5.3.16)$$

with subscripts F = flight
S = static

For the two reference conditions this ratio is

$$\frac{\left(\sigma_{1B}\right)_F}{\left(\sigma_{2B}\right)_S} = .021$$

The difference in the narrowband sound power level W at BPF between static and flight conditions is usually dominated by the change in the intensity of the turbulence involved in the tone noise generation. The power difference between the two reference conditions is

$$W = 27.3 \text{ dB}$$

This difference is representative for the changes in narrowband fan noise due to atmospheric turbulence between static and flight conditions.

The effect of the various independent variables on the sound power level are discussed in the following paragraphs. The sound power level is normalized with its value for the static reference condition.

Altitude

In flight, the intensity of the turbulence involved in tone noise generation decreases due to the increase in the integral scales and the slow decrease in the turbulent shear stresses (Figure 46). The corresponding change in the sound power level is shown in Figure 47.

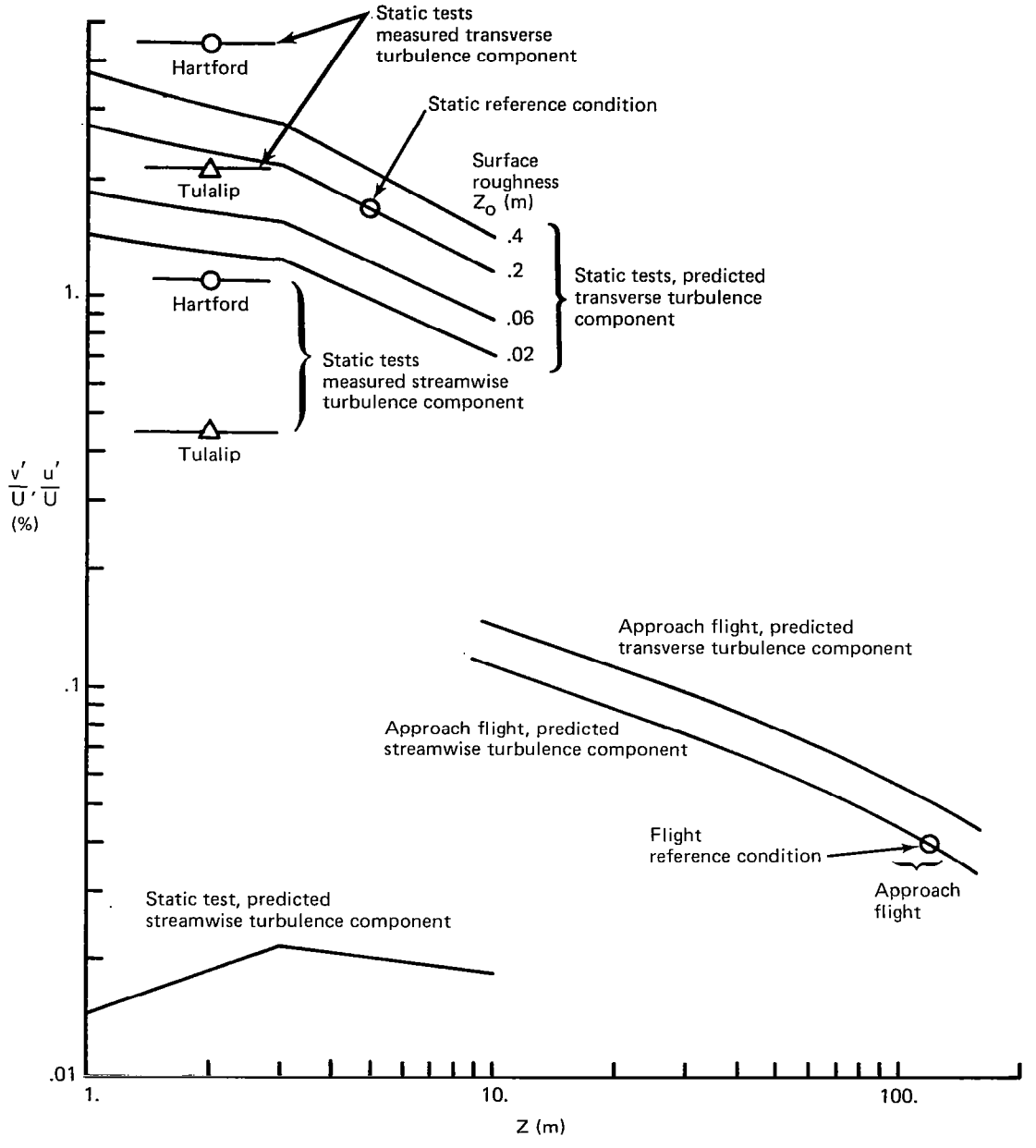

Figure 46.—Estimated Turbulence Intensities at the Fan Face Based on Scales Involved in Rotor Tone Noise Generation as a Function of Altitude Above the Ground

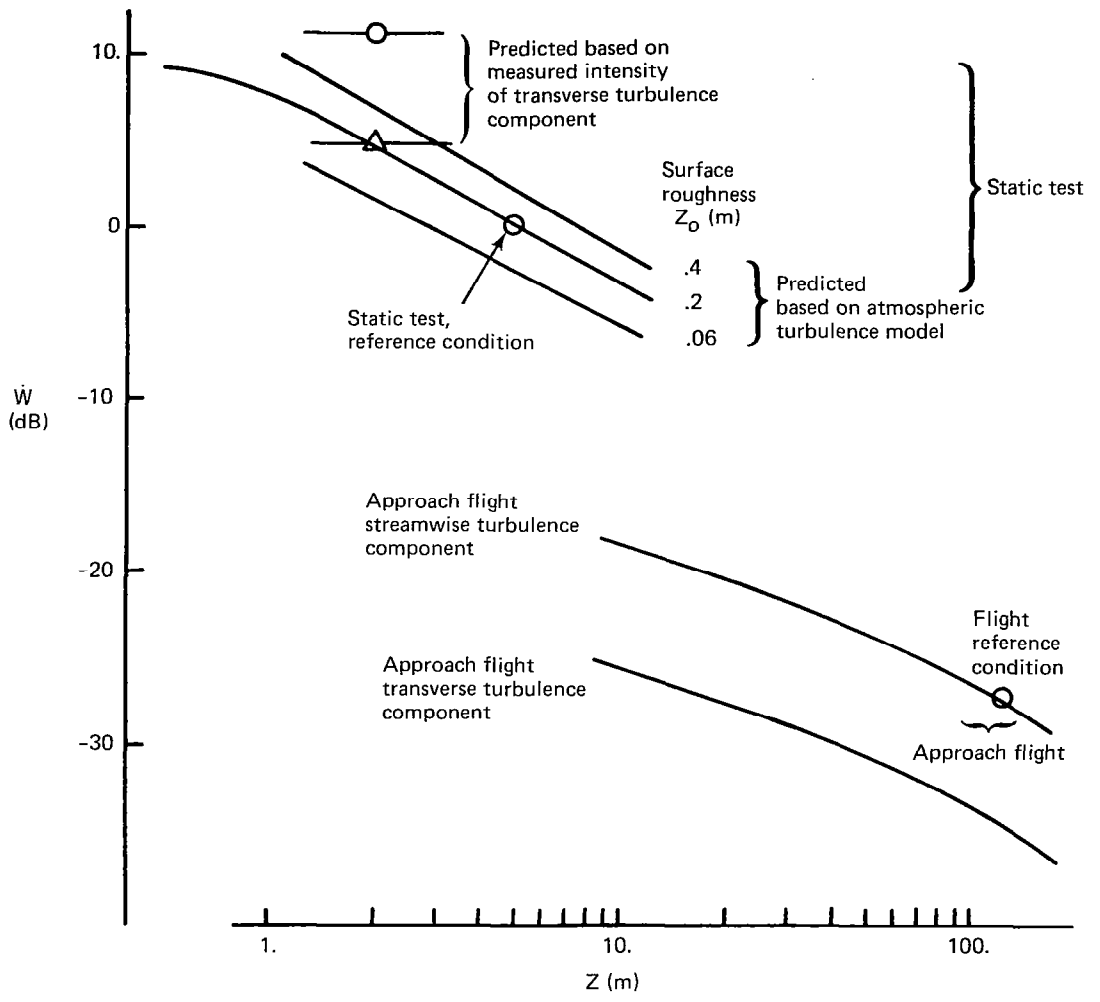

Figure 47.—Predicted Narrowband Sound Power Level W at BPF Due to Atmospheric Turbulence as a Function of Altitude Above Ground

In static conditions the decrease in the power level with altitude is even stronger. This is due to the decrease in the contraction ratio with increasing altitude. This is an indication that static test conditions can be improved by increased engine height above the ground level.

In static conditions the fan inflow field is not uniform due to the variation of the mean wind velocity with altitude, which results in a variation of the contraction ratio throughout the inflow field. This variation in the contraction ratio coupled with the variation in the turbulence properties with altitude result in a non-homogeneous turbulence field at the fan face. The models used in the present study are not sophisticated enough to evaluate such complex flow fields. But by assuming local uniformity in the mean flow field and homogenity in the turbulence field, the turbulence intensity at the fan face can be estimated for streamlines originating at different levels above the ground (Figure 46). The results indicate a significant increase in the intensity of the transverse turbulence component for flow segments originating closer to the ground. The change in the slope of the curves occurs at the point where the integral length scale of the considered scale range is equal to the integral scale of the vertical turbulence component. The corresponding sound power levels (Fig. 47) indicate increasing levels with decreasing engine axis height above the ground. In an actual static test situation with an inhomogeneous inflow field, the highest contributions to the sound pressure field are therefore expected to come from the bottom segment of the inlet. Rotor blade mounted transducer data reported by Hanson (Ref. 39) do indeed show a variation of the standard deviation of the pressure signals along the circumference of the fan face, with the highest values in the bottom segment of the inlet.

In most static test conditions, the inflow streamtube touches the ground. In that case, a stagnation point forms on the ground and along the streamline from this point the contraction ratio becomes infinite. The vorticity associated with the horizontal turbulence components, which have an intensity twice as large as the vertical component close to the ground, are very effectively amplified by the transverse contraction around such a stagnation point streamline. The contraction of the atmospheric turbulence in the flow field around such streamlines leads to a phenomena frequently referred to as a ground vortex. It is very likely that the highest turbulence intensities at the fan face occur in the vicinity of such stagnation point streamlines. The models used in this study do however not allow the prediction of the resulting intensities. Similar stagnation point situations can occur on surfaces of the test stand structure in the vicinity of the inlet.

Surface Roughness Scale

The surface roughness scale affects the mean velocity profile as well as the standard deviations of the turbulence velocity components. Its effect on the length scales of the ingested turbulence can be neglected and its effect on the intensity of the ingested turbulence as well as on the sound power can be estimated with the approximate equations (5.3.12) and (5.3.14).

$$\text{for } Z = Z_{REF} \qquad \left(\frac{\sigma_B}{U_B}\right) \sim \left[\ell n \frac{Z_{REF}}{Z_o}\right]^{-1} \qquad W \sim \left[\ell n \frac{Z_{REF}}{Z_o}\right]^{-2}$$

The ratio Z_{REF}/Z_o is usually quite large and therefore the effect of Z_o is relatively small.

In the flight condition, Z_o is reasonably well defined. Most landing approaches occur in headwinds and therefore the boundary layer evolves along the airfield. Suggested values for the roughness scale of airports range from .02 to .05 meters.

In static conditions it is more difficult to define a surface roughness scale. In most static test stand environments the surface cover changes abruptly in the vicinity of the test arena. Such a change will initiate a new internal boundary layer, a situation that exceeds the limitations of the simple atmospheric boundary layer model. Roughness elements with scales in the order of the engine height above the ground (buildings, test stands, trees, forests) are present in the vicinity of most test stands. The flow around such objects creates large scale, high intensity turbulence. The validity of the simple atmospheric boundary layer model is limited to altitudes higher than the size of the roughness elements. Usually the surface roughness varies around the test stand and therefore the mean velocity as well as the turbulence intensity change with the wind direction. These problems make it difficult to predict atmospheric turbulence in static test stand environments.

Inflow turbulence was measured at the fan face of a JT9D-7 engine during two static tests which form part of a joint P&WA and Boeing noise reduction program. The two tests were conducted at different test facilities. The turbulence was measured with split film and X-wire anemometers located at several radial positions on a rake in the bottom segment of the inlet. The statistical averages of the turbulence measured at the fan face, averaged over several conditions and all radial locations are listed in the following table.

Test site	Mean wind m/s	Sensor type	$\frac{u_1'}{U}$ %	$\frac{u_2'}{U}$ %	$\frac{L_{21}}{R_o}$	$\frac{L_{22}}{R_o}$
Hanford	3.58	Split film	1.06	4.26	45.	.17
Tulalip	.76	X wire	.44	2.06	—	—

The turbulence intensities are presented in Figure 46 together with results predicted by the analytical model for various surface roughness scales. The results indicate that the predicted and the measured turbulence intensities for the transverse component are of the same order of magnitude. An extremely large discrepancy exists however between the predicted and measured intensities of the streamwise turbulence component. This difference can be partially explained with the high noise floor in the streamwise turbulence component signal measured by the split film anemometers, which affected the higher of the two levels. It also could be due to density fluctuations in the highly anisotropic turbulence. However, many investigators have reported, that the attenuation of the streamwise turbulence component is not nearly as large as predicted by the analytical flow contraction models. Nonetheless, the separation between the two turbulence component intensities is large enough to make the transverse component the dominant one in the fan tone noise generation in static tests.

The narrowband sound power at BPF due to atmospheric turbulence in static tests has been computed based on the measured turbulence length scales and the intensities of the transverse turbulence component. The power is computed with the assumption of a homogeneous turbulence distribution. Since it is based on the turbulence characteristics measured in the bottom of the inlet, it overestimates the sound power level to be expected in static test conditions. The results are presented in Figure 47 together with the sound power levels predicted by the analytical model. The two sets of data agree reasonably well. Based on these results, it is concluded that the surface roughness scale in the test stand environment should be minimized. Large roughness elements (buildings) should be moved away from the test arena.

Mean Wind Velocity

The reference wind velocity affects the mean wind velocity as well as the standard deviations of the turbulence components. Its effect on the integral scales of the turbulence involved in the generation of narrowband fan noise is minimal. Its effect on the corresponding turbulence intensities can be estimated with equations (5.3.12) and (5.3.14).

$$\left(\frac{\sigma_{2B}}{U_B}\right)_S \sim U_{REF}^{1/3} \quad \left(\frac{\sigma_{1B}}{U_B}\right)_F \sim U_{REF}$$

The results based on the exact equations are presented in Figure 48. The corresponding sound power levels are presented in Figure 49. The results indicate that in-flight power levels increase rapidly with the mean wind velocity, but in all situations they remain substantially lower than the ones occurring in static tests. In static test conditions the effect of the mean wind velocity is less significant. But lower wind velocities provide lower turbulence intensities at the fan face and are therefore preferred in static test conditions.

Atmospheric Stability

In an atmosphere with an adiabatic lapse rate, in neutral stability, the turbulence is sustained by the shear in the mean flow. The associated energy transfer from the mean flow to the turbulence is proportional to the velocity gradient and therefore decreases with altitude. In stable or unstable conditions energy is subtracted or added to the turbulence through buoyancy forces. This energy is assumed to be invariant with altitude. The absolute value of the flux Richardson number, the ratio between the turbulence production by buoyancy and by shear increases therefore with altitude.

This is reflected in the predicted intensities for the turbulence involved in fan tone noise generation shown in Figure 50. They are based on a mean wind velocity of 4.12 m/s (8 kts) at 6.1 meters (20 ft) altitude and the range of Richardson numbers has been selected based on data presented in Reference 16, which indicate that at the selected altitude and mean wind velocity Richardson numbers smaller than –.5 have an occurrence probability of less than 10%. The same set of data indicates that the average Richardson number is

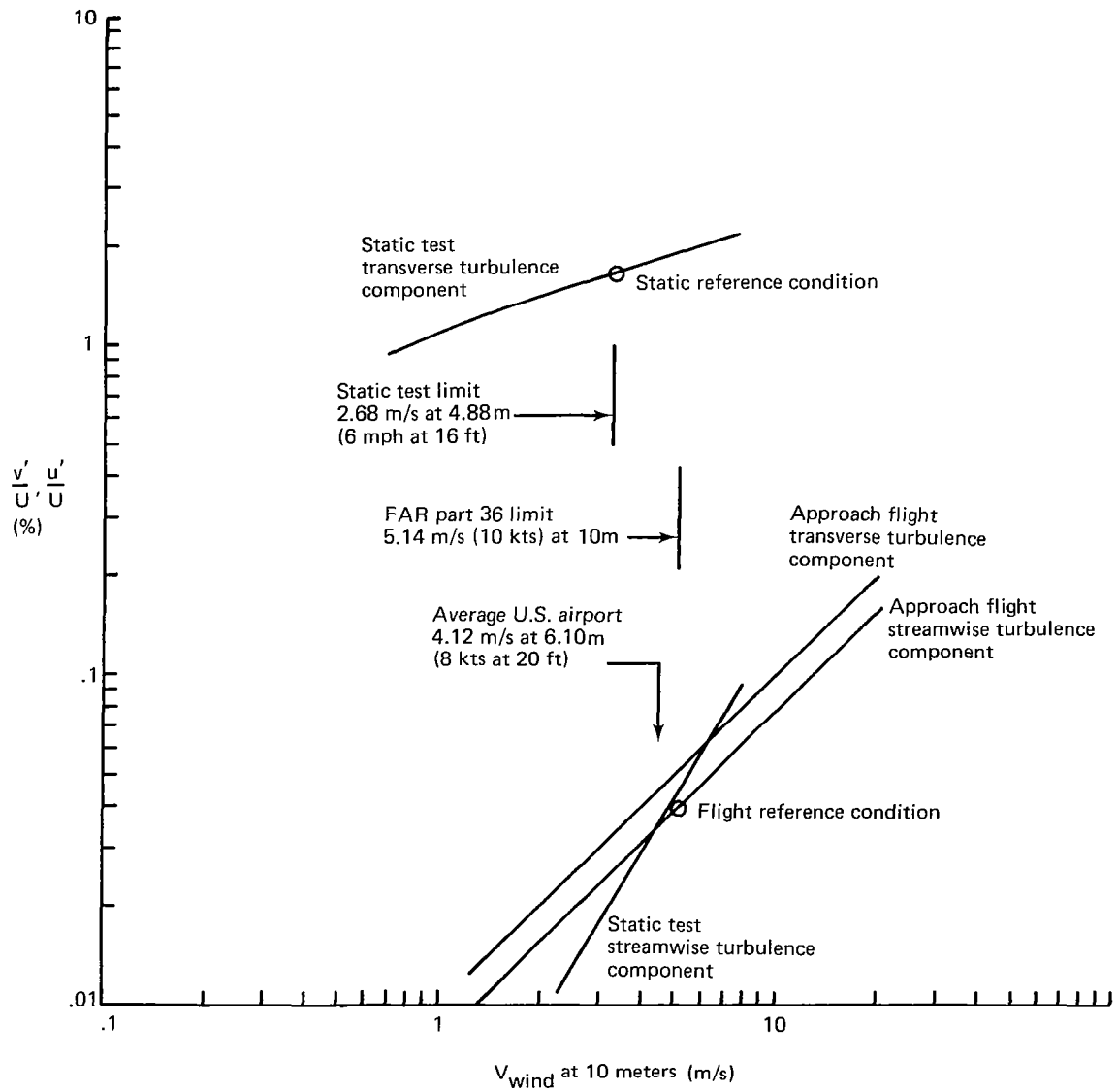

Figure 48.—Estimated Turbulence Intensities at the Fan Face Based on Scales Involved in Rotor Tone Noise Generation as a Function of the Wind Velocity at 10 Meters Above the Ground

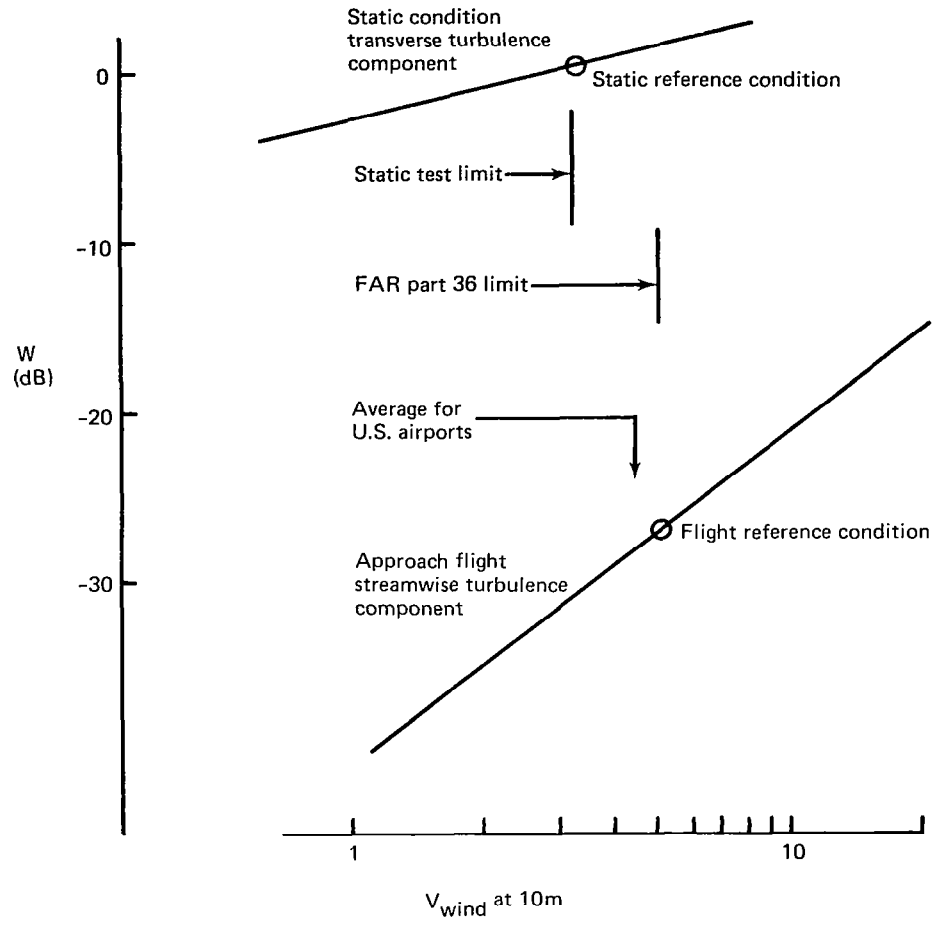

Figure 49.—Predicted Narrowband Sound Power Level W at BPF Due to Atmospheric Turbulence as a Function of the Wind Velocity at 10 Meters

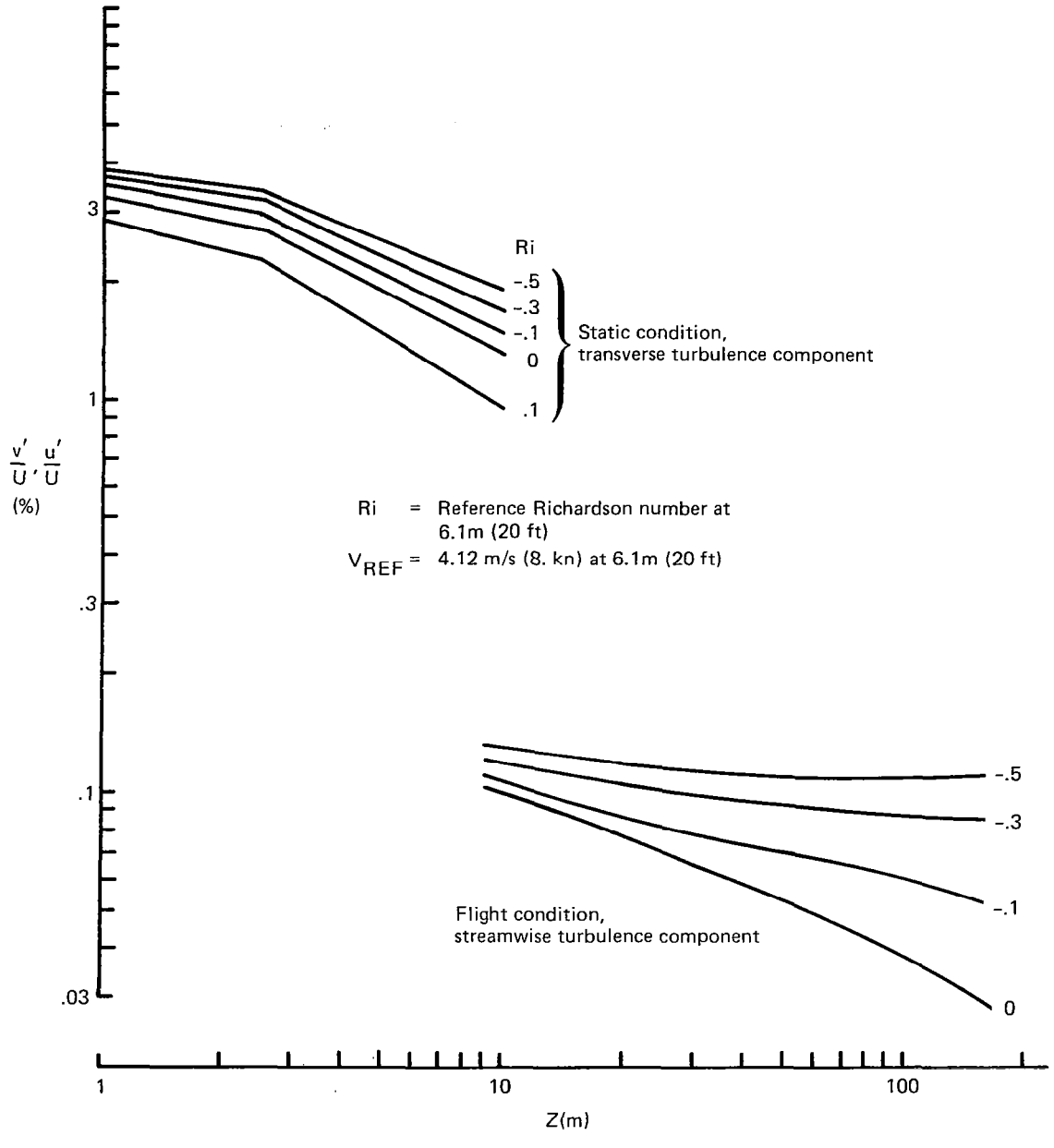

Figure 50.—Estimated Turbulence Intensities at the Fan Face Based on Scales Involved in Tone Noise Generation as a Function of Altitude and Atmospheric Stability

slightly positive. The results shown in Figure 50 demonstrate the negligible effect of thermal stability on the static conditions and its substantial effect on the flight conditions. The corresponding sound power levels are presented in Figure 51. The gap between static and flight conditions is substantially reduced in unstable conditions, but is still in the order of 20 to 25 dB.

Airplane Mach Number

The analytical model has been used to estimate the effects of airplane forward velocity on the ingested turbulence as well as on the associated fan narrowband sound power at BPF.

With increasing forward velocity, the inflow contraction ratio is reduced and therefore the contraction effects on the turbulence decrease. At the same time the size of the inflow streamtube is reduced which in turn reduces the scale and therefore the energy of the pre-contraction turbulence. The resulting intensities for the turbulence involved in the fan narrowband noise generation are presented in Figure 52. They are based on the size and location of a JT9D engine installed in a 747 aircraft. The reference wind velocity was assumed 2.68 m/s (6 MPH) at 4.88 meters (16 ft). The results are based on the conditions along a streamline that enters the fan horizontally at engine axis height. They demonstrate the significant reduction in the intensity of the transverse turbulence component during the initial phase of the ground roll ($M_{ap} < .05$). They also show insignificant changes for the range of aircraft velocities during landing approach. The corresponding narrowband sound power levels at BPF are shown in Figure 53. They demonstrate the significant sound power reduction (20 dB) during the initial aircraft acceleration to a Mach number of .05 and the negligible changes over the range of airplane approach velocities. Significant improvements in the fan inflow field can therefore be achieved even at small vehicle velocities ($M_{ap} > .05$).

Fan Size

In the evaluation of fan tone noise due to atmospheric turbulence of different scale fans, the results cannot simply be scaled. This is due to the fact that several significant scales affect the results, the fan radius, the surface roughness scale, the test stand height, the flight path altitude, and the thickness of the atmospheric boundary layer. According to the models used in the prediction of the narrowband sound due to atmospheric turbulence, the acoustic results are primarily a function of the integral scales and the intensities of the turbulence at the fan face. For most conditions, a given engine height and contraction ratio, the model predicts that the integral length scales are proportional to the fan rotor radius. Therefore, the non-dimensionalized integral scales are independent of fan rotor scale. Based on this result the sound power could be scaled with the square of the rotor radius. However, according to equations (5.3.12) and (5.3.14) the turbulence intensities are a function of the fan rotor radius R_o.

$$\left(\frac{\sigma_{2B}}{U_B}\right)_S \sim R_o^{1/3} \qquad \left(\frac{\sigma_{1B}}{U_B}\right)_F \sim R_o^{1/3}$$

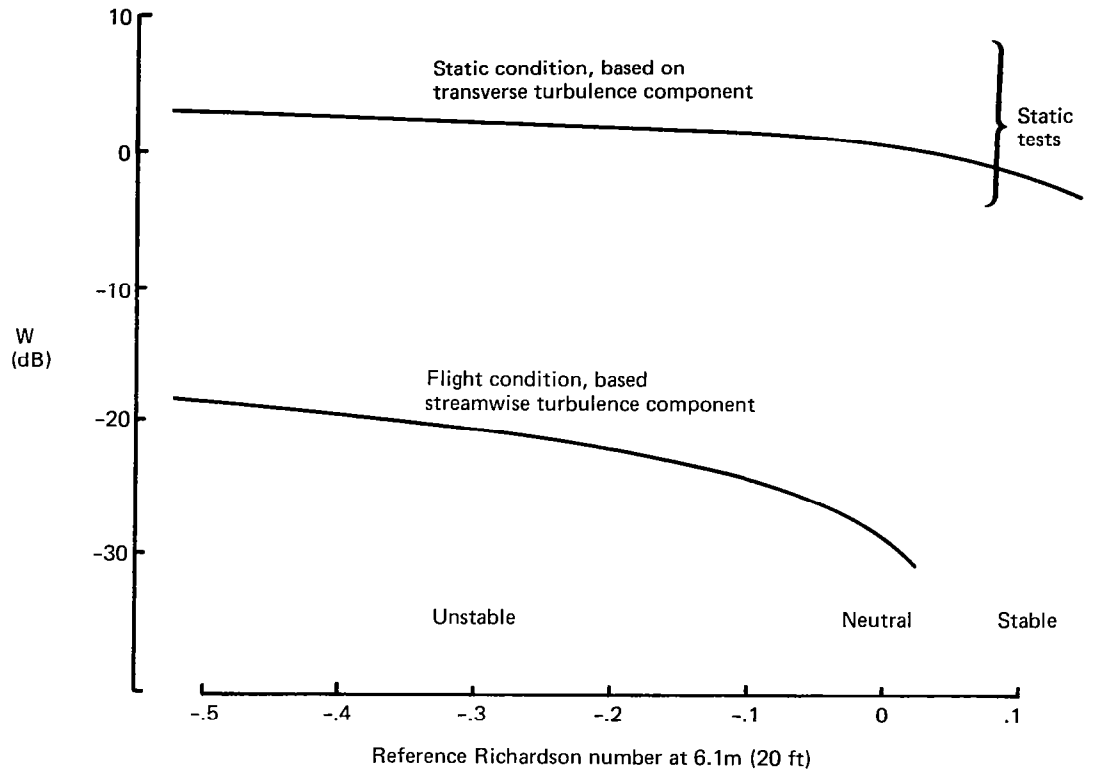

Figure 51.—Predicted Narrowband Sound Power Level W at BPF Due to Atmospheric Turbulence as a Function of Atmospheric Stability

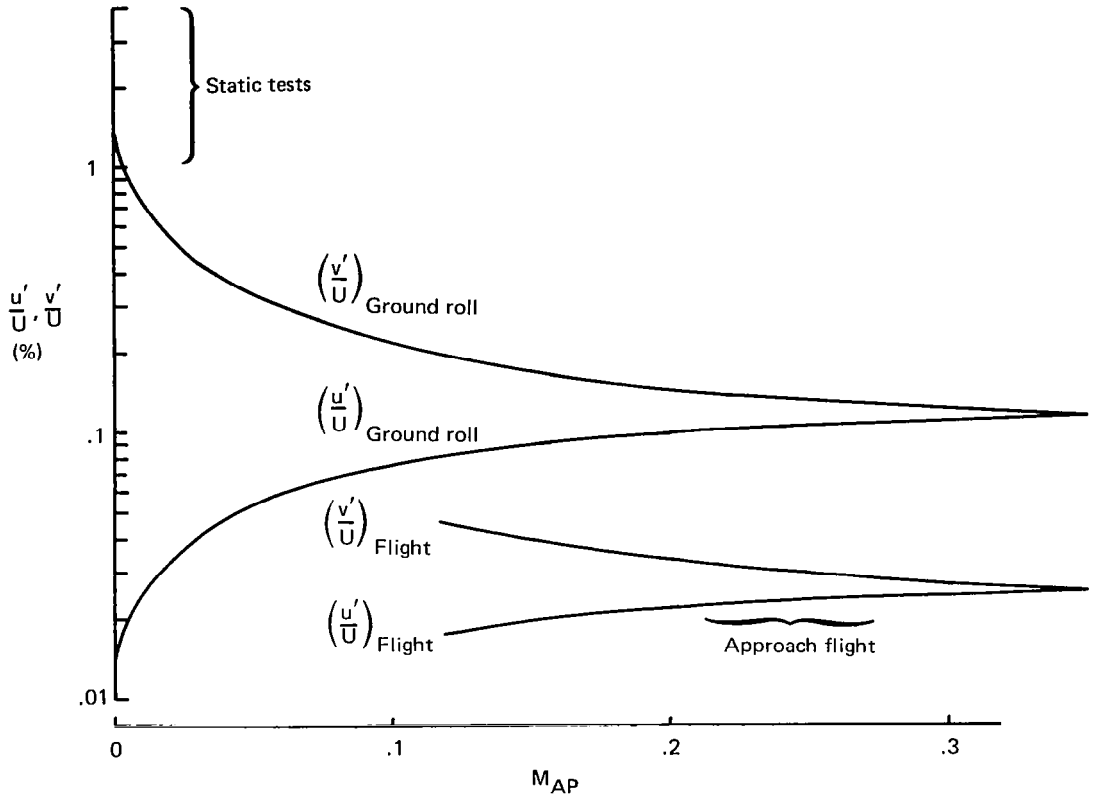

Figure 52.—Estimated Turbulence Intensities at the Fan Face Based on Scales Involved in Fan Tone Noise Generation as a Function of Airplane Mach Number M_{AP}

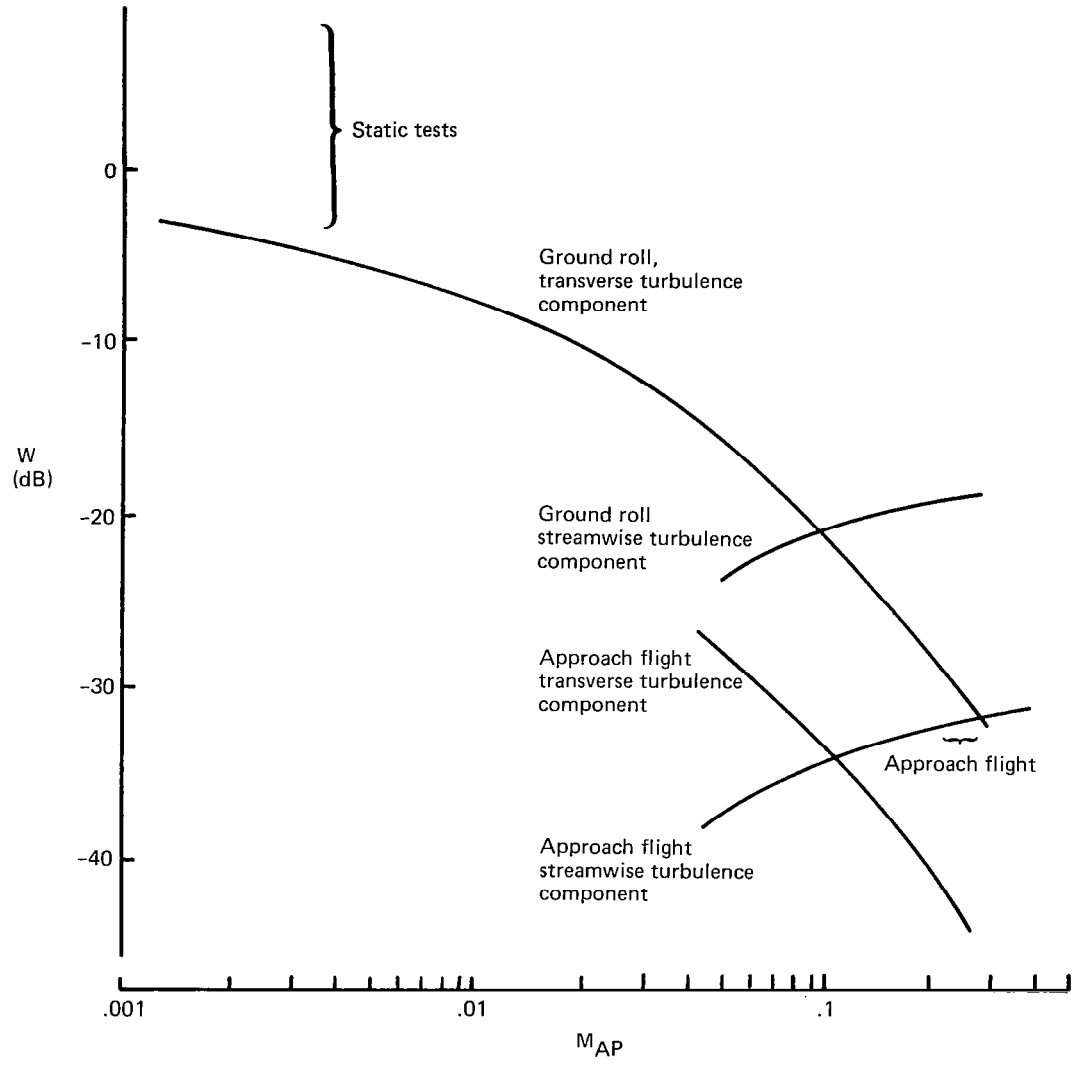

Figure 53.—Predicted Narrowband Sound Power Level W at BPF Due to Atmospheric Turbulence as a Function of Airplane Mach Number M_{AP}

The predicted turbulence intensities shown in Figure 54 reflect this simple relationship.

The sound power due to atmospheric turbulence convected through a rotor is proportional to the (8/3) power of the fan rotor radius (Fig. 55). In a first-order approximation the difference in rotor tone noise between static and flight conditions seems to be independent of fan rotor size. Since the sound power due to atmospheric turbulence is proportional to the (8/3) power of the rotor scale, it becomes more dominant with respect to other fan tone noise sources with increasing fan scale. This change in the separation relative to other sources is in the order of 4 dB between the JT9D (R_o = 1.18 m) and the JT15D (R_o = .27 m).

Rotor Blade Spacing

Results presented in Section 5.2.2 indicate that changes in the fan tone sound power level with the number of rotor blades, or in other words with the rotor blade spacing, are minimal for transverse integral scales larger than 3% of the rotor radius. Measured as well as predicted transverse integral scales are considerably larger. The predicted results shown in Figure 55 demonstrate the relatively small effect of the rotor blade number. The level differences apparent in the results for the approach flight condition are primarily due to the change in the bandwidth which has been assumed proportional to the blade passing frequency.

Figure 55 also includes predictions for the JT9D and JT15D engines. For both engines the static to flight differences in rotor tone noise due to atmospheric turbulence are predicted to be in the order of 30 dB.

Fan Tip Mach Number

In Section 5.2.2 it has been shown that for constant turbulence intensity and scales, the fan tone noise power due to convected turbulence increases proportionally with the fourth to seventh power of the fan tip Mach number. Based on equations (5.3.12) and (5.3.14) the effect of the axial Mach number at the fan face on the turbulence intensities is

$$\left(\frac{\sigma_{2B}}{U_B}\right)_S \sim U_B^{-1/3} \qquad \left(\frac{\sigma_{1B}}{U_B}\right)_F \sim U_B^{-11/6}$$

In both conditions the turbulence intensity is reduced with increasing fan face velocity and therefore with the fan tip Mach number. This reduces the exponent in the relationship between fan tone sound power and fan tip Mach number by 2/3 in the static condition and 11/3 in the flight condition. Within the approach power range the difference in rotor tone noise due to atmospheric turbulence between static and flight conditions is expected to increase with fan tip Mach number.

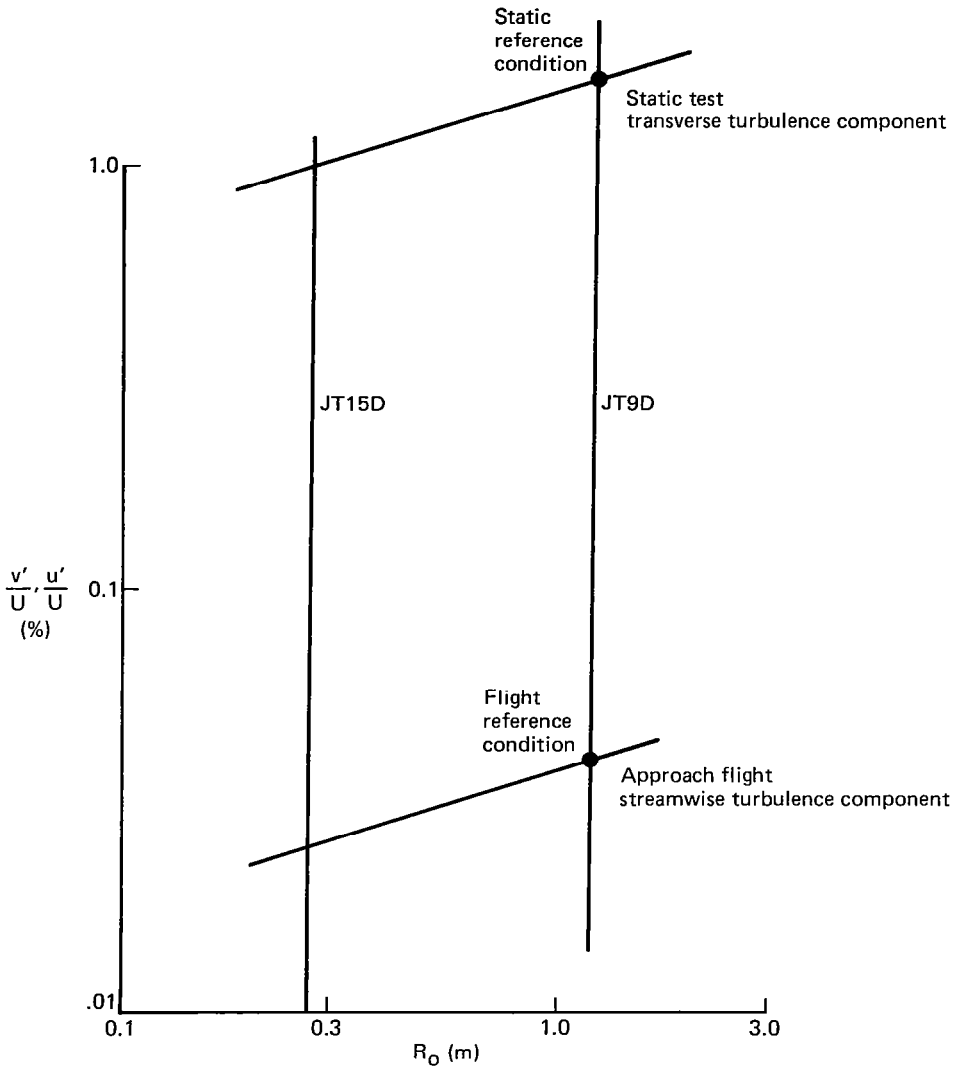

Figure 54.—Estimated Turbulence Intensity at the Fan Face Based on Scales Involved in Tone Noise Generation as a Function of the Fan Radius R_o

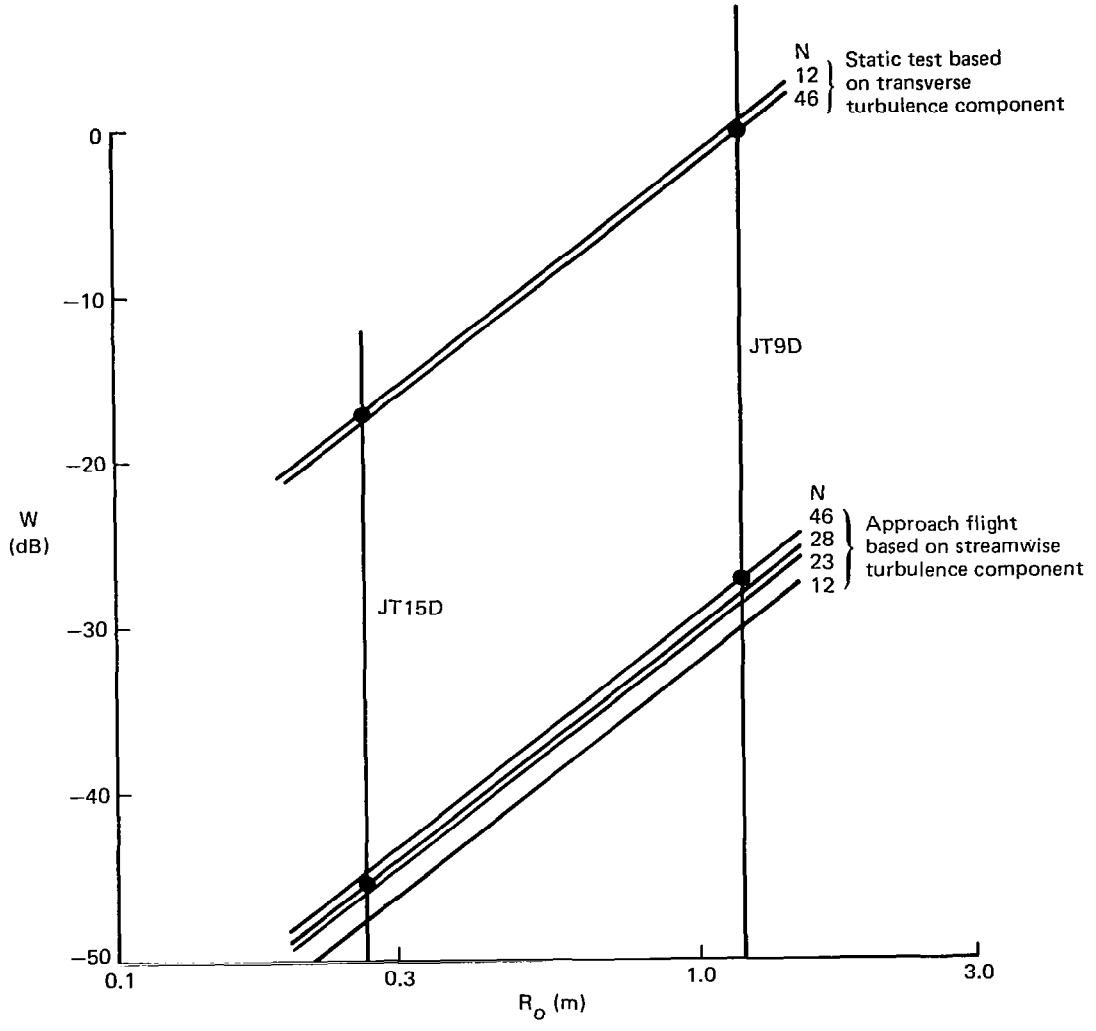

Figure 55.—Narrow Band Sound Power at BPF Due to Atmospheric Turbulence as a Function of Fan Rotor Radius R_o and Number of Rotor Blades N

6.0 INLET ANGLE OF ATTACK EFFECTS ON FAN NOISE

6.1 BACKGROUND

The flow field in an inlet operated at an angle of attack is asymmetric. The mean flow velocity, as well as the boundary layer, vary circumferentially throughout the inlet. The resulting circumferential distortions in the flow field at the fan face may affect the sound pressure field emitted by the fan. The more significant distortions in the vicinity of the inlet surface between the highlight and the throat plane may affect the sound propagation from the fan to the far field. In connection with the improvement of test methods for static fan noise tests, it is necessary to know the significance of the acoustic effects resulting from inlet angle of attack induced flow distortions. If these effects are significant, an attempt to simulate them in static conditions might be necessary.

References 12 and 13 report fan noise results from wind tunnel tests concerned with angle of attack effects. The results indicate that inlet operation at an angle of attack will affect the directivity and possibly the sound power generated by a fan. Results from an in-flight investigation of fan noise reported in Reference 3 indicate that the inlet angle of attack might have an effect on fan tone noise at the blade passing frequency and its harmonics. During a joint flight test conducted by P&WA and Boeing, a limited amount of information concerned with the inlet angle of attack effects on fan noise has been acquired. It is the purpose of this section to describe the results of this investigation.

6.2 TEST DESCRIPTION AND INSTRUMENTATION

The inlet angle of attack effects on fan noise were investigated during a flight test, which formed part of a joint P&WA and Boeing Noise Reduction Program. The test was conducted in Seattle with a 747 aircraft powered by JT9D-7 engines with hardwall nacelles. One of the inboard engines was extensively instrumented with static pressure sensors, rotor blade mounted transducers and inlet and fan duct microphones. In addition to the standard test instrumentation, the airplane was equipped with fuselage-mounted microphones and split film anemometers in various locations. The investigation of the inlet angle of attack effects is based on aircraft and engine mounted instrumentation only and the evaluation is limited to the sound pressure field of the instrumented, inboard engine. In order to minimize the effects of parameters other than the inlet angle of attack on the data, the corrected fan speed of the inboard engines was kept constant and changes in the aircraft velocity were kept to a minimum. The inlet angle of attack changes were obtained by variation of flap settings, outboard engine power settings and landing gear position. The investigation is limited to two typical power settings for approach and takeoff. The conditions are summarized in the following table.

Condition	Flaps	Landing gear	Airspeed	Inboard engine $N1\sqrt{\theta_{t2}}$	Inlet angle of attack
–	deg	–	m/s	RPM	deg
1	5	down	90.	3310.	17.5
2	10	up	90.	3300.	15.5
3	20	up	91.	3330.	11.5
4	25	up	104.	3350.	5.5
5	10	up	90.	2425.	15.5
6	20	up	88.	2420.	12.5
7	25	up	89.	2415.	10.5
8	25	up	104.	2425.	5.5

During normal takeoff and landing maneuvers the inlet angle of attack varies between 7 and 15 degrees. The range of angles evaluated during this test therefore covers the normal operating conditions.

The following instrumentation has been used in the evaluation of the angle of attack effects.

Static Pressure Sensors

Static pressure ports were located in two planes, upstream and downstream of the fan rotor (Fig. 56). The upstream location was separated 9 cm from the fan leading edge and the downstream position was 15 cm from the trailing edge. Each plane contained 12 equispaced pressure ports. Each pressure was measured by an individual pressure sensor and the signals were sampled at a rate of 2.5 times per second. The purpose of these measurements was to determine the mean flow distortions at the fan face and to observe changes in the static pressure distribution downstream of the fan rotor.

Rotor Blade Mounted Pressure Transducers (BMT)

Thin film dynamic pressure transducers were mounted on several rotor blades. The diaphragm of these sensors is about 1 mm in diameter and the frequency response extends to above 20 KHz. The transducers were bonded to the pressure side of the blades at various radial locations close to the blade leading edge (Fig. 58). The transducer lead wires were run along the blade pressure surface to the blade hub and into the nose cone, where they were connected to the rotating telemetry system. The signal emitted by the telemetry transmitter was picked up by an antenna embedded in the surface of the inlet. From there the signal was carried by fixed wiring to a bank of FM receivers, where the signals were separated and passed to the proper recording channels. The purpose of these dynamic pressure measurements was to detect changes in the steady and unsteady velocity distortions at the fan face.

Inlet and Fan Duct Dynamic Pressure Transducers

Dynamic pressure transducers were mounted at various locations in the inlet as well as in the fan duct (Figs. 61 and 64). These sensors were used to evaluate changes in the fan sound pressure field due to the variation of the inlet angle of attack.

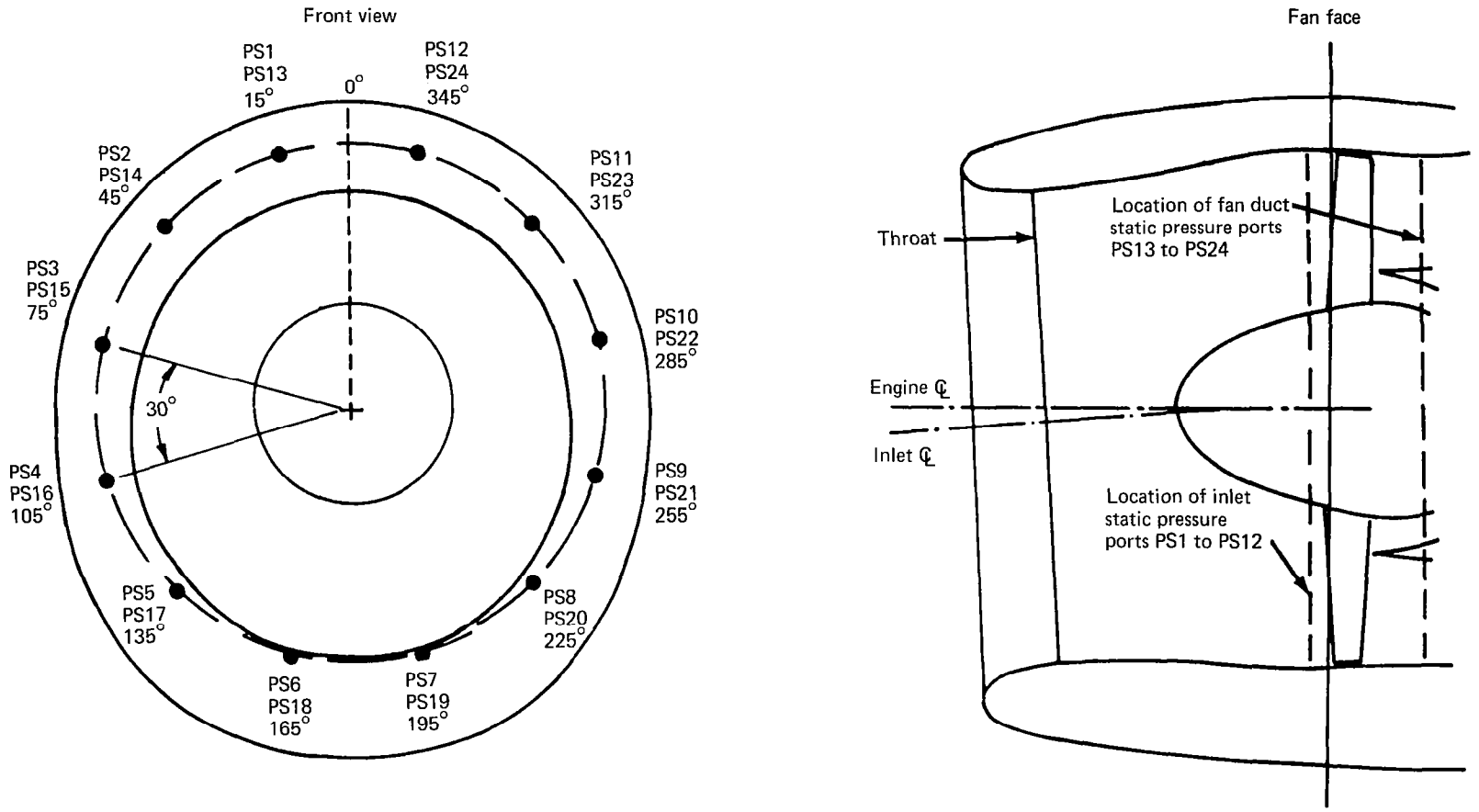

Figure 56.—Static Pressure Port Locations

Fuselage Mounted Microphones

Twelve .5 inch condensor microphones were mounted in window panes of the test aircraft (Fig. 67). They were used to monitor changes in the far field sound pressure distribution that could be associated with inlet angle of attack changes.

All dynamic signals were recorded on tape at 76.2 cm/s. The results presented in the next paragraph are based on post test narrowband analysis of these records and represent averages for signals of 35 seconds duration.

6.3 RESULTS

The results from this test can, at best, provide a partial assessment of the inlet angle of attack effects on fan noise. The mean flow field in an inlet operated at an angle of attack is circumferentially distorted. The highest velocity distortions occur in the area between the highlight and the throat close to the inlet surface. As a result of these distortions in the mean flow field corresponding distortions in the propagation must be expected, and this may lead to a distortion in the far field acoustic pressures. Very likely such propagation distortions cannot be observed with the fuselage mounted microphones. The results of this test will therefore at best, provide an assessment of the inlet angle of attack effects on the fan noise at its source.

Static Pressure Sensors

The circumferential variation of the static pressure at the inlet surface upstream of the fan is shown in Figure 57. The static pressure distortion increases with the angle of attack at both power settings. The results show a decrease in the static pressures in the bottom of the inlet. Results from an earlier flight test show that outside of the thin boundary layer the total pressure variations along the inlet circumference are considerably smaller than the corresponding static pressure variations. Based on this information, it is concluded that the low static pressures in the bottom of the inlet represent a high velocity region. This positive streamwise velocity distortion increases with the inlet angle of attack.

The static pressure distribution downstream of the fan is difficult to interpret without the knowledge of the corresponding total pressure distribution. It therefore, is omitted in the discussion of the inlet angle of attack effects.

Blade Mounted Transducers

The results are based on four transducers located on the same blade at different radial locations (Fig. 58). A typical power spectrum of a blade mounted transducer signal is shown in Figure 59. The narrow spikes in this spectrum represent the periodic pressure fluctuations on the fan blades that result from steady or quasi-steady distortions in the fan inflow field. Figure 60 presents the five lowest harmonics of the BMT signals as a function of the inlet angle of attack for the four transducers. The data indicate an angle of attack related increase in the power of the two lowest harmonics. This increase is greatest at the edge of the boundary layer and becomes smaller towards the hub. Changes in the

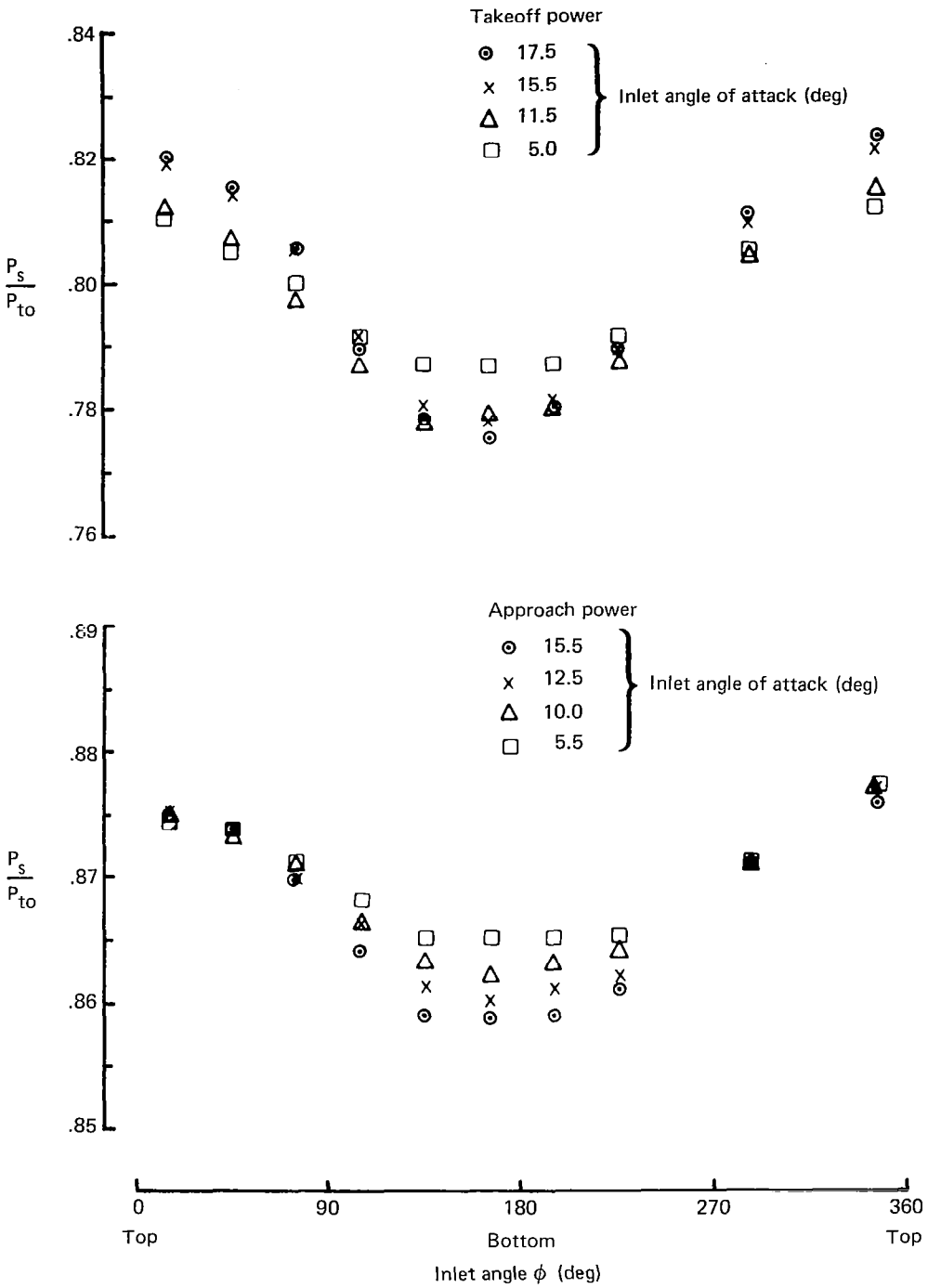

Figure 57.—Circumferential Variation of the Static Pressure at the Inlet Surface Upstream of the Fan

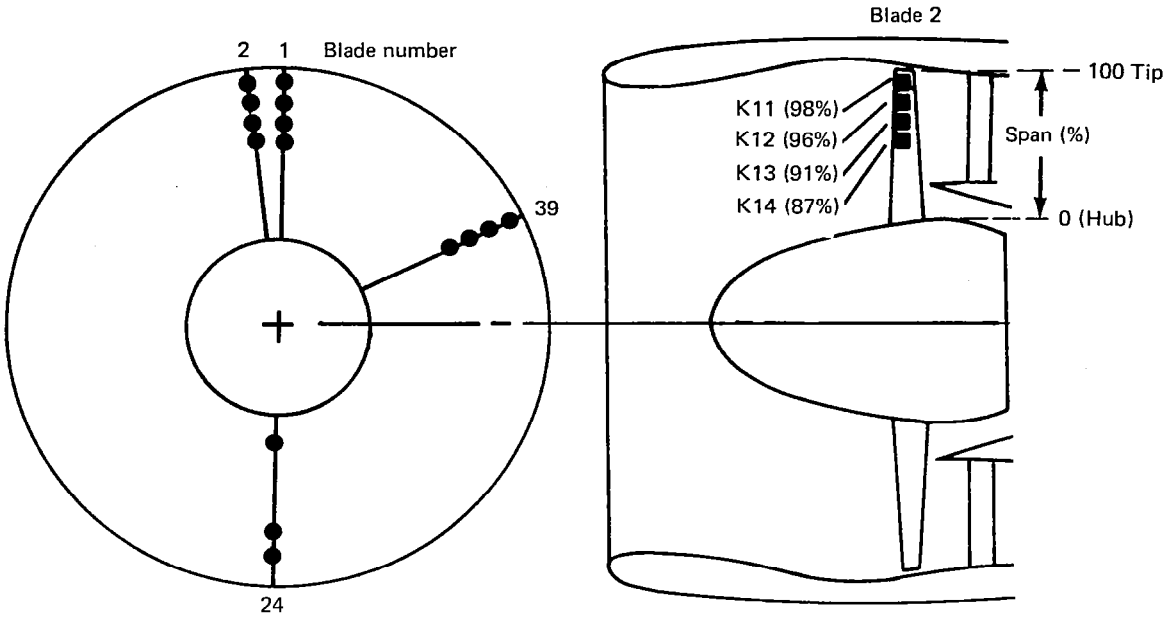

Figure 58.—Location of Rotor Blade Mounted Transducers

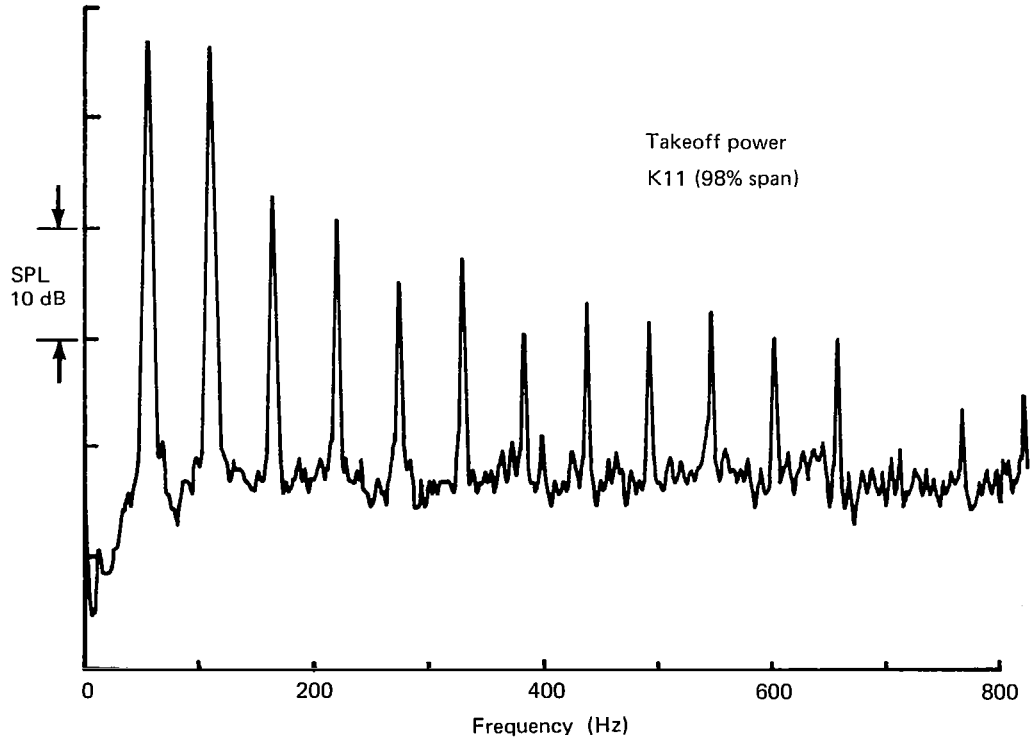

Figure 59.—Typical Blade Mounted Transducer Spectrum

higher order harmonics do not seem to be related to angle of attack effects. The distortion represented by the changes in the two lowest harmonics has a circumferential scale in the order of one-half of the circumference and a radial scale in the order of 10% of the blade span. Such a distortion is either due to the inlet boundary layer or the rotor tip flow. Based on the BMT and static pressure data combined, it is concluded that a positive streamwise velocity distortion exists close to the inlet surface in the bottom of the inlet. It covers the inlet boundary layer as well as part of the mean flow and increases in intensity with the inlet angle of attack. At takeoff power an opposite trend is apparent in the top of the inlet. These phenomena cannot be explained as inlet boundary layer effects and it is suggested that they are due to changes in the rotor blade tip flow. They could result from a change in the circumferential distribution of the rotor tip clearance brought about by the asymmetric aerodynamic load distribution on the inlet nacelle and the oval shape of the rotor rub strip. Relative motion between the fan axis and the fan case under asymmetric aerodynamic loads has been observed previously (Ref. 14).

Inlet and Fan Duct Microphones

The inlet and the fan duct sound pressure fields were evaluated with flush mounted surface transducers only. The recorded data therefore represent only the surface pressure fluctuations and their significance in the evaluation of the total sound pressure field should not be overestimated.

Changes in the broadband noise levels in the inlet as well as in the fan duct were in general less than ±1. dB and could not be related to angle of attack changes. This was the case for both power settings and the full range of angles of attack. The sound pressure levels at the blade passing frequency and its harmonics exhibited large variations between the different angle of attack conditions. A typical set of data for the second harmonic at approach power in the inlet is presented in Figure 62. This set of data demonstrates the seemingly random scatter that does not show any correlation with the inlet angle of attack changes. It also shows the large spatial variations in the inlet sound pressure field measured by the six coplanar sensors located close to the inlet throat. Such variations result from the interference of modes of different spinning order. The scatter in the data could be due to changes in the interference pattern between the sound pressure field resulting from the angle of attack related distortions and the sound pressure field resulting from a different source. It also could be due to the unintentional variation of a parameter other than the angle of attack that significantly affects fan tone noise. Experimental data from static tests with inflow control structures have demonstrated large, rapid variations in the narrowband sound pressure levels with fan rotational speed. It is assumed that small differences as well as fluctuations in the fan rotational speed have contributed to the scatter in the data.

Average narrowband sound pressure levels based on the seven transducers in the fan duct and on the six inlet transducers close to the throat are presented in Figures 63 and 65. The spatial averaging has eliminated a large portion of the total variation in the signals. The variations over the full range of angles of attack is less than 2 dB for most signals, and no correlation between the average sound pressure levels and inlet angle of attack is apparent.

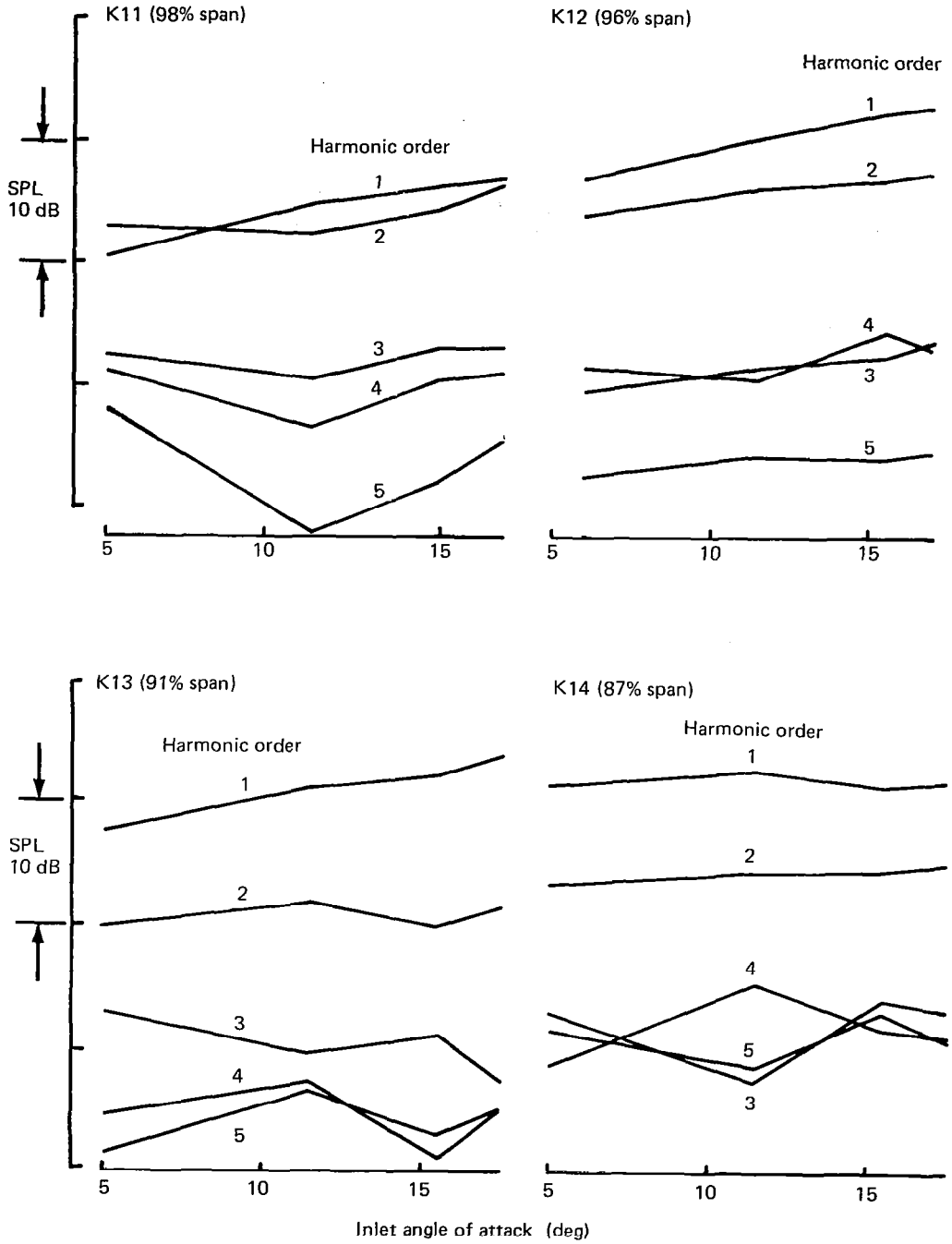

Figure 60.—Blade Mounted Transducers, Spectrum Levels of the Five Lowest Distortion Orders for Sensors at Various Radial Locations

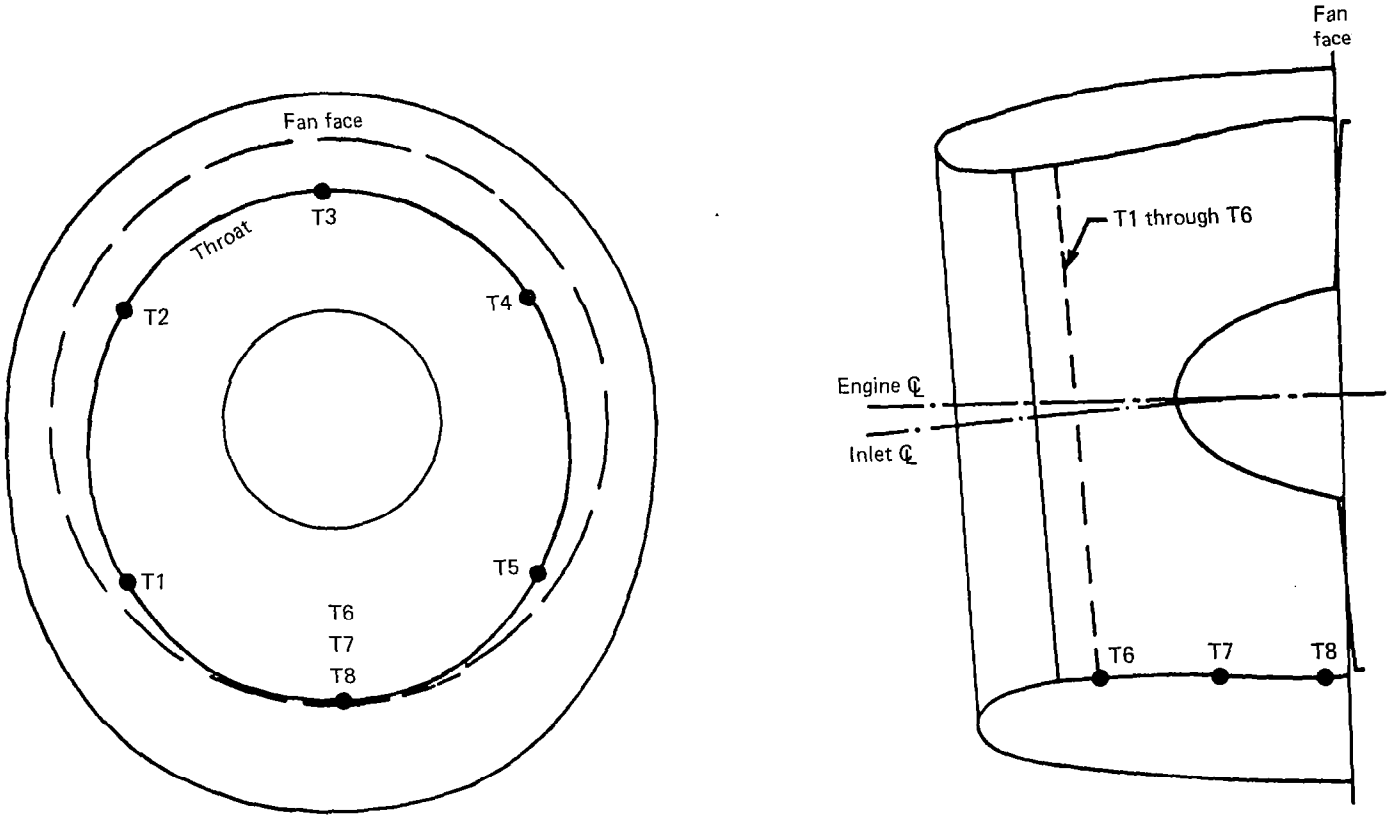

Figure 61.—Location of Inlet Pressure Transducers

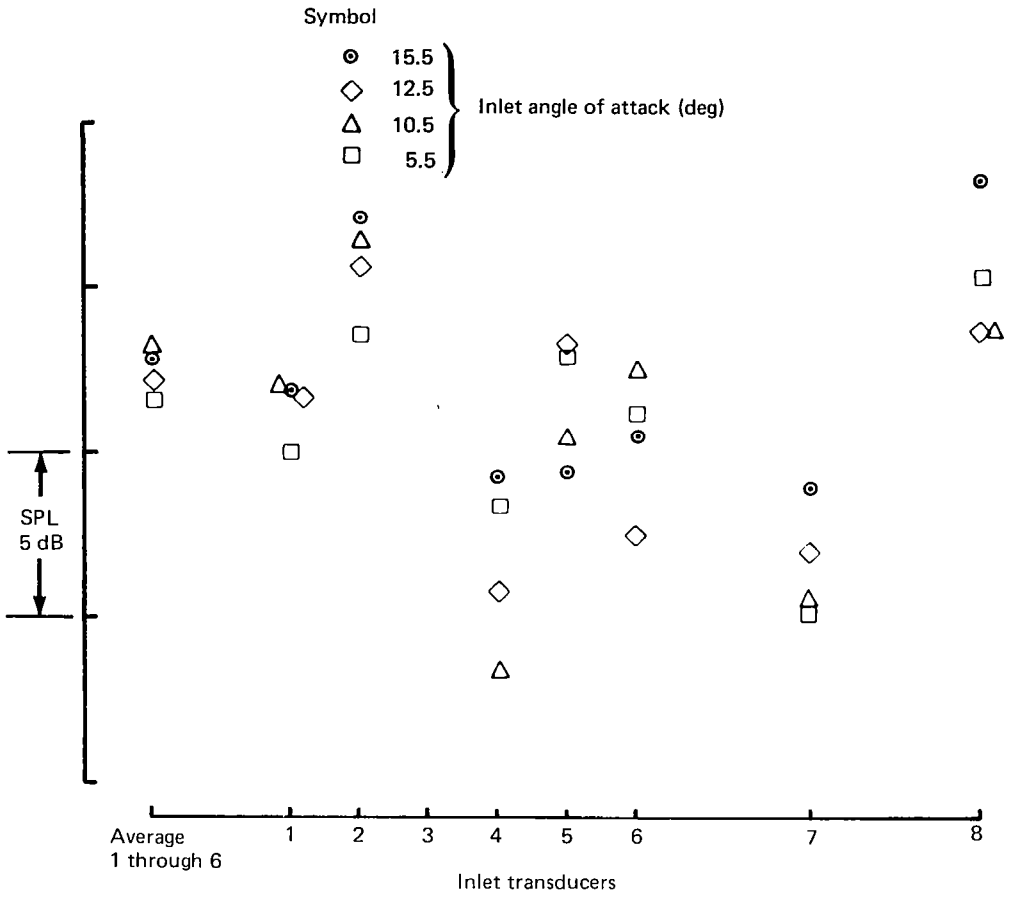

Figure 62.—Sound Pressure Level for Second Harmonic of Blade Passing Frequency in the Inlet at Approach Power

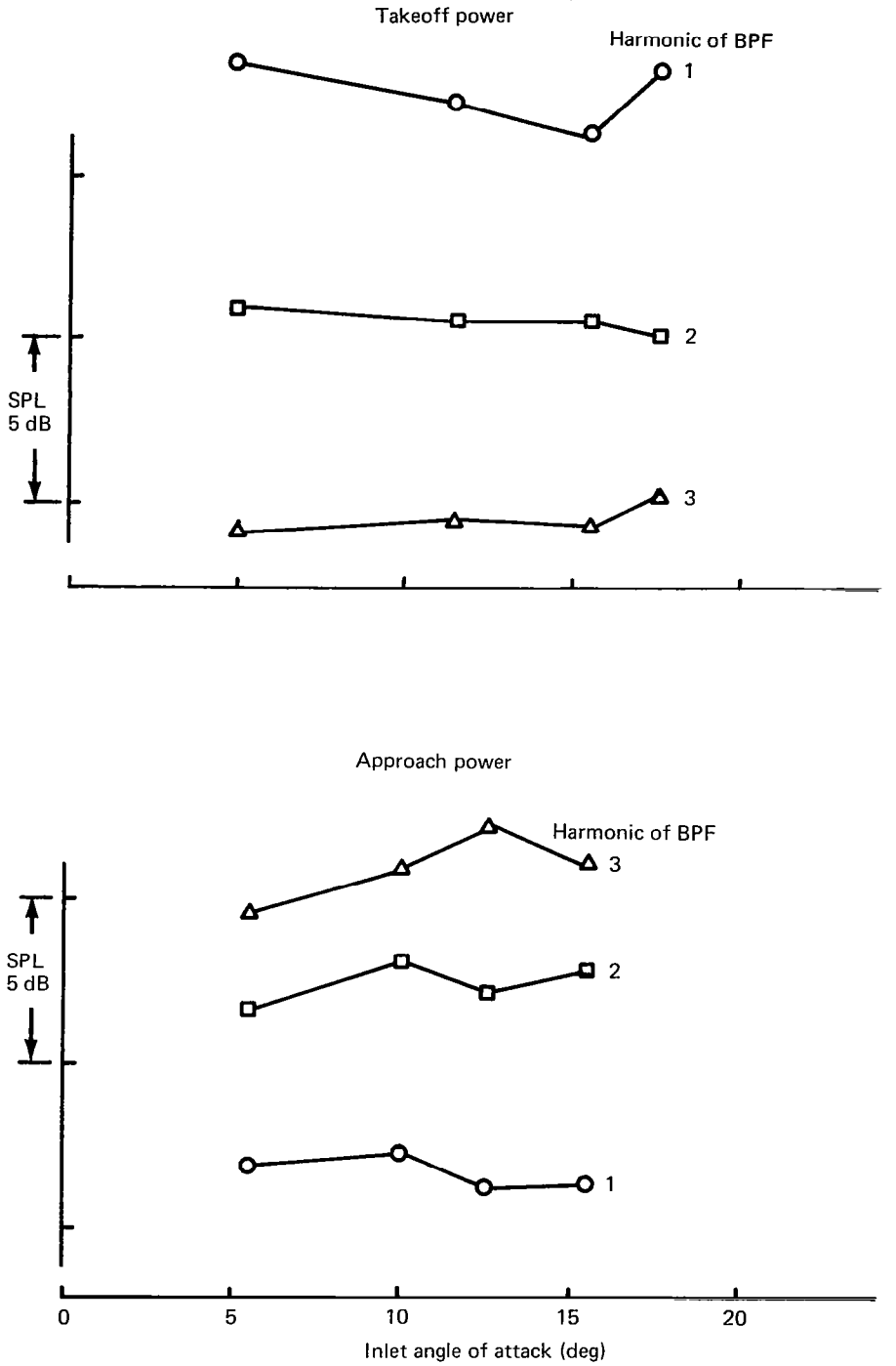

Figure 63.—Average Sound Pressure Levels Based on Six Locations Near the Inlet Throat for Harmonics of the Blade Passing Frequency

An interesting phenomenon was observed at takeoff power in the inlet sound pressure field. At small angles of attack, the buzzsaw spectrum is nearly the same at all circumferential locations. But with increasing angle of attack, the differences between the spectra in the bottom and in the top of the inlet become larger. This is demonstrated by the spectra shown in Figure 66. They represent the sound pressure signals of the sensors in the top and in the bottom of the inlet at the smallest and the largest angle of attack condition. At the intermediate locations, on the side of the inlet as well as for the intermediate angle of attack conditions, the spectra fall between the extremes. Similar changes in the buzzsaw spectra are also observed at the intermediate axial location, between the throat and the fan face. Based on this observation, it has been concluded that the asymmetry in the buzzsaw noise develops in the vicinity of the fan and is not due to velocity distortions in the throat area. It is very likely that this asymmetry is the result of the mean flow distortions in the vicinity of the fan face observed with the static pressure sensors and the blade-mounted transducers.

Fuselage Mounted Microphones

The signals of the fuselage mounted microphones represent the pressure fluctuations due to several different sources: inboard and outboard engine noise, fuselage boundary layer noise, landing gear and other aerodynamic noise. The broadband noise floor below 5 KHz is dominated by fuselage boundary layer, landing gear and other aerodynamic noise. For this reason the evaluation of the inboard engine noise field had to be limited to narrowband tones. A typical set of data representing the second harmonic of the blade passing frequency at approach power is shown in Figure 68. These data reflect the same scatter problem that was observed in the inlet and fan duct pressure signals. No attempt has been made to find correlations between the changes in the sound pressure level and the inlet angle of attack variations.

The main results based on this limited investigation are:

- The most significant changes in the flow field at the fan face associated with changes in the inlet angle of attack are very likely due to a change in the rotor blade tip flow, rather than a change in the inlet boundary layer.

- An asymmetry in the buzzsaw sound pressure field that increases with the inlet angle of attack has been observed.

- The effects of inlet angle of attack on broadband noise as well as narrowband sound at the blade passage frequency and its second harmonic seem to be in the order of 2 dB or less for the sound pressure field at the inlet and fan duct surfaces.

All conclusions apply only to angles of attack conditions representative of CTOL, subsonic aircraft operating conditions.

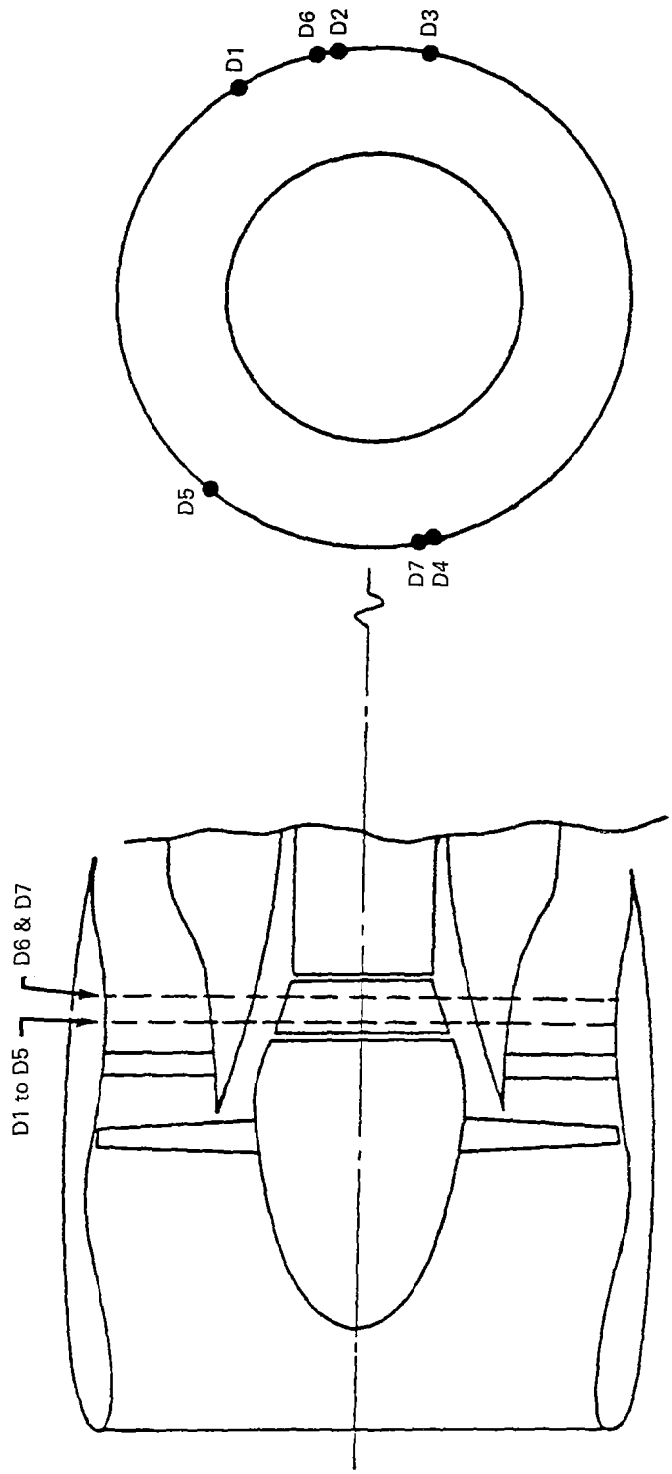

Figure 64.–Fan Duct Pressure Transducer Locations

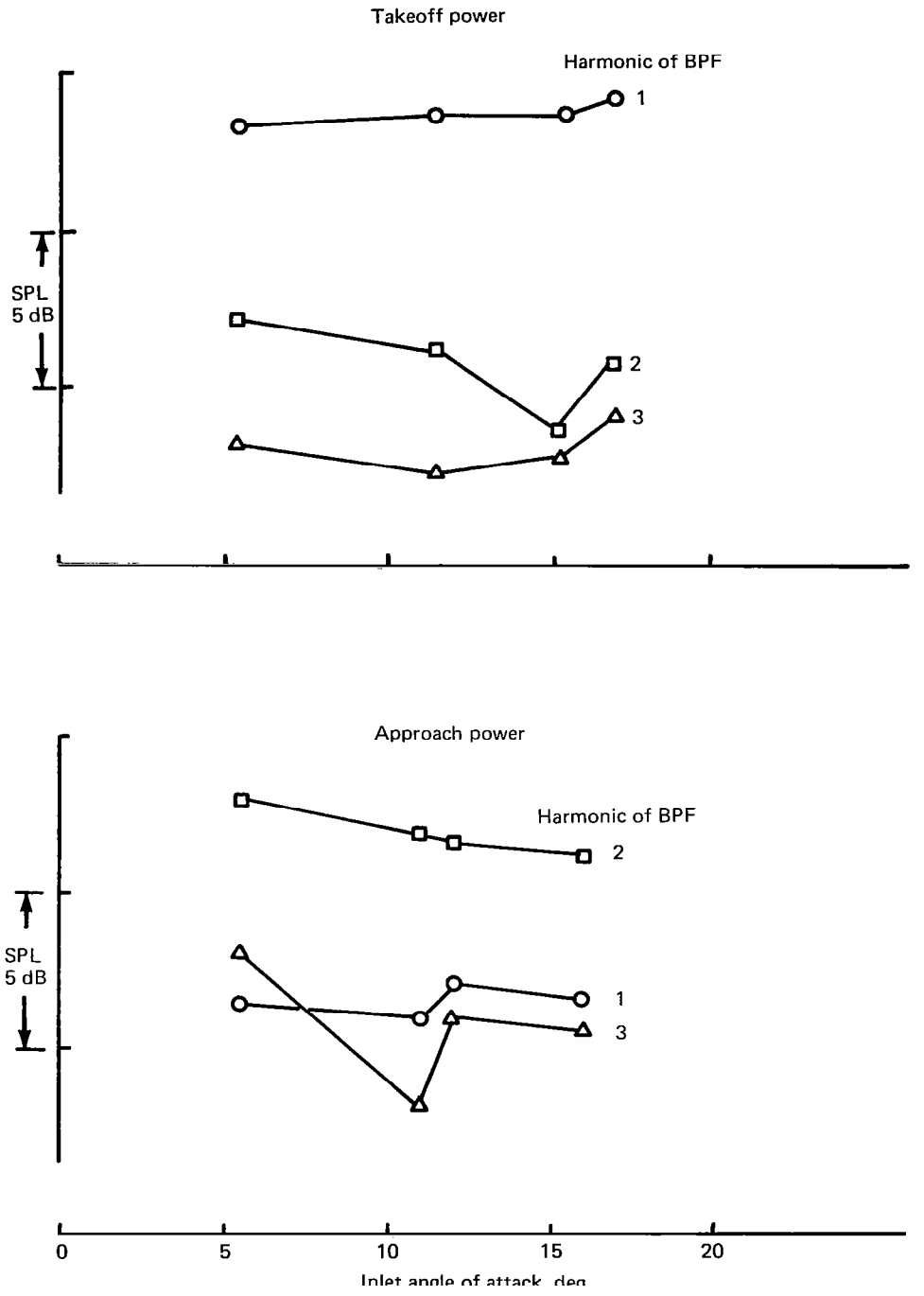
Takeoff power
Harmonic of BPF
1
SPL
5 dB
2
3
Approach power
Harmonic of BPF
2
SPL
5 dB
1
3
0
5
10
15
20
Inlet angle of attack, deg

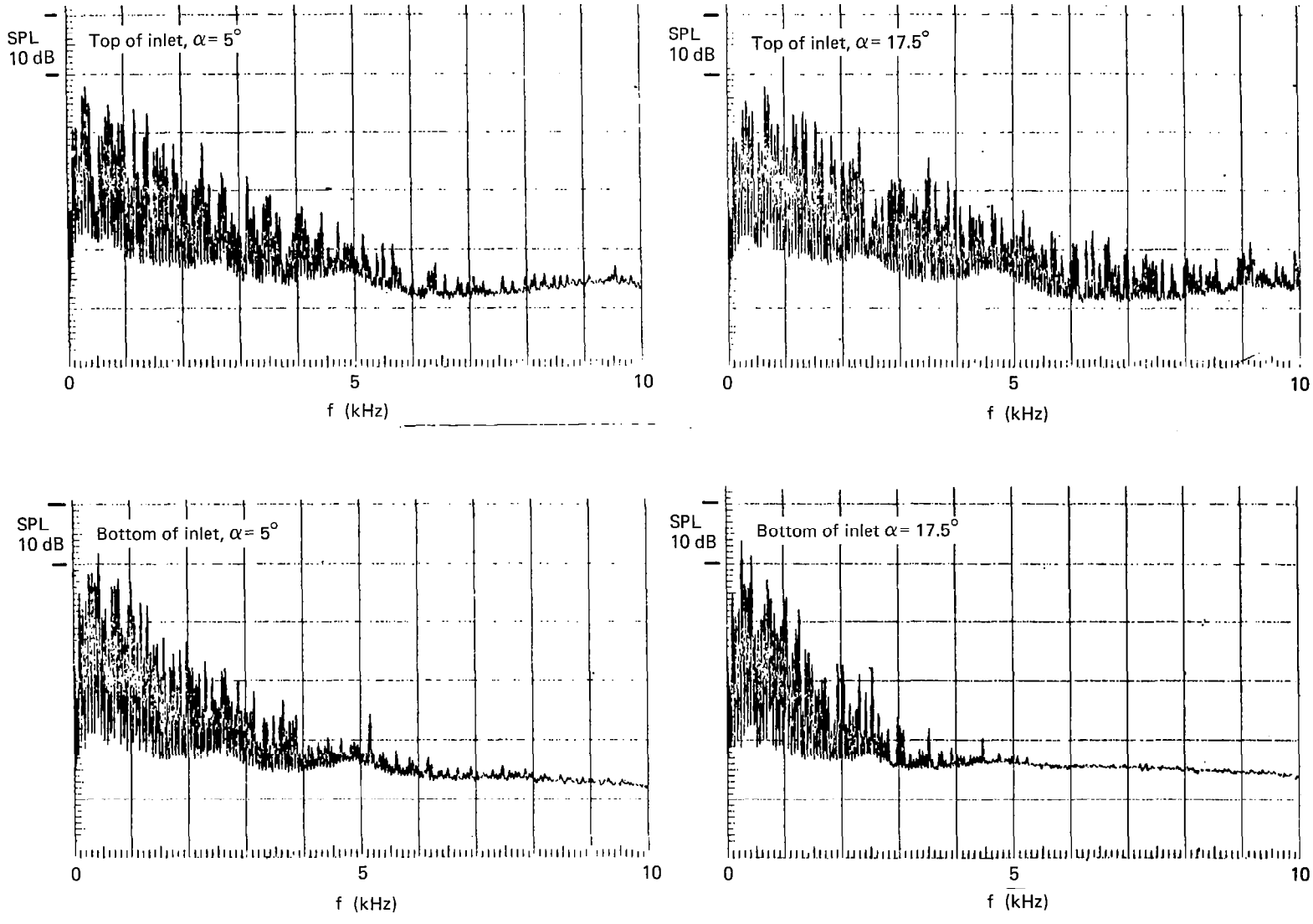

Figure 66.—Sound Pressure Spectra at Takeoff Power at Two Inlet Surface Locations for Two Inlet Angle of Attack Conditions

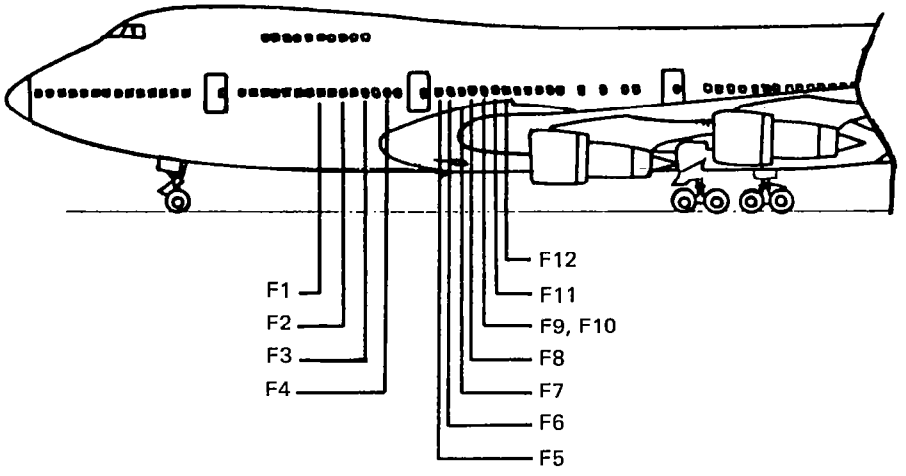

Figure 67.—Locations of Fuselage Mounted Microphones

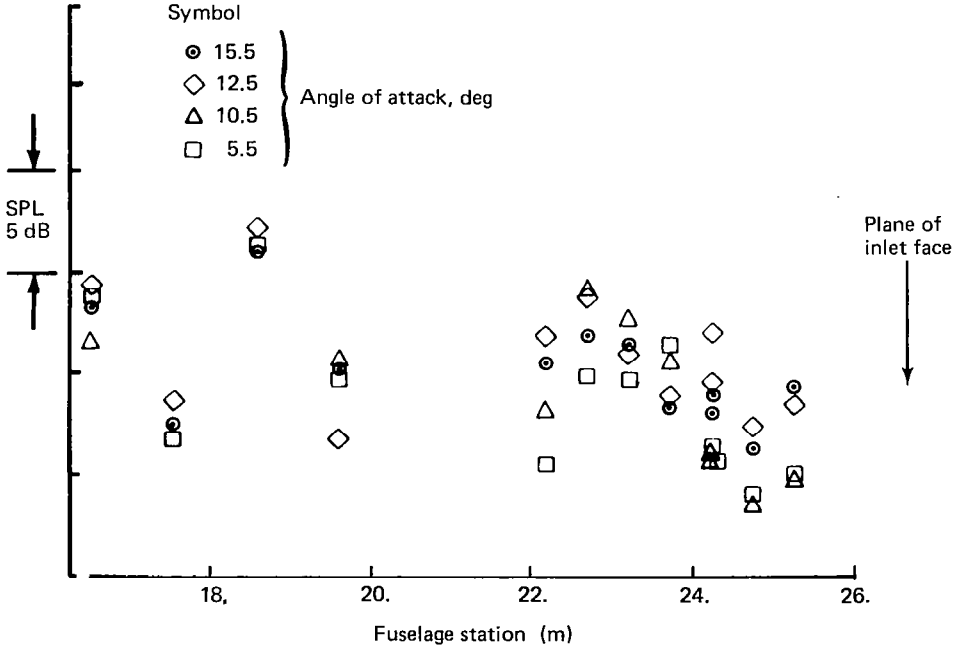

Figure 68.—Sound Pressure Level at Second Harmonic of Blade Passing Frequency at Fuselage Surface for Approach Power

7.0 CONCLUSIONS; RECOMMENDATIONS AND SUMMARY OF RESULTS

Based on a literature search, an atmospheric turbulence model has been selected that predicts turbulence intensities, integral scales and spectra as a function of the altitude above the ground, the mean wind velocity, the surface roughness and atmospheric stability. An existing flow contraction model has been extended to provide all the one-dimensional spectra of the post-contraction turbulence for simple, isotropic pre-contraction turbulence. Narrow-band fan noise resulting from ingested anisotropic but homogeneous turbulence has been studied with existing fan noise models with particular emphasis on fan noise resulting from atmospheric turbulence in static and flight conditions. Based on the material presented in this study the following conclusions have been drawn and the following recommendations are made:

Rotor Tone Noise Due to Atmospheric Turbulence

- The difference in fan tone sound power at BPF due to ingested atmospheric turbulence between typical static test conditions and typical landing approach conditions is in the order of 30 dB. Based on this difference, it is concluded that fan noise due to ingested atmospheric turbulence, is negligible in landing approach conditions for the currently-used high-bypass ratio engines.

- Fan noise due to atmospheric turbulence is expected to be below actual fan noise in flight conditions. It is therefore assumed, that it is not necessary to simulate in-flight turbulence in static tests. However, fan noise due to atmospheric turbulence in static tests should be reduced to levels below broadband fan noise in flight conditions. An effective way to achieve this is the reduction of the turbulence intensities in the static inflow field. The following guidelines are recommended for static test conditions:

    - usage of an inflow control device
    - low limits on wind velocities
    - small surface roughness scale in the test stand environment
    - large height of engine axis above ground
    - mean wind direction from the forward arc to eliminate reingestion

Proper test stand and bellmouth inlet design and possibly inlet boundary layer suction are necessary to achieve this reduction.

- Fan tone noise due to convected turbulence is dominated by the distortion elements within a small range of transverse scales. For typical turbulence energy distributions this range covers about one decade and is centered around a transverse scale in the order of 30% of the rotor blade spacing at the blade tip. For a given turbulence variance, maximum sound power levels are achieved at transverse integral scales in the order of 25% of the rotor blade spacing at the blade tip. For a JT9D fan this is about 4.1 cm and for the JT15D fan it is about 1.3 cm.

- Although fan tone noise due to convected turbulence is dominated by the distortion elements within a small range of transverse scales, it is relatively insensitive to changes in the transverse integral scale. Over a large range of transverse integral scales (5 to 200% of the fan blade spacing at the blade tip) the sound power due to convected turbulence varies only by 6 dB. This is due to the turbulent energy distribution, which is based on the von Karman spectra. For the mentioned region of transverse integral scales the range of distortion elements that dominate the fan noise generation contain always a significant fraction of the total turbulence energy.

- All correlation coefficients characterizing the inflow turbulence field have an effect on the resulting fan noise. A vortex field with its uneven radial velocity distribution function causes lower sound power levels than the corresponding Gaussian eddy field with an even radial velocity distribution function. This is due to the fact that a significant amount of the turbulent energy in the vortex field contributes to higher order radial modes which do not propagate.

- The difference in fan tone noise due to atmospheric turbulence between static and flight conditions is primarily due to the difference in the intensities of the turbulence involved in the fan tone noise generation. In static conditions the atmospheric turbulence is affected by a large inflow contraction, which results in:

  - large initial scale and therefore high initial turbulence energy level
  - large increase in the standard deviation of the transverse turbulence component
  - large streamwise integral scale at the fan face.

  In the flight conditions the turbulent energy at large wavenumbers decreases with altitude, due to the nearly constant turbulence variance and the increase of the integral scales with altitude.

- Due to the mean velocity profile in the ambient air in static conditions, the highest intensities for the transverse turbulence component are expected to occur in the bottom of the inlet, where the turbulence is exposed to the largest contraction ratios. It is recommended that special attention be given the attenuation of the turbulence entering the fan in the bottom segment of the inlet.

- For the fan geometry representative for the currently used high bypass ratio engines, the fan noise due to atmospheric turbulence is due to the streamwise turbulence component in the flight condition and due to the transverse component in static tests.

Effect of flow contraction on initially isotropic turbulence:

- According to analytical models, the transverse turbulence component increases while the streamwise component decreases in a flow contraction. For small contraction ratios the analytical model predictions agree reasonably well with the experimental data. But at large contraction ratios, typical for static tests, the analytical models overpredict the attentuation of the streamwise turbulence component.

- Most of the changes in the spectral distribution of the transverse turbulence component occur in the first segment of the contraction, at contraction ratios smaller than three. The most significant change occurs in the one-dimensional spectrum for the transverse wavenumber component normal to the turbulence velocity component. For large contraction ratios the post-contraction turbulence field is dominated by the transverse turbulence component and can be represented with a unidirectional vortex field.

Inlet angle of attack effects on fan noise:

- The effect of inlet angle of attack on fan noise has been investigated with sound pressure measurements on the inlet walls, fan duct walls and fuselage surface over the full operational range of aircraft angle of attack. The measurements indicate that there is no obvious correlation between inlet angle of attack changes and changes in broadband noise as well as narrowband noise at BPF and its second and third harmonic. A circumferential variation of the buzzsaw sound pressure field in the inlet, that increases with angle of attack has been observed. The acquired data did not allow the evaluation of inlet angle of attack effects on fan noise radiation. The feasibility to evaluate such an effect in flight tests should be investigated prior to future flight tests.

- For the particular engine used in the flight test the most significant changes in the mean flow field at the fan face, associated with changes in the inlet angle of attack, are probably due to a change in the rotor tip flow rather than changes in the inlet flow field. Most likely they result from the relative motion between the fan and the fan casing introduced by the asymmetric loads on the inlet nacelle.

- The remaining fan tone noise at BPF in flight conditions is neither due to atmospheric turbulence nor due to inlet angle of attack related distortions.

APPENDIX
ONE DIMENSIONAL POST-CONTRACTION SPECTRA

Ribner and Tucker (Ref. 17) derived the three-dimensional post-contraction spectra for an axisymmetric contraction and initially isotropic turbulence

$$\Gamma_{11}{}^{B}(\mathcal{H}) = \frac{\ell_2{}^2}{\ell_1}\, G(k)\, \frac{\left(k^2 - k_1{}^2\right) k^4}{\left(\epsilon\, k_1{}^2 + k_2{}^2 + k_3{}^2\right)^2} \tag{A.1}$$

$$\Gamma_{22}{}^{B}(\mathcal{H}) = \ell_1\, G(k) \left[k^2 - k_2{}^2 - \frac{2k_1{}^2\, k_2{}^2\, (1-\epsilon)}{\epsilon k_1{}^2 + k_2{}^2 + k_3{}^2} + \frac{k_1{}^2\, k_2{}^2 \left(k^2 - k_1{}^2\right)\, (1-\epsilon)}{\left(\epsilon k_1{}^2 + k_2{}^2 + k_3{}^2\right)^2} \right]^2 \tag{A.2}$$

with G(k) = spectrum function of isotropic turbulence.

Based on these equations and a given spectrum function, the one-dimensional spectra at the post-contraction location can be determined by integration over two of the wavenumber components. This integration is only possible, however, for simple spectrum functions. One of the simplest functions used to represent turbulence at large Reynolds numbers is

$$G(k) = \frac{N}{\left(k^2 + \gamma^2\right)^3} \tag{A.3}$$

For isotropic conditions it forms the basis for the Dryden spectra

$$F_1{}^{A}(k_1) = \frac{\pi N}{k_1{}^2 + \gamma^2} \tag{A.4}$$

$$F_2{}^{A}(k_1) = F_3{}^{A}(k_1) = \frac{\pi N \left(3k_1{}^2 + \gamma^2\right)}{2\left(k_1{}^2 + \gamma^2\right)^2} \tag{A.5}$$

with

$$\gamma = \frac{1}{L} \qquad N = \frac{2\sigma^2}{\pi^2 L}$$

σ^2 = variance
L = integral length scale

Based on this spectrum function Ribner and Tucker derived the longitudinal one-dimensional spectra at the post-contraction location

$$F_1^B(k_1) \qquad F_2^B(k_1) = F_3^B(k_1)$$

In the course of the present investigation three additional spectra have been derived to complete the matrix of one-dimensional post-contraction spectra

$$F_1^B(k_2) = F_1^B(k_3)$$

$$F_2^B(k_2) = F_3^B(k_3)$$

$$F_2^B(k_3) = F_3^B(k_2)$$

Explicit equations have been derived for these spectra

$$F_1^B(\mathcal{K}_2) = 2 \iint_{-\infty}^{\infty} \Gamma_{11}^B(\mathcal{K})\, d\mathcal{K}_1 \; d\mathcal{K}_3 = \ell_2 F_1^B(k_2) \tag{A.6}$$

Since the three-dimensional spectra have been formulated as a function of k rather than $\mathcal{K}$, the integration will be executed in the k coordinate system

$$(\mathcal{K}_1, \mathcal{K}_2, \mathcal{K}_3) = \left(\frac{k_1}{\ell_1}, \frac{k_2}{\ell_2}, \frac{k_3}{\ell_3}\right)$$

$$F_1^B(k_2) = \frac{2N}{\ell_1^2} \iint_{-\infty}^{\infty} \frac{(k_2^2 + k_3^2)\,(k_1^2 + k_2^2 + k_3^2)}{(k_1^2 + k_2^2 + k_3^2 + \gamma^2)^3\,(\epsilon k_1^2 + k_2^2 + k_3^2)^2}\, dk_1 \; dk_3 \tag{A.7}$$

The integration is performed in polar coordinates

$$k_1 = r \cos\theta \qquad k_3 = r \sin\theta$$

$$F_1{}^B(k_2) = \frac{2N}{\ell_1{}^2} \int_0^{\infty} \int_0^{2\pi} \frac{\left(k_2{}^2 + r^2 - r^2 \cos^2\theta\right)\left(k_2{}^2 + r^2\right)^2}{\left(k_2{}^2 + \gamma^2 + r^2\right)^3 \left(k_2{}^2 + r^2 + r^2(\epsilon - 1)\cos^2\theta\right)^2} \, r\,dr\,d\theta \quad \text{(A.8)}$$

The integrations provide the following result

$$F_1{}^B\left(k_2\right) = \frac{\pi N}{\ell_1{}^2 \gamma^2}\left(D_1 + D_2 - D_3 - D_4\right) \quad \text{with} \quad \text{(A.9)}$$

$$D_1 = \frac{p+q}{2q^2}\left[\frac{3}{2}\left(\frac{\epsilon}{q} - 1\right)\left(\frac{p}{S} - \sqrt{\epsilon}\right) - \frac{p}{S^2} - \left(\frac{3(q-\epsilon)^2}{4q} + \epsilon\right)\frac{\Delta}{q}\right] \quad \text{(A.10)}$$

$$D_2 = \left[\frac{p}{q^2}\left(\frac{\epsilon}{q} + 2\right) + \frac{2}{q}\right]\left[\frac{(q-\epsilon)}{2\sqrt{q}}\Delta - \sqrt{\epsilon} + \frac{p}{S}\right] \quad \text{(A.11)}$$

$$D_3 = \frac{\Delta}{\sqrt{q}}\left[1 + (1-\epsilon)^2\left(\frac{p}{q}\right)^3\right] \quad \text{(A.12)}$$

$$D_4 = \frac{2\sqrt{\epsilon}}{1+\sqrt{\epsilon}}\,\frac{(q+\epsilon)^2}{q^3} \quad \text{(A.13)}$$

$$p = \frac{k_2{}^2}{\gamma^2} \quad \text{(A.14)}$$

$$S = p + 1 \tag{A.15}$$

$$q = p\,(1 - \epsilon) - \epsilon \tag{A.16}$$

$$\Delta = \arcsin\left(\frac{q - 1}{s\,(1 - \epsilon)}\right) - \arcsin\left(\frac{q - \epsilon}{p\,(1 - \epsilon)}\right) \tag{A.17}$$

$$\epsilon = \frac{\ell_2^{\,2}}{\ell_1^{\,2}} \tag{A.18}$$

This solution is restricted by the following condition

$$k_1^{\,2} > \frac{\epsilon}{1 - \epsilon}\ \gamma^2$$

The one-dimensional spectra for the transverse turbulence component are based on the three-dimensional spectrum of equation (A.2) and are obtained by integration over k_1, and either k_2 or k_3. Integration over k_1 and k_3 gives

$$F_2^{\,B}\,(k_2) = \frac{\pi N p}{\ell_2^{\,2}\,\gamma^2\,S^2}\ \left(G_1 + G_2 + G_3\right) \tag{A.19}$$

with

$$G_1 = 1 + \frac{S}{p} \tag{A.20}$$

$$G_2 = \left[\frac{\epsilon - 3}{2} - \frac{\epsilon - 1}{2}\left(\frac{p}{q}\right)\right]\frac{S^2}{q}\left[\frac{p}{S}\left(\frac{1}{S} - \frac{1}{2} - \frac{3\epsilon}{2q}\right) + \sqrt{\epsilon}\left(\frac{1}{2} + \frac{3\epsilon}{2q}\right) + \left(\frac{3\epsilon^2 + 2\epsilon q - q^2}{4q}\right)\frac{\Delta}{q}\right] \tag{A.21}$$

$$G_3 = \frac{\epsilon - 1}{2}\left(\frac{p\,S^2}{q^3}\right)\left[2\epsilon\left(\frac{p}{S} - \sqrt{\epsilon}\right) + 4\epsilon\,\left(\epsilon - \sqrt{\epsilon}\right) - \epsilon\,(q + 3\epsilon)\frac{\Delta}{\sqrt{q}}\right] \tag{A.22}$$

$$P = \frac{k_2^{\,2}}{\gamma^2} \tag{A.23}$$

s, q, Δ and ϵ are defined by equation (A.15) through (A.18). The validity of the solution is again limited to

$$k_2^2 > \frac{\epsilon}{1-\epsilon}\gamma^2$$

For large contraction ratios ($\epsilon \ll 1.$) the spectrum can be approximated by

$$F_2^B(k_2) = \frac{\pi N}{\ell_2^2 \gamma^2 S}\left\{1 + \frac{p}{2} + \frac{S\sqrt{p}}{4}\left[\arcsin\left(1 - \frac{2}{S}\right) - \frac{\pi}{2}\right]\right\} \tag{A.24}$$

Integration of the three-dimensional spectrum defined in Equation (A.2) over k_1 and k_2 provides the second one-dimensional spectrum for the transverse component

$$F_2^B(k_3) = \frac{\pi N}{\ell_2^2 \gamma^2}\left(H_1 + H_2 + H_3 + H_4 + H_5\right) \tag{A.25}$$

with

$$H_1 = \frac{p}{S^2}\,\frac{2}{1-\epsilon} \tag{A.26}$$

$$H_2 = \frac{1}{1-\epsilon}\,\frac{\epsilon - q}{q}\left(\frac{p}{S} - \sqrt{\epsilon}\right) \tag{A.27}$$

$$H_3 = \frac{\Delta}{\sqrt{q}}\left[\epsilon\left(\frac{3+\epsilon}{1-\epsilon}\right) - \frac{p^2}{2q}(1-\epsilon)\right] \tag{A.28}$$

$$H_4 = \frac{1}{q(1-\epsilon)}\left[p\left(2 - \epsilon - \epsilon^2\right) - \left(6\epsilon + 2\epsilon^2\right)\right]\left[\frac{p}{S} - \sqrt{\epsilon} + \frac{q-\epsilon}{2\sqrt{q}}\Delta\right] \tag{A.29}$$

$$H_5 = \frac{p\left(2 - \epsilon - \epsilon^2\right) - \epsilon(3+\epsilon)}{(1-\epsilon)\,q^2}\left[\left(-\frac{q}{2S} - \frac{3(q-\epsilon)}{4}\right)\frac{p}{S} + \frac{3}{4}(q-\epsilon)\sqrt{\epsilon}\right.$$

$$\left. - \frac{\Delta}{\sqrt{q}}\left(\frac{3(q-\epsilon)^2 + 4q\epsilon}{8}\right)\right] \tag{A.30}$$

$$p = \frac{k_3^2}{\gamma^2} \tag{A.31}$$

s, q, Δ and ϵ are again defined by equations (A.15) through (A.18) and the validity of the solution is again limited to

$$k_3^2 > \frac{\epsilon}{1-\epsilon}\ \gamma^2$$

The approximate solution for large contraction ratios ($\epsilon << 1$) is

$$F_2^B\left(k_3\right) = \frac{\pi N}{\ell_2^2\,\gamma^2}\left\{\left(\frac{1}{S}-\frac{1}{2}\right)\frac{p}{S}-\frac{\sqrt{p}}{4}\left[\arcsin\left(1-\frac{2}{S}\right)-\frac{\pi}{2}\right]\right\} \tag{A.32}$$

The integral scales are determined based on the following relationship.

$$L_{ij} = \pi\left[\frac{1}{2\pi}\int_{-\infty}^{\infty} C_i\left(x_j\right) e^{-i\,\mathcal{H}_j\,x_j}\,dx_j\right]_{\mathcal{H}_j = .0}$$

$$= \frac{\pi}{2\,\sigma_i^2}\ F_i^B\left(\mathcal{H}_j = .0\right) = \frac{\pi\,\ell_j}{2\,\sigma_i^2}\ F_i^B\left(k_j = .0\right)$$

The post-contraction integral length scales have been determined based on this equation.

$$F_1^B\left(k_1 = .0\right) = \frac{2\,\sigma_A^2\,L_A}{\pi\,\ell_1^2} \qquad L_{11}^B = \frac{L_A\,\sigma_A^2}{\ell_1\,\sigma_{1B}^2}$$

$$F_1^B\left(k_2 = .0\right) = \frac{\sigma_A^2\,L_A}{\ell_1\,\ell_2\,\pi} \qquad L_{12}^B = \frac{L_A\,\sigma_A^2}{2\ell_1\,\sigma_{1B}^2} = \frac{L_{11}}{2}$$

$$F_2^B\left(k_1 = .0\right) = \frac{\sigma_A^2\,L_A}{\pi\,\ell_2^2} \qquad L_{21}^B = \frac{L_A\,\ell_1\,\sigma_A^2}{2\,\ell_2^2\,\sigma_{2B}^2}$$

$$F_2^B\left(k_2 = .0\right) = \frac{2\,\sigma_A^2\,L_A}{\pi\,\ell_2^2} \qquad L_{22}^B = \frac{L_A\,\sigma_A^2}{\ell_2\,\sigma_{2B}^2}$$

$$F_2^B\left(k_3 = .0\right) = \frac{\sigma_A^2\,L_A}{\pi\,\ell_1\,\ell_2} \qquad L_{23}^B = \frac{L_A\,\sigma_A^2}{2\,\ell_1\,\sigma_{2B}^2}$$

with

σ_A^2 = variance of precontraction turbulence

L_A = integral scale parallel to turbulence component in precontraction turbulence

The ratios $\left(\sigma_A^2/\sigma_{1B}^2\right)$ and $\left(\sigma_A^2/\sigma_{2B}^2\right)$ are defined by equation (4.2.20) and (4.2.21).

REFERENCES

1. Plucinsky, J. C.: *"Quiet Aspects of the P&WA JT15D Turbofan"*, Paper 730289, SAE Business Aircraft Meeting, April, 1973.

2. Feiler, C. E., Merriman, J. E.: *"Effects of Forward Velocity and Acoustic Treatment on Inlet Fan Noise"*, AIAA Paper 74-946, August, 1974.

3. Merriman, J. E., Good, R. C.: *"Effect of Forward Motion on Fan Noise"*, AIAA Paper 75-464, March, 1975.

4. Roundhill, J. P., Schaut, L. A.: *"Model and Full Scale Test Results Relating to Fan Noise Flight Effects"*, AIAA Paper 75-465, March, 1975.

5. Cumpsty, N. A., Lowrie, B. W.: *"The Cause of Tone Generation by Aero-Engine Fans at High Subsonic Tip Speeds and the Effect of Forward Speed"*. ASME Paper 73-WA/GT-4, November, 1973.

6. Lowrie, B. W.: *"Simulation of Flight Effects on Aero-Engine Fan Noise"*, AIAA Paper 75-463, March 1975.

7. Hodder, B. K.: *"An Investigation of Possible Causes for the Reduction of Fan Noise in Flight"*, AIAA Paper 76-585, 1976.

8. Bekofske, K. L., Sheer, R. E., Wang, J. C.: *"Fan Inlet Disturbances and Their Effect on Static Acoustic Data"*, ASME Paper 77-GT-63, March, 1977.

9. Cocking, B. J., Ginder, R. B.: *"The Effect of an Inlet Flow Conditioner on Fan Distortion Tones"*, AIAA Paper 77-1324, October, 1977.

10. Shaw, L. M., et al: *"Inlet Turbulence and Fan Noise Measured in an Anechoic Wind Tunnel and Statically With an Inlet Flow Control Device"*, AIAA Paper 77-1345, October, 1977.

11. Kantola, R. A., Warren, R. E.: *"Reduction of Rotor-Turbulence Interaction Noise in Static Fan Noise Testing"*. AIAA Paper 79-0656, March, 1979.

12. Dietrich, D. A., Heidmann, M. F., Abbott, J. M.: *"Acoustic Signatures of a Model Fan in the NASA-Lewis Anechoic Wind Tunnel"*, NASA TMX-73560, 1976.

13. Wesoky, L. H., Dietrich, D. A., Abbott, J. M.: *"Simulated Flight Effects on Noise Characteristics of a Fan Inlet With High Throat Mach Number"*, NASA Technical Paper 1199, April, 1978.

14. Stakolich, E. G.: *"Effect of Flight Loads on Turbofan Engine Performance"*, NASA TM 79041, March, 1979.

15. Pegg, R. J., Magliozzo. B., Farassat, F.: *"Some Measured and Calculated Effects of Forward Velocity on Propeller Noise"*, ASME Paper 77-GT-70, March, 1977.

16. Barr, N. M., Gangaas, D., Schaeffer, D. R.: *Wind Models for Flight Simulator Certification of Landing and Approach Guidance and Control Systems"*, U. S., D.O.T., FAA Report No. FAA-RD-74-206, December, 1974.

17. Ribner, H. S., Tucker, M.: *"Spectrum of Turbulence in a Contracting Stream"*, NACA Report 1113, 1953.

18. Van der Hoven, I.: *"Power Spectrum of Horizontal Wind Speed in the Frequency Range from .0007 to 900 Cycles Per Hour"*, J. Meteorol., Vol. 14, pg. 160, 1957.

19. Hanson, D. B.: *"Measurements of Static Inlet Turbulence"*, AIAA Paper 75-467, March, 1975.

20. Hanson, D. B.: *"Study of Noise Sources in a Subsonic Fan Using Measured Blade Pressures and Acoustic Theory"*, NASA CR-2574, August, 1975.

21. Teuniessen, H. W.: *"Characteristics of the Mean Wind and Turbulence in the Planetary Boundary Layer"*, UTIAS Review No. 32, October, 1970.

22. Engineering Sciences Data Unit, *"Characteristics of Atmospheric Turbulence Near the Ground (Part III)"*, ESDU Item, Number 75001, July, 1975.

23. Counihan, J.: *"Adiabatic Atmospheric Boundary Layers, A Review and Analysis of Data from the Period 1880 – 1972"*, Atmospheric Environment, Vol. 9, pgs. 871-905. February, 1975.

24. A DDC Bibliography on Atmospheric Turbulence, Vol. I, DDC-TAS-68-40, Defense Documentation Center, Alexandria, Virginia, September, 1968.

25. Lumley, J. L., Panofsky, H. A.: *"The Structure of Atmospheric Turbulence"*, John Wiley & Sons, Inc., 1964.

26. Gunter, D. E., Jones, G. W., Jones, J. W., Monson, K. R.: *"Low Altitude Atmospheric Turbulence, LO-LOCAT Phases I & II"*. ASD-TR-69-12, Wright Patterson Air Force Base, February, 1969.

27. Elderkin C. E.: *"Experimental Investigation of the Turbulence Structure in the Lower Atmosphere"*, Batelle Northwest Report, BNWL-329, December, 1966.

28. Prandtl, L.: *"Attaining a Steady Air Stream in Wind Tunnels"*, NACA TM 726, 1933.

29. Taylor, G. I.: *"Turbulence in a Contracting Stream"*, Z.A.M.M., Vol. 15, 1935.

30. Batchelor, G. K., Proudman, I.: *"The Effect of Rapid Distortion of a Fluid in Turbulent Motion"*, Quarterly Journal of Applied Mathematics, Vol. 7, Pt. 1, 1954.

31. Uberoi, M. S.: *"Effect of Wind Tunnel Contraction on Freestream Turbulence"*, Journal of Aeronautical Sciences, August, 1956.

32. Ganz, U. W.: *"Measurement of Atmospheric Turbulence in the Inflow Field of a Stationary Engine"*, Boeing Document D6-42740, May, 1980.

33. Clark, T. L., Ganz, U. W., Graf, G. A., Westall, J. S.: *"Analytic Models of Ducted Turbomachinery Tone Noise Sources"*, Vol. I, NASA-CR-132443, May, 1974.

34. Clark, T. L.: *"Analytical Model for Fan Tone Noise Due to Convected Turbulence"*, Boeing Document D6-47048, May, 1980.

35. Melick, H. C.: *"Analysis of Inlet Flow Distortion and Turbulence Effects on Compression Stability"*, NASA CR 114577, March, 1973.

36. Lee, Y. W.: *"Statistical Theory of Communication"*, John Wiley & Sons, Inc., 1960.

37. Naumann, H., Yeh, H.: *"Lift and Pressure Fluctuations of a Cambered Airfoil Under Periodic Gusts and Applications in Turbomachinery"*, Journal of Engineering for Power, January, 1973.

38. Pickett, G. F.: *"Effects of Non-Uniform Inflow on Fan Noise"*, ASA Paper, April, 1974.

39. Hanson, D. B.: *"Study of Noise and Inflow Distortion Sources in the NASA QF-1B Fan Using Measured Blade and Vane Pressures"*, NASA-CR-2899, September, 1977.

1 Report No	2 Government Accession No	3 Recipient's Catalog No
NASA CR-3302		

4 Title and Subtitle	5 Report Date
ANALYTICAL INVESTIGATION OF FAN TONE NOISE DUE TO INGESTED ATMOSPHERIC TURBULENCE	August 1980
	6 Performing Organization Code
7 Author(s)	8 Performing Organization Report No
Ulrich W. Ganz	
	10 Work Unit No
9 Performing Organization Name and Address	
Boeing Commercial Airplane Company P.O. Box 3707 Seattle, WA 98124	11 Contract or Grant No NAS1-15085
	13 Type of Report and Period Covered
12 Sponsoring Agency Name and Address	Contractor Report
National Aeronautics and Space Administration Washington, DC 20546	14 Sponsoring Agency Code

15 Supplementary Notes Prepared under Contract NAS1-15085 with United Technologies; Boeing Commercial Airplane Company, subcontractor.

Langley Technical Monitor: David Chestnutt Topical Report

16 Abstract

An analytical study of fan narrowband noise due to atmospheric Turbulence has been conducted. The atmospheric turbulence involved in the fan noise generation is evaluated with an existing model for the atmospheric turbulence and an extended version of an existing model concerned with the effects of a flow contraction on convected turbulence. Fan tone noise due to ingested atmospheric turbulence is evaluated with existing fan noise models. The results indicate that the difference in fan narrowband noise due to atmospheric turbulence between static and flight landing approach conditions is in the order of 30 dB. It is concluded that fan noise due to atmospheric turbulence is insignificant in flight conditions for the fans used in the current high bypass ratio engines. The difference in fan narrowband noise between the two conditions is primarily due to the low intensity of the turbulence involved in fan noise generation in flight conditions. Fan noise due to atmospheric turbulence in static conditions should be reduced below the flight fan broadband noise levels which is best achieved with a reduction in the intensity of the fan inflow turbulence. Such a reduction can be obtained with the use of an inflow control device, low wind velocities, small surface roughness in the test stand environment and large engine axis height above the ground. Peak sound power levels for fan tone noise due to ingested turbulence occur for transverse integral scales in the order of 25% of the rotor blade spacing in the fan tip region.

17 Key Words (Suggested by Author(s))	18 Distribution Statement
Fan Noise Inlet Noise Inlet Distortion Inlet Turbulence Atmospheric Turbulence	Unclassified - Unlimited Subject Category 71

19 Security Classif (of this report)	20 Security Classif (of this page)	21 No of Pages	22 Price*
Unclassified	Unclassified	148	A07

*For sale by the National Technical Information Service, Springfield, Virginia 22161

NASA-Langley, 1980